Graphene-based chemiresistive nanosensor: from gas detection to electronic olfaction

DISSERTATION

zur Erlangung des akademischen Grades

Doktoringenieur (Dr.-Ing.)

vorgelegt

der Fakultät Maschinenwesen
der Technischen Universität Dresden

von

M. Sc. Shirong Huang

geboren am 6. Februar 1988 in Fuzhou, China

Tag der Einreichung: 2. Dezember 2021

Tag der Verteidigung: 5. April 2022

Vorsitzender: Prof. Dr. Markus Kästner

Gutachter: Prof. Dr. Gianaurelio Cuniberti

                     Prof. Dr. Michael Schmuker

Mitglied: Prof. Dr. Andreas Richter

                     Prof. Dr. Kerstin Eckert

DECLARATION

I hereby declare that the thesis entitled "Graphene-based chemiresistive nanosensor: from gas detection to electronic olfaction" submitted by me, for the award of the degree of *Doktoringenieur* to Technische Universität Dresden is a record of bonafide work carried out by me under the supervision of Prof. Dr. Gianaurelio Cuniberti, in the Chair of Materials Science and Nanotechnology at TU Dresden.

I further declare that the work reported in this thesis has not been submitted and will not be submitted, either in part or in full, for the award of any other degree or diploma in this institute or any other institute or university.

Place: Dresden

Date: 10. April 2022 **Signature of the Candidate**

Abstract

Gas sensors are extensively utilized in monitoring air quality, ensuring public safety, and detecting released trace gases in countless industrial fields. Accordingly, the development of highly efficient, sensitive, selective, reliable, low power consumption and low-cost gas sensors is in considerable demand. A myriad of gas sensors using traditional metal oxide semiconductor materials have been developed, nevertheless, the selectivity and power-consumption of these sensors are still far from satisfactory. Inspired by human olfaction, advanced nanomaterials as well as artificial intelligence technology may provide the solution to these issues. In this work, the pristine graphene-based highly sensitive gas sensors working at room temperature for NH_3 detection were developed. In combination with machine learning techniques, the selectivity of pristine graphene-based gas sensors is significantly enhanced, which present excellent performance towards odor discrimination.

As a first step, the stabilization mechanism of functionalized graphene in an aqueous dispersion of surfactant is elucidated *via* all-atom molecular dynamic simulations. The stabilizing role of flavin mononucleotide sodium salt (FMNS) is demonstrated by the potential of mean force calculations for pairs of graphene flakes covered by FMNS molecules. At a high surface coverage, graphene flakes repel each other which leads to the stabilization of graphene dispersions. To achieve approximately the same potential of mean force (PMF) energy barrier of 10 $kJ/(mol \cdot nm^2)$, the surface coverage of graphene flakes by FMNS molecules is 44% lower than by sodium cholate (SC) molecules, and 71% lower than by sodium dodecylbenzene-sulfonate (SDBS) molecules, respectively. With this in mind, FMNS functionalized graphene-based gas sensors are then developed, demonstrating excellent sensing performance to NH_3 gas. The optimized NH_3 sensors demonstrate outstanding performance: ultralow limit-of-detection (1.6 ppm), excellent sensitivity (2.8%, 10 ppm; 18.5%, 1000 ppm), reproducibility, reversibility, low power consumption, room temperature function, as well as low cost. The roles of FMNS from graphene preparation to NH_3 sensing are elucidated *via* all-atom molecular dynamics simulations

(MDS): (1) stabilizer for the graphene dispersion, (2) p-type dopant for graphene-based sensing element, and (3) active adsorption sites for NH_3 gas sensing.

Moreover, in combination with machine learning techniques, biomimetic electronic olfaction based on graphene single channel nanosensors is proposed. The developed prototype exhibits excellent odors (Eucalyptol – Euca, 2-nonanone – 2Nona, Eugenol – Euge, 2-phenylethanol – 2Phe, N_2) discrimination and identification performance at room temperature, maximizing the obtained results from a single nanosensor. Upon exposure to binary odor mixture, the response features behave similarly to existing individual odor component, mimicking the overshadowing effect in human olfactory perception. Computational simulations support the experimental results and reveal competing adsorption of odor molecules occur. With this approach, the industrial pollutants (NH_3, PH_3) were succefully identified at ultra-low concentration (100 ppb – 1000 ppb) with satisfying performance.

The present work represents a novel and reliable strategy to develop highly sensitivity, highly selective, and low-cost graphene-based gas sensors towards inorganic gases detection (NH_3, PH_3) and volatile organic compounds (VOCs) sensing at room temperature. The developed strategy may allow for gas detection, odor recognition of a wide spectrum of odor molecules, as well as detection of volatile organic compounds (VOC) in an extensive variety of domains, e.g., environmental monitoring, public security, smart farming, or disease diagnosis (e.g., lung cancer, COVID-19).

Keywords: graphene, liquid phase exfoliation, gas sensor, electronic nose, sensitivity, selectivity, machine learning, molecular dynamic simulation, NH_3/PH_3, volatile organic compounds

Kurzfassung

Gassensoren werden in großem Umfang zur Überwachung der Luftqualität, zur Gewährleistung der öffentlichen Sicherheit und zum Nachweis freigesetzter Spurengase in zahlreichen Industriebereichen eingesetzt. Dementsprechend groß ist der Bedarf an der Entwicklung hocheffizienter, empfindlicher, selektiver, zuverlässiger, stromsparender und kostengünstiger Gassensoren. Eine Vielzahl von Gassensoren, die herkömmliche Metalloxid-Halbleitermaterialien verwenden, wurden bereits entwickelt, doch die Selektivität und der Stromverbrauch dieser Sensoren sind noch lange nicht zufriedenstellend. In Anlehnung an den menschlichen Geruchssinn könnten fortschrittliche Nanomaterialien und Technologien der künstlichen Intelligenz eine Lösung für diese Probleme bieten. In dieser Arbeit entwickeln wir hochempfindliche Gassensoren auf Graphenbasis, die bei Raumtemperatur arbeiten und u.a. NH_3 nachweisen. In Kombination mit Techniken des maschinellen Lernens wird die Selektivität von Gassensoren auf Basis von reinem Graphen deutlich verbessert, so dass sie eine hervorragende Leistung bei der Geruchsunterscheidung aufweisen.

In einem ersten Schritt wird der Stabilisierungsmechanismus von funktionalisiertem Graphen in einer wässrigen Dispersion eines Tensids mittels molekulardynamischer All-Atom-Simulationen aufgeklärt. Die stabilisierende Rolle des Flavinmononukleotid-Natriumsalzes (FMNS) wird durch das Potenzial von mittleren Kraftberechnungen für Paare von Graphenflocken, die von FMNS-Molekülen bedeckt sind, nachgewiesen. Bei einer hohen Oberflächenbedeckung stoßen sich die Graphenflocken gegenseitig ab, was zu einer Stabilisierung der Graphen-Dispersionen führt. Um annähernd die gleiche Energiebarriere von 10 $kJ/(mol \cdot nm^2)$ zu erreichen, ist die Oberflächenbedeckung der Graphenflocken durch FMNS-Moleküle um 44% niedriger als durch Natriumcholat (SC)-Moleküle bzw. um 71 % niedriger als durch Natriumdodecylbenzolsulfonat (SDBS)-Moleküle. Vor diesem Hintergrund wurden FMNS-funktionalisierte Gassensoren auf Graphenbasis entwickelt, die eine hervorragende Sensorfunktion für NH_3-Gas: ultraniedrige Nachweisgrenze (1,6 ppm), ausgezeichnete Empfindlichkeit (2,8%, 10 ppm; 18,5%, 1000 ppm), Reproduzierbarkeit, Reversibilität, geringer Stromverbrauch, Funktion bei Raumtemperatur sowie geringe Kos-

ten. Die Rolle von FMNS von der Graphenherstellung bis zum NH_3-Sensor wird durch Molekulardynamiksimulationen aufgeklärt: (1) Stabilisator für die Graphen Dispersion, (2) p-Typ-Dotierstoff für die Graphen-basierte Sensorik und (3) aktive Adsorptionsstellen für die NH_3-Gassensorik.

Darüber hinaus wird in Kombination mit Techniken des maschinellen Lernens ein biomimetischer elektronischer Geruchssensor auf der Grundlage von Einkanal-Nanosensoren aus Graphen vorgeschlagen. Der entwickelte Prototyp zeigt eine hervorragende Unterscheidungs- und Identifizierungsleistung von Gerüchen (Eucalyptol - Euca, 2-Nonanon - 2Nona, Eugenol - Euge, 2-Phenylethanol - 2Phe, N_2) bei Raumtemperatur und maximiert die mit einem einzigen Nanosensor erzielten Ergebnisse. Bei der Exposition gegenüber einem binären Geruchsgemisch verhalten sich die Reaktionsmerkmale ähnlich wie die einzelnen Geruchskomponenten und ahmen den Überschattungseffekt in der menschlichen Geruchswahrnehmung nach. Computersimulationen unterstützen die experimentellen Ergebnisse und zeigen, dass es zu einer konkurrierenden Adsorption von Geruchsmolekülen kommt. Mit diesem Ansatz ist es uns gelungen, die industriellen Schadstoffe (NH_3, PH_3) bei extrem niedrigen Konzentrationen (100 ppb - 1000 ppb) mit zufriedenstellender Leistung zu identifizieren.

Die vorliegende Arbeit stellt eine neuartige und zuverlässige Strategie zur Entwicklung hochempfindlicher, hochselektiver und kostengünstiger Gassensoren auf Graphenbasis dar, mit denen anorganische Gase (NH_3, PH_3) und flüchtige organische Verbindungen (VOCs) bei Raumtemperatur nachgewiesen werden können. Die entwickelte Strategie kann die Gasdetektion, die Geruchserkennung eines breiten Spektrums von Geruchsmolekülen sowie die Detektion flüchtiger organischer Verbindungen (VOC) in einer Vielzahl von Bereichen ermöglichen, z. B. Umweltüberwachung, öffentliche Sicherheit, intelligente Landwirtschaft oder Krankheitsdiagnose (z. B. Lungenkrebs, COVID-19).

Schlüsselwörter: Graphen, Flüssigphasen-Exfoliation, Gassensor, elektronische Nase, Empfindlichkeit, Selektivität, maschinelles Lernen, molekulardynamische Simulation, NH_3/PH_3, flüchtige organische Verbindungen.

Contents

Acronyms

2Nona	2-nonanone
2Phe	2-phenylethanol
2D	Two-dimensional
APTS	8-Aminopyrene-1,3,6-trisulphonic acid trisodium salt
AC	Alternating current
AFM	Atomic force microscopy
ATR-FTIR	Attenuated total reflectance-Fourier transform infrared
BTEX	Benzene, toluene, ethylbenzene, xylene
CDC	Centroid distance component
CNT	Carbon nanotube
CuPc	Copper phthalocyanine-3,4 ', 4", 4''' - tetrasulfonic acid tetrasodium salt
CVD	Chemical vapor deposition
COM	Centers of mass
DI	Deionized
DFTB	Density-Functional based Tight-Binding
Euca	Eucalyptol
Euge	Eugenol
FET	Field Effect Transistor
FMNS	Flavin mononucleotide sodium salt
GO	Graphene oxide

G-FMNS	FMNS functionalized graphene
HOPG	Highly oriented pyrolytic graphite
IDE	Interdigitated electrode
LDA	Linear discriminant analysis
LOD	Limit of detection
LPE	Liquid phase exfoliation
MDS	Molecular dynamics simulation
MOS	Metal oxide semiconductor
MFC	Mass flow controllers
NDIR	Non-dispersive infrared
PME	Particle mesh Ewald
PMF	Potential of mean force
PANI	Polyaniline
PPy	Polypyrrole
PCA	Principal component analysis
QCM	Quartz crystal microbalance
RGO	Reduced graphene oxide
RDF	Radial distribution function
SDBS	Sodium dodecylbenzenesulfonate
SC	Sodium Cholate
SAW	Surface acoustic wave
SWCNT	Single-walled carbon nanotubes
SEM	Scanning electron microscope
SASA	Solvent accessible surface areas
SCC	Self-consistent charge
TPSA	Topological polar surface area

UV-VIS   Ultraviolet–visible spectroscopy

VOC   Volatile organic compound

VMD   Visual Molecular Dynamics

List of Figures

List of Tables

Chapter 1

Introduction

1.1   Air quality and human health

Air pollution is the presence of substances in the atmosphere that are detrimental to the health of humans and other living beings, which is at present one of the major global social and environmental issues accompanying with terrible consequences. According to the world health organization (WHO), there are estimated seven million people killed by the air pollution around the world each year [1]. The European Union (EU) has identified seven main air pollutants (excluding greenhouse gases): nitrogen oxides (NO_x), carbon monoxide (CO), particulate matter (PM), sulfur dioxide (SO_2), ozone(O_3), ammonia (NH_3), and volatile organic compounds (VOCs) [2].

Among these pollutants, NH_3 is an inorganic compound widely utilized in many industrial processes, including manufacturing, food processing, refrigeration systems, fertilizer production, etc [3]. However, even exposure to low concentrations of NH_3 adversely affects human health [4]. It irritates the eyes, the skin, and the respiratory tract if its concentration is exceeding the threshold value of 25 ppm in the environment [5]. Analogous to NH_3, phosphine (PH_3) is a colorless and, flammable, toxic gas, which is extensively utilized as a chemical dopant for silicon semiconductors and photovoltaic process applications in the semiconductor industry [6], as well as for the fumigation of durable agricultural commodities in the farming industry, such as cereal grain, pulses, tobacco and dried fruits, etc [7]. Nevertheless, PH_3 is extremely toxic and exhibits an acute lethal effect on humans and animals by inhibiting aerobic respiration at even extremely low concentration. To protect people
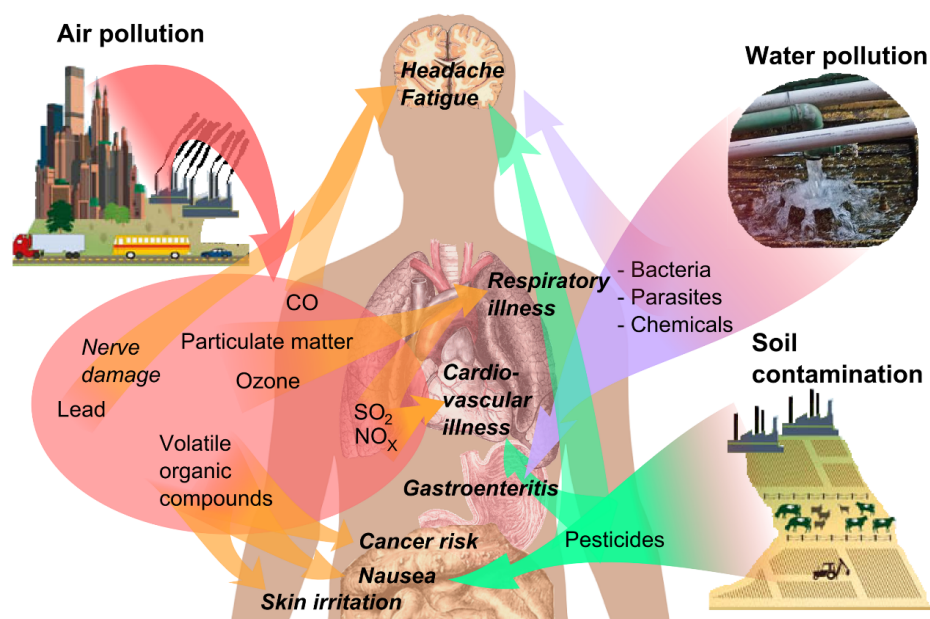
Figure 1.1 Major impacts of environmental pollution on human health [9].

from excessive NH_3 and PH_3 exposure at their work place, the American Occupational Safety and Health Administration (OSHA) has set the permissible exposure value for NH_3 as 50 ppm and for PH_3 as 300 ppb over an 8h work-shift per day, or 40h per week, respectively [8].

Another category of air pollutant, volatile organic compounds (VOCs), are organic chemicals with high vapor pressure at room temperature, among which some are prominent and representative indoor pollutants, such as benzene, toluene, ethylbenzene, xylene (BTEX), formaldehyde, acetaldehyde, etc [10]. The Unites States Environmental Protection Agency (U.S. EPA) estimates that the VOCs level in indoor air is typically 2-5 times higher than those of outdoor air [11]. Commonplace items in our dwellings such as building materials, paints, and furniture, cleaning agents and cosmetics etc., are potential sources of VOCs. Nevertheless, considerable evidence suggests that a substantial number of these VOCs could cause adverse health effects, including sensory irritation, respiratory symptoms (asthma, allergy, etc.), and even cancer [9], as shown in Fig. 1.1. Indoor air quality of residential units and workplaces has been a serious concern since we human beings spend more than 80% of lifetime indoors, including domestic residences and working places [12].
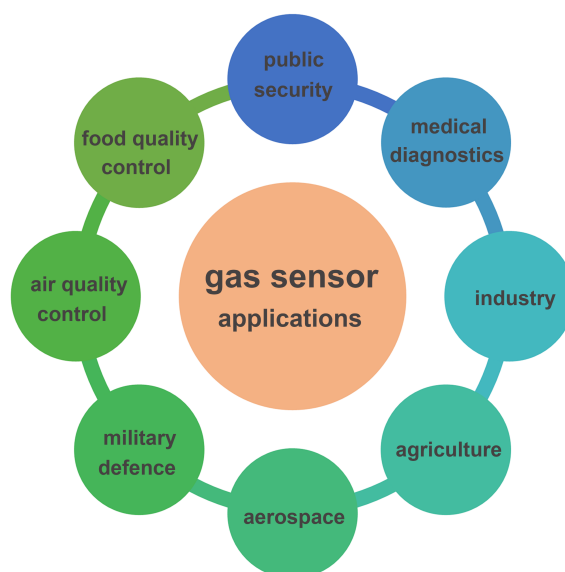
Figure 1.2 Overview of gas sensor applications.

Gas sensors play vital roles in monitoring and detecting hazardous gases, and ensuring public safety, air quality, or analyzing environments throughout many different fields [13], as summarized in Fig. 1.2. They are helpful not only in monitoring toxic gases in the atmosphere emitted from industry, but also in the control of indoor air quality (such as working places, indoor household) [14], and safety in the car. Their application is virtually countless in the industry and span across a lot of industrial branches, including automotive, underground mining, gas and oil industry, petrochemical industry, etc [15]. In agriculture, they are widely utilized as well, including plant/animal diagnostics, CO_2 gas monitoring, soil and water testing, meat/poultry inspection, etc [16]. Moreover, in aerospace aircraft, gas sensors are helpful to monitor the concentration of oxygen, carbon dioxide, and toxic gases in the environment atmosphere [17]. In military field, gas sensors facilitate the detection of chemical, biological, and toxin warfare agents, etc [18]. In the food processing industry, they are dedicated to ensure the food quality by detecting particular odors, which are released from rotten or spoiled food [19]. Another important application is to detect dangerous substances (e.g., explosive, flammable, combustible gases, etc.) [20], and maintain security and safety of the general public (e.g., public transportation, airline transportation, etc.). As an emerging application field, disease diagnosis *via* detection of disease-related VOCs using gas sensors (e.g., breath analysis) is attracting extensive attention currently. Various demonstrations have re-

cently been published, such as lung cancer [21], SARS-COVID-19 [22], diabetes [23], Alzheimer's [24], and Parkinson's disease [25].

During most of the aforementioned applications, gas sensors are capable to be interfaced with a control system so that emergency measures could be taken automatically [26]. Moreover, they could sound an alarm to operators in the working area where the leak is occurring, alarming them to evacuate from the dangerous district [27]. In this manner, the application of gas sensors could prevent accidents caused by gas leakages, thereby saving lives. Therefore, the development of highly efficient, sensitive, reliable, low-cost gas sensors has been of great significance for improving the work safety and life quality.

1.2 Gas sensors

Typically, gas sensors consist of a receptor component as well as a transducer component [28], as schemed in Fig. 1.3. The receptor represents sensing materials, which upon exposure to the analyte gas could give rise to some change of its own physical properties, such as conductivity, permittivity, work function, mass, etc. or emit heat or light [29]. The transducer component, on the other hand, is responsible for converting such a variation into an electrical signal (e.g., sensing response) like, current or voltage [30]. The sensor architecture is determined by the transducer utilized, while the receptor is generally integrated into the transducer [31].

According to the operating principle of the transducer, there are six general categories of gas sensors, including electrochemical (EC), optical, mass-sensitive, calorimetric, magnetic, and electrical type sensors [32], as illustrated in Fig. 1.4. Electrochemical gas sensors are those sensors, in which the gas molecules interact with the sensing electrodes associating an electrochemical reaction event (e.g., oxidation/reduction reaction) and this event could be further converted into an electrical signal [33]. Based on the signal output, electrochemical gas sensors could be classified as potentiometric, amperometric and conductometric type gas sensors. Electrochemical gas sensors are extensively utilized to detect oxygen in automotive application [34]. Optical gas sensors rely on the detection of changes of optical phenomena, such as light intensity, color or emission spectra, upon the analyte gas interacting with sensor receptor [35]. In accordance with applied optical properties,
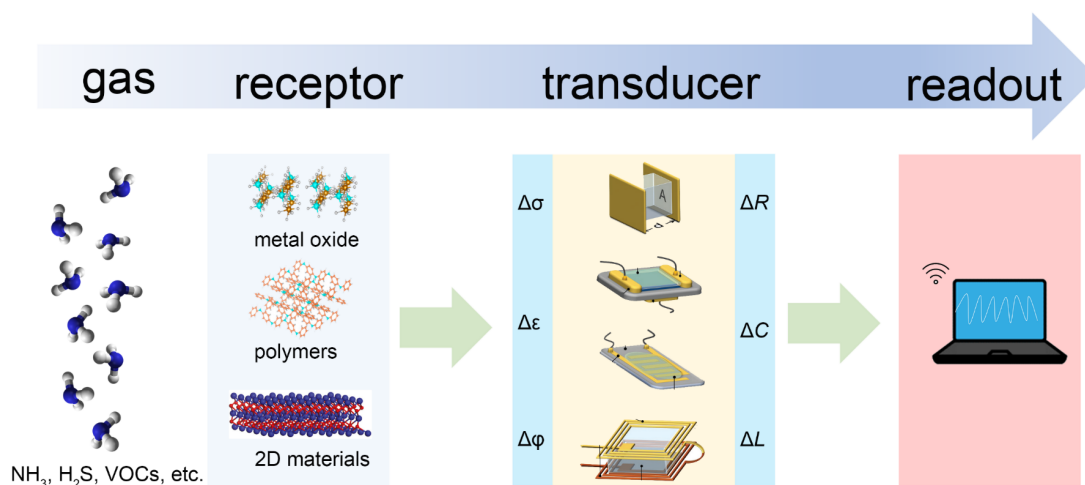
Figure 1.3 Schematic diagram of electrical gas sensor working principle. Gas molecules interact with the receptor (sensing materials), altering its physical properties, such as conductivity (σ), permittivity (ε) and work function (ϕ). The transducer component is responsible to convert the alternated physical properties into the variation of electric parameters, such as resistance (R), capacitance (C) and inductance (L). Finally, the circuit connected to the sensor gives rise to the sensing signal, which is in either current (I) or voltage (V) [30].

optical gas sensors could be further subdivided into several categories, such as absorbance type (e.g., non-dispersive infrared gas sensor, NDIR), reflectance type, luminescence type, fluorescence type, refractive index type, optothermal effect type and light scattering type gas sensors [36]. For instance, the infrared gas sensors detect trace gases by measuring the absorption of an emitted infrared light source through an air sample [37]. Optical gas sensors are widely utilized to detect carbon dioxide as well as a broad range of combustible gases [38]. Mass-sensitive gas sensors convert the change of mass at a specifically modified surface due to the gas adsorption on the receptor, into the change of a property of the substrate material [39]. Mass-sensitives gas sensors generally involve piezoelectric (e.g., quartz crystal microbalance, QCM) and surface acoustic wave (SAW) techniques [40, 41].

Calorimetric gas sensors interpret the temperature changes of receptors, which are generated by chemical reactions or adsorption of analyte gas, into an electrical signal [42]. They involve catalytic (catalytic bead, pellistors) [43], thermoelectric and pyroelectric types, which are extensively used to detect combustible gases [44]. Magnetic gas sensors rely upon the change of paramagnetic properties of an analyte gas, which are represented by some types of oxygen detectors [45]. Finally, electrical gas sensors are the most popular types, in which there are no electro-
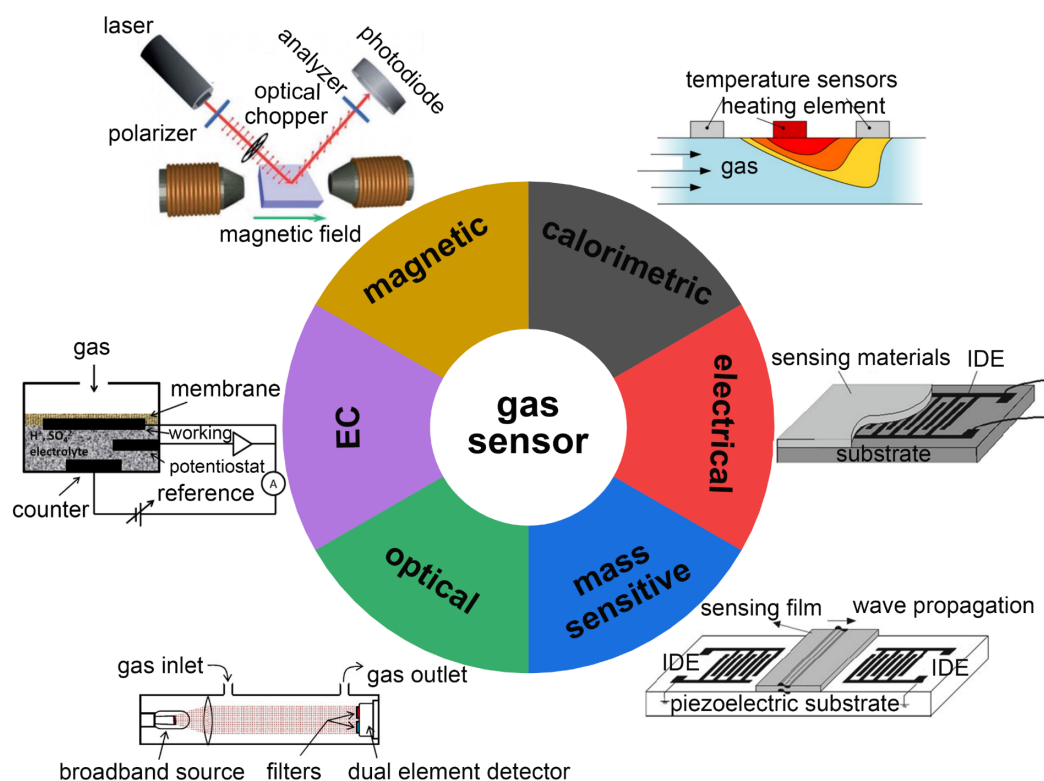
Figure 1.4 Classification of gas sensors based on the transduction working principles, including electrochemical (EC), optical, mass-sensitive, electrical, calorimetric and magnetic type sensors.

chemical reaction events occurring, instead, the signal arises from the change of electrical properties of receptor (sensing materials) owing to the surface interaction with analyte gas (e.g., charge transfer, reversible redox process, etc.) [46]. A large group of gas sensors are contained in the family of electrical gas sensors, such as chemiresistive type (e.g., metal oxide, metal, polymer, one-dimensional material, twO dimensional material, or semiconductor conductometric sensors, etc.), capacitive type, and semiconductor type (e.g., work-function, Schottky barrier, FET, etc.), as shown in Fig. 1.5.

So far, numerous gas sensors have been developed based on the aforementioned principles, nevertheless, the majority of gas sensors exhibit some common drawbacks, such as relatively high cost, poor sensitivity and selectivity, sophisticated design, a need for additional equipment, or lack of portability [47]. Among them, chemiresistive sensors, working on the mechanism of variation in resistance upon exposure to analyte gases [42], have attracted significant attention and become
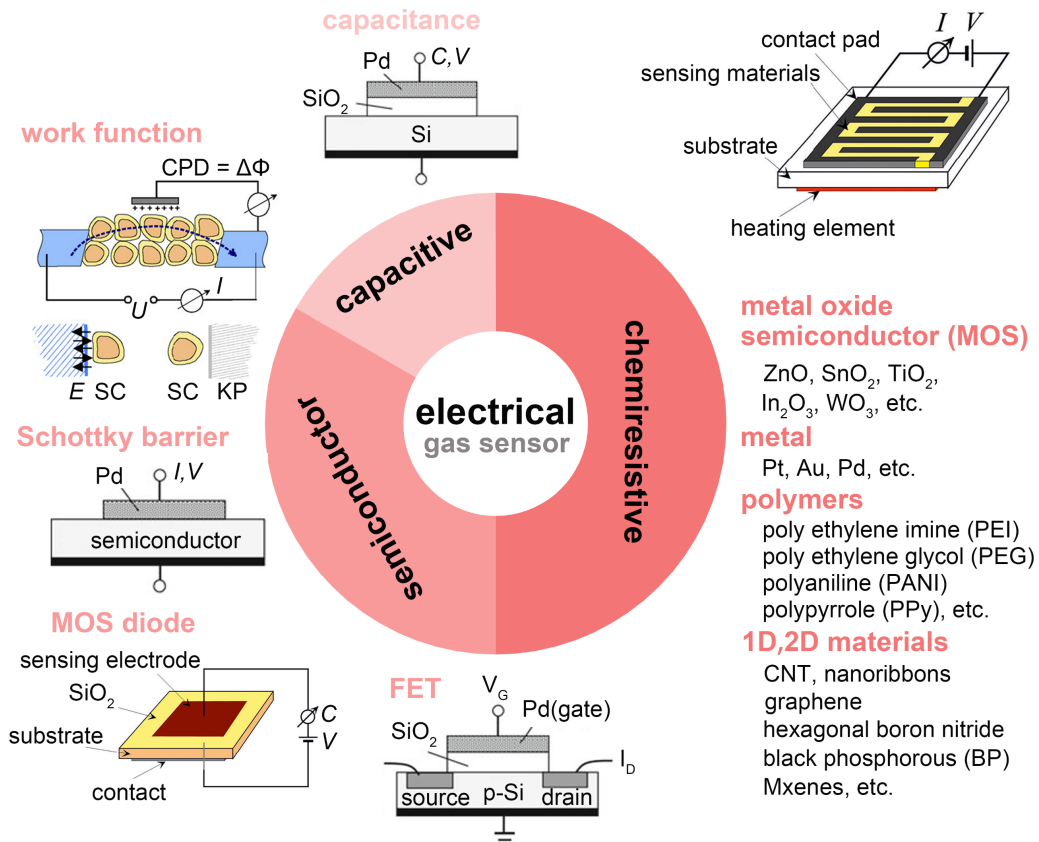
Figure 1.5 Classification of electrical gas sensors based on the output signal of the transducers, containing chemiresistive, capacitive and semiconductor type sensors.

a hot research topic due to their multiple advantageous characteristics, such as simple fabrication/circuitry, easy operation, high sensitivity, fast response/recovery, good stability, low cost, ability to detect a wide spectra of gases, and compatibility with miniaturization as well as integration for portable applications, etc [48]. The typical structure of a chemiresistive type gas sensor is depicted in Fig. 1.6, which comprises four essential components: sensing materials, interdigitated electrodes (IDE), insulating substrate (e.g., SiO_2, ceramic, etc.), and a heater element.

In order to evaluate the performance of different gas sensors, some critical quality indicators have to be taken into consideration, such as sensitivity, selectivity, response and recovery time, limit of detection (LOD) and resolution, stability, and working temperature [49]. In a chemiresistive gas sensor, sensitivity (S) refers to the relative change of resistance upon exposure to analyte gas [50], which could be
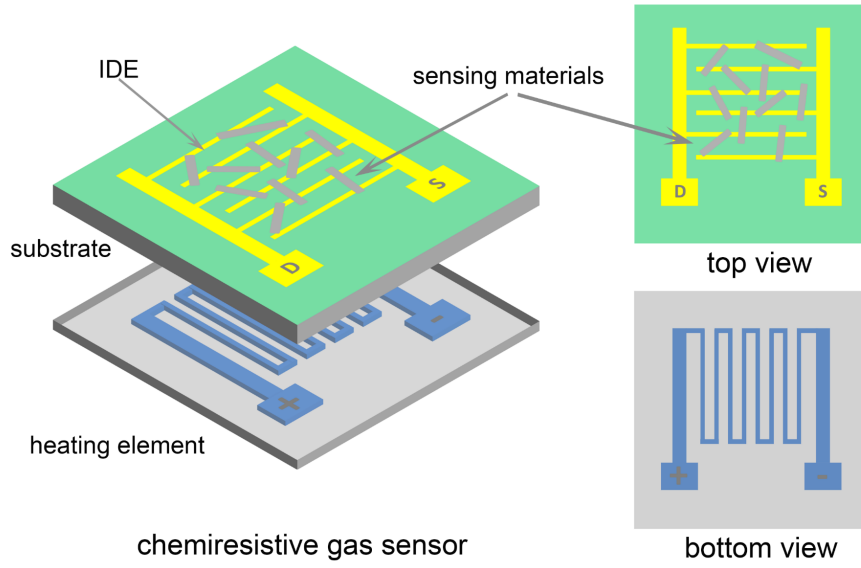
Figure 1.6 Typical structure of chemiresistive type gas sensor, containing four components, interdigital electrodes (IDE), sensing materials, silicon substrate and heating element.

described as the ratio between the absolute resistance change upon exposure to analyte gas and the resistance under the reference medium (e.g., ambient air):

$$S(\%) = (R_g - R_a) \, / \, R_a \times 100 \tag{1.1}$$

Where R_a is the resistance of gas sensor under the reference medium, or termed baseline resistance, and R_g is the resistance of gas sensor upon exposure to the analyte gas.

Selectivity indicates the ability of gas sensors to differentiate the group of target gases or single gas in the gas mixture [51]. Response time characterizes the period during which the resistance value increases/decreases by a certain percentage (e.g.,63.2% or 90%) of its baseline value at the certain gas concentration [52]. Likewise, recovery time determines the period required for the gas sensor to recover to its baseline value fully or partially (e.g., 90%) after switching off the analyte gas supply. The limit of detection represents the lowest gas concentration that could be distinguished from the noise [53]. The lowest concentration difference, corresponds to the resolution of the gas sensors. The stability denotes the ability to provide reproducibility of measurement results in a prolonged usage.
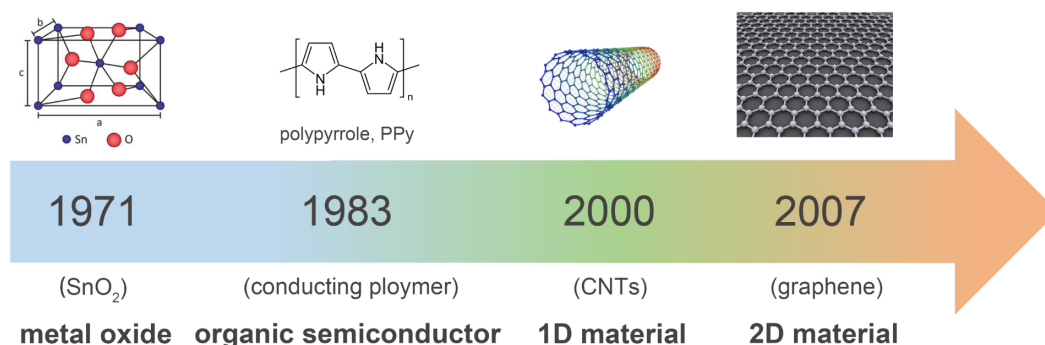
Figure 1.7 Evolution of sensing material for chemiresistive type gas sensors since the first commercial gas sensor (SnO$_2$) in 1971.

1.3   Overview of chemiresistive type gas sensors

So far, chemiresistive gas sensors have been used for over 50 years, as summarized in Fig. 1.7. In 1962, Seiyama demonstrated the sensing characteristics of ZnO thin film relying on simple electrical devices [54]. When the sensor operated at 485 ^{o}C, the sensing response to propane was 100 times higher than the thermal conductivity detector utilized at that time. In 1967, Shaver reported the sensitivity of a number of semiconductor metal oxides (e.g., WO$_3$, MoO$_x$, Cr$_2$O$_3$, TiO$_2$, Fe$_2$O$_3$, Nb$_2$O$_5$, NiO, etc.) could be increased significantly by introducing the noble metals as foreigner additives, such as Pt, Pd, Ir, Rh, etc [55]. In 1971, Taguchi fabricated and patented the first SnO$_2$ based chemiresistive gas sensors for practical application, and meanwhile, he founded Figaro Inc. to commercialize these devices, which were widely used for domestic gas alarms of fire protection [56]. In his work, he found that SnO$_2$ exhibited a lot of merits for gas sensing application compared with the other metal oxides, such as higher sensitivity, low working temperature, and thermal stability. The semiconductor metal oxides for the gas sensing application are categorized into n-type and p-type, among which the n-types metal oxides gas sensor accounts for the majority [57]. The sensing characteristics for both types of gas sensors are reviewed in Table. 1.1.

The resistances of n-type semiconductor metal oxide-based gas sensors, in which the electrons are the majority carriers, decrease when they are heated, because electrons on the valence band are excited to the conduction band, the number of electron charge carriers increase [65]. When the metal oxides materials are heated

Table 1.1 Sensing characteristics of both types (n-type, p-type) semiconductor metal oxide gas sensors. E_g: band gap; T: work temperature [58–64].

Metal oxide	E_g(eV)	$T(^oC)$	Pros	Cons
SnO_2	3.6	200-500	High sensitivity Low LOD Chemically stable	Low selectivity
ZnO	3.37	300-500	Mechanical stable Chemically stable High electron mobility Suitability to doping Non-toxicity	Low selectivity
TiO_2	3.1(rutile)	400–1000	Lower cross-sensitivity	Low selectivity Unstable repeatability Unstable stability
WO_3	2.75	200	Fast response/recovery High sensitivity	Low selectivity
CuO	1.2	200	Catalytic activity High stability Tolerance to humidity	Low selectivity
NiO	3.6–4.2	200–600	Catalytic activity Work at high temperature Chemical stability Good conductivity	Low selectivity
Cr_2O_3	3.4	200	Catalytic activity Mechanical stable Chemically stable	Low selectivity

to different temperature T in the ambient air, various forms of oxygen ions are generated on the surface of metal oxides [66], such as O_2^- (T=100-200 ^{o}C), O^- (T=200-300 ^{o}C), O^{2-} (T >300 ^{o}C), as the adsorbed oxygen molecules withdraw electrons from the conduction band of metal oxides [67]. This further results in a decrease of the concentration of electron carriers, thus an increase of the resistance of gas sensors. Upon exposure to the reducing gas, such as CH_4, C_2H_4, CO, etc., the chemical reaction occurs between these oxygen ions (O_2^-, O^-, O^{2-}, etc.) adsorbed on the surface of n-type semiconductor metal oxides and the reducing gas [68], in which electrons are released and retracted to the conduction band of the n-type semicon-

ductor metal oxides, giving rise to a decrease of the sensor resistance, as illustrated in Fig. 1.8 and Fig. 1.9.

Likewise, the sensor resistance of p-type metal oxide gas sensors decreases when the temperature arises. In the ambient environment, p-type metal oxide gas sensors, in which the holes are the majority carriers, generate more holes since oxygen molecules are adsorbed on the surface of metal oxides and form oxygen ions by withdrawing the electrons excited from the valence band [69]. In this step, the population of hole carries increase, resulting in the decrease of the sensor resistance. Upon exposure to reducing gas, chemical reactions occur between oxygen ions and reducing gas, and electrons are generated, which are poured into the valence band of metal oxide and recombine with hole charge carriers [70]. The recombination step causes a decrease of the population of hole charge carriers, and thus leading to the increase of the resistance of p-type metal oxide gas sensors. As for the case of exposure to oxidizing gases, the resistance change is inverse to the previous discussion.

Till now, metal oxides are one of the most popular, diverse, and most likely, the largest group of sensing materials owing to their various merits, such as low cost, facile fabrication, easy use, a wide spectrum of gas detection including combustible gases and toxic gases [71]. The limitations for these sensing materials, however, contain low selectivity, high working temperature, high power consumption, baseline resistance drift, etc [72].

In the past 50 years, a myriad of novel sensing materials have been developed. In 1983, Nylabder reported the application of polypyrrole (PPy) for the detection of ammonia [73], which marked the first work of chemiresistive gas sensors using conducting polymer materials. Besides, some other conducting polymers were also widely investigated as sensing materials, such as polyaniline (PANI) [74], poly (3,4-ethyleneedioxythiopene) (PEDOT) [75], etc. Navale reported the development of highly sensitive PPy based gas sensors for NO_2 detection at 10 ppm [76]. Xie developed PANI film-based gas sensor for NO_2 detection and found the pure PANI film prepared by Langmuir-Blodgett technique exhibit better sensitivity to NO_2 than PANI film prepared by self-assembly technique [77]. Seekaew presented the PEDOT based gas sensor using ink-jet printing method, which demonstrated high response and high selectivity to NH_3 at low concentration (25-1000 ppm) at room tempera-
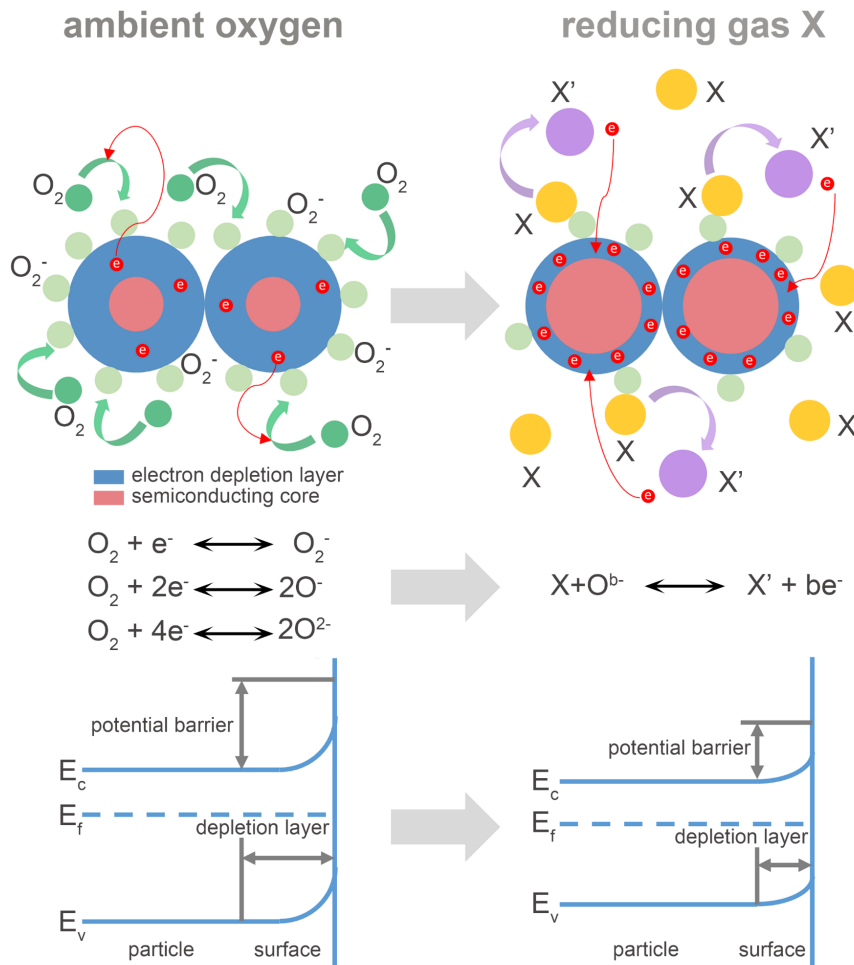
Figure 1.8 Schematic diagram of sensing mechanism of n-type semiconductor metal oxide gas sensor in ambient air and reducing gas X (e.g., CO, CH_4, C_2H_4, etc.) [13].

ture [78]. Conducting polymers-based gas sensing materials have many advantages, such as good sensitivity to redox-active gases, such as NH_3, NO_2, SO_2, H_2, H_2S, and VOCs, low work temperature (e.g., room temperature), good mechanical properties, easy modification, and simple synthesis [79]. The main drawbacks are instability, irreversibility, and poor selectivity for long-term use [13]. Besides, the environment humidity and temperature exert a great influence on their physical and chemical properties since conducting polymers are usually thermally instable [80]. The conductivity of pure polymer film is very low, in order to achieve a good conductivity suitable for sensing applications, doping treatment is indispensable [81].

In the last decades, with the successful discoveries of a myriad of low dimensional nanomaterials, such as nanoparticles/nanodots, nanowires/nanotubes, 2D
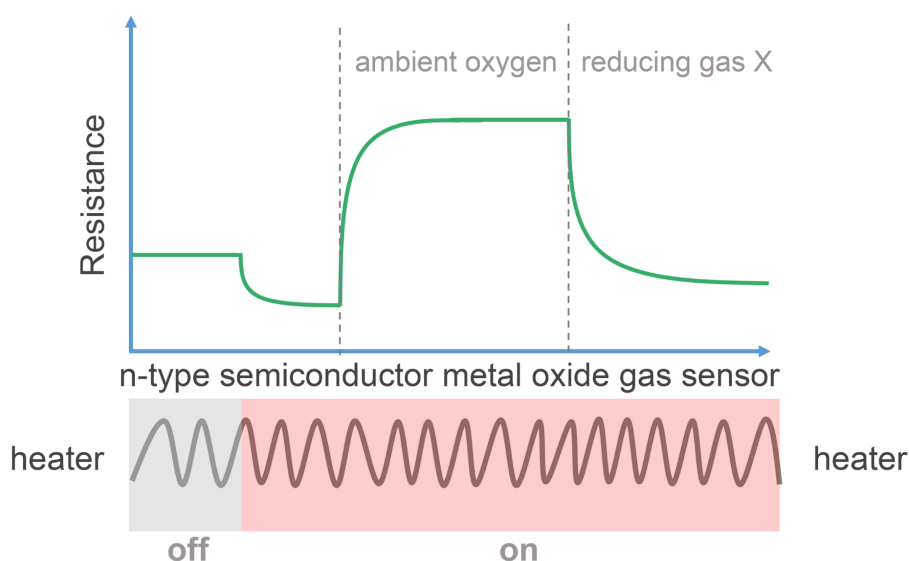
Figure 1.9 The resistance evolution of n-type semiconductor metal oxide gas sensors with respect to different conditions, such as operation temperature and exposure to reducing gas X (e.g., CO, CH_4, C_2H_4, etc.)

materials, etc., considerable effort has been made to investigate these nanomaterials as sensing materials in chemiresistive type gas sensors. In 2000, Kong firstly presented the development of single-walled carbon nanotubes (SWCNT) based gas sensor for the gas detection (NO_2 and NH_3) and their work laid foundation of SWCNT in the gas sensing application [82]. The resistance of the SWCNT based gas sensors were observed increased or decreased dramatically upon exposure to gases such as NO_2 or NH_3, respectively. Carbon nanotubes are very promising gas sensing materials due to their ultra-high surface-to-volume ratio, excellent conductivity and mechanical stability [83]. For example, they are compatible with B- and/or N- groups doping, rending them widely utilized for the detection of a large range of gases [84]. In a similar manner, with the functionalization of polar groups, such as –COOH , carbon nanotube-based gas sensors exhibit a stronger response towards the VOCs since the adsorption efficiency of the VOCs could be enhanced owing to the intermolecular interaction (dipole-dipole interactions, hydrogen-bonding interactions, etc.) between the functional groups and the VOC molecules [85, 86]. However, technological carriers make costly the fabrication of high quality and purity nanotubes, resulting in commercialization impediments [87]. More recently, graphene emerged as a new 2D material with exceptional properties that could also be exploited for gas sensing applications, as it will be described next.

In addition to employing single type sensing component as sensing materials, a lot of hetero structure materials (more than one type of sensing components) have been widely reported as gas sensing materials by modulating the factors affecting the receptor function and/or transducer function of the host sensing materials. In this case, it's possible to complement the limitations of each sensing component and maximize the merits of each sensing component. In this context, the receptor function refers to the ability of the sensing materials to interact with the analyte gas [88], while the transducer function concerns the ability to convert the signal caused by the chemical interaction of sensing materials into electrical signal [89]. The physical contact surface between two different materials is defined as heterojunction. Once the electrical contact is established at the heterojunction, the Fermi levels line up to the same energy owing to the mismatch in chemical-potential, which results in the charge transfer between these two different materials, further leading to the formation of charge depletion layers [48]. For example, it has been widely reported that an introduction of foreign particles such as noble metal nanoparticles (e.g., Pd, Au, Pt, Ag, etc.), metal oxides (e.g., SnO_2, CuO, TiO_2, etc.) on the host sensing materials (e.g., conducting polymers, carbon nanotubes, graphene, etc.) can modify the receptor function and enhance the sensitivity as well as the selectivity.

1.4 Graphene

Since its discovery by Geim and Novoselov in 2004, graphene, a two dimensional (2D) single-atom-thick layer of sp^2 hybridized carbon atoms arranged in a honeycomb lattice, has been acclaimed as a miracle material owning to its extraordinary properties [90]. It has ultrahigh Young's modulus, excellent thermal conductivity and electrical conductivity, superb optical transmittance, complete impermeability to any gases [91]. In particular, graphene possesses remarkable ultrahigh charge-carrier mobility at room temperature [92] and ultrahigh specific surface area [93], which makes graphene a promising candidate material in highly sensitivity detection applications.

To date, two distinct strategies have been developed for graphene synthesis: exfoliating graphite towards graphene (termed 'top-down') and build-up graphene from molecular building blocks (termed 'bottom-up') [94], as shown in Fig. 1.10. The
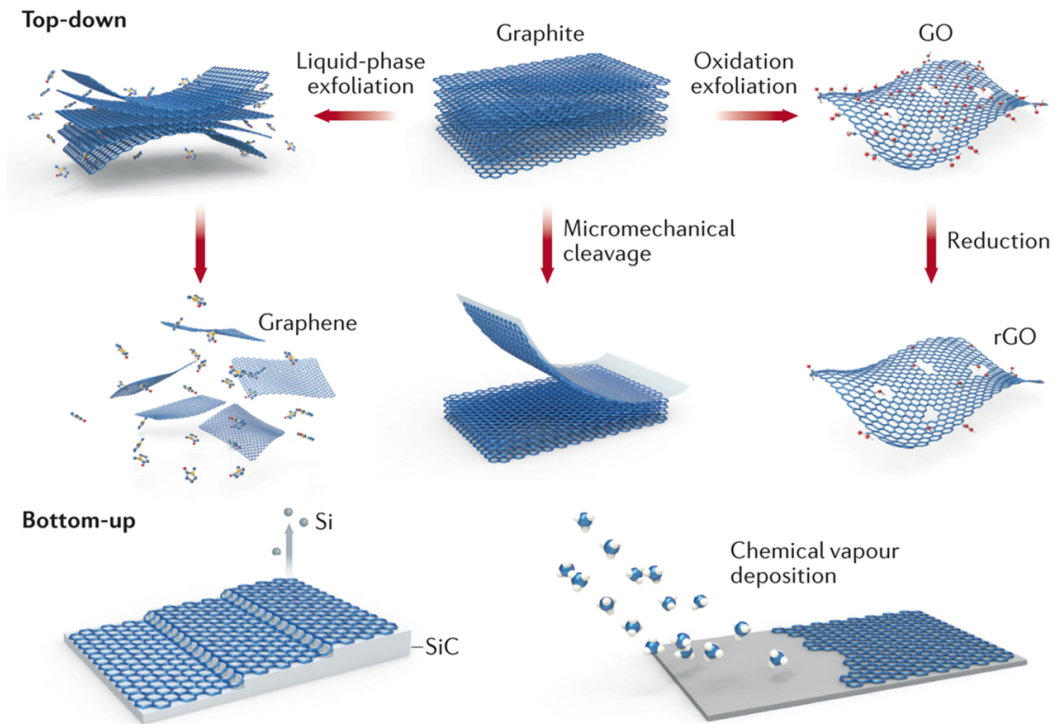
Figure 1.10 Major synthesis methods of graphene based on top-down and bottom-up strategies [94].

top-down strategy generally includes mechanical exfoliation of highly oriented py-rolytic graphite (HOPG) [95], liquid phase exfoliation of graphite [96], chemical oxidation/exfoliation of graphite followed by reduction of graphene oxide (GO) [97], etc. The bottom-up approaches for graphene synthesis involves epitaxial growth on metallic substrates by means of chemical vapor deposition (CVD) [98], thermal decomposition of SiC [99], organic synthesis based on precursor molecules [100], etc. These synthesis methods could be categorized by the quality of the resulting graphene and its potential applications [91]:

- Graphene or chemically reduced/modified graphene oxide flakes for composite materials, conductive paints, sensors, etc.

- Planar graphene for lower-performance active and non-active devices.

- Planar graphene for high-performance electronic devices.

The properties of a particular grade of graphene depend on the synthesis approaches, the quality of material, defects, etc., as illustrated in Fig. 1.11.
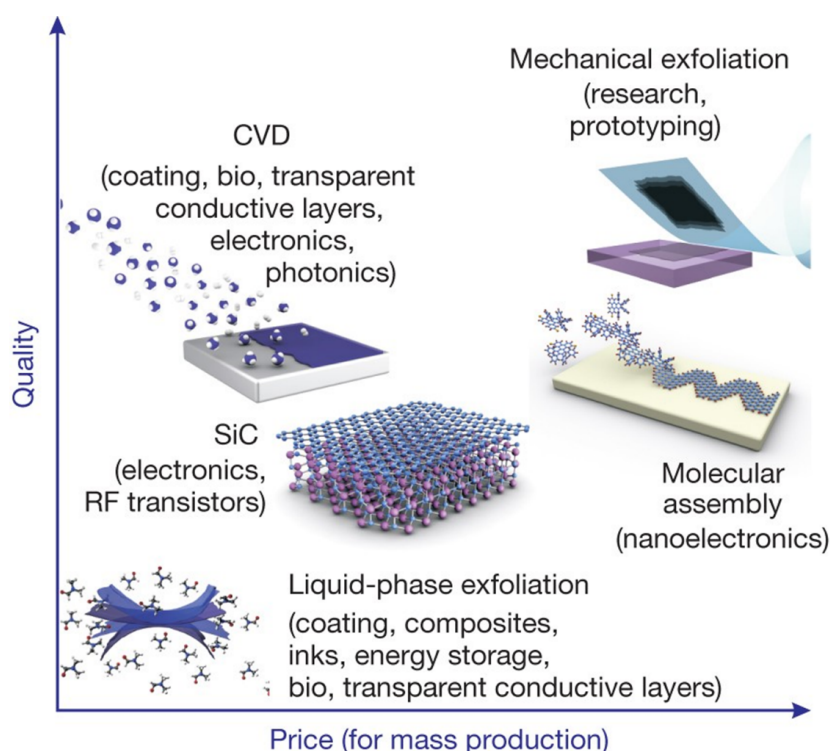
Figure 1.11 Comparison of various methods of mass-production of graphene in terms of quality and price [91] [94].

1.5   Graphene-based gas sensors

The first graphene-based ammonia gas sensor was reported by Andre Geim's group employing the micromechanical cleavage of graphite on an oxidized silicon substrate in 2007 [101]. The initial response of 4% upon exposure to 1 ppm NH_3 at room temperature was followed by saturation, and the sensor could recover to the initial state by annealing at 150 ^{o}C in vacuum. In 2009, the follow-up work was carried out by Johnson's group, confirming that the intrinsic response of graphene towards ammonia gas, however, was surprisingly small (1%) even upon exposure to 1000 ppm NH_3 [102]. First principles calculations showed that the residue contamination introduced from conventional nanolithography process could play a significant role in enhancing the response of graphene. The calculation results indicated that there exists weak bonding (around20 meV) and charge transfer (around 0.027 e^-) between NH_3 and graphene [103]. The aforementioned work inspired a pathway to facilitate the application of graphene towards gas sensing *via* intentional functionalization.

Thereupon, chemically modified graphene-based ammonia sensors gained prominence, such as reduced graphene oxide (rGO) based ammonia sensors [104], rGO/metal particles hybrid based ammonia sensors [3], rGO/metal oxide hybrid ammonia sensors [105], rGO/polymers hybrid material based ammonia gas sensors [106], etc. It is well established that the original perfect atomic lattices of graphene are potentially sacrificed during the chemical modification process owing to the formation of covalent bonds introducing functional groups, which severely damages the intrinsic electrical properties of graphene [107]. Additionally, chemical modifications usually require harsh reaction conditions as well as complex processing [108]. Some works on pristine graphene-based ammonia sensors were reported as well, involving vertically aligned graphene-based ammonia sensors [109] and chemical vapor deposited (CVD) graphene-based ammonia sensors [110]. CVD strategy can yield high quality graphene whilst it comes along with several disadvantages, for example, expensive and sophisticated equipment, toxic gaseous by-products and complicated transfer steps, etc [102]. These aforementioned limitations of rGO or CVD graphene seriously restrict the efficient commercial application of graphene-based ammonia sensors. Thus, graphene-based gas sensors with the following characteristics, e.g., facile fabrication, environmentally friendly process, biocompatible synthesis, low cost, and scale-up capability, are highly in demand at this moment.

1.6   Scope of this thesis

In this work, a facile, environmentally friendly, biocompatible, and compatible to mass production, low-cost approach to synthesize graphene dispersions, which could be utilized as gas sensing materials in chemiresistive format. The developed gas sensors utilizing specifically functionalized graphene exhibit excellent performance towards NH_3 detection at room temperature in terms of sensitivity. In combination with machine learning techniques, the selectivity could be significantly enhanced, which demonstrated excellent discriminability towards volatile organic compounds, NH_3/PH_3, etc. The developed sensing platform may facilitate miniaturization of smart gas sensors, digitization of odors, and distinction of various gases in numerous emerging applications. The structure of this thesis is as follows:

- The chapter 2 introduces the materials and methods involved in this work. The instruments servicing for material preparation, and the methods of graphene preparation, sensor fabrication, and material characterization are detailed in this section. Two important techniques employed in this work, molecular dynamic simulation tool and machine learning approach are briefly introduced as well.

- The chapter 3 presents the simulation work on the investigation of the stabilization mechanism of functionalized graphene in dispersant aqueous solution. In terms of FMNS morphology on graphene surface, the potential of mean force of functionalized graphene flakes and the surface coverage of graphene flakes, the underlying stabilization mechanism are elucidated.

- The chapter 4 demonstrates the experimental work on the development of FMNS functionalized graphene-based gas sensor and the sensing performance towards NH_3 detection. In addition, the role of FMNS on NH_3 gas sensing and the sensing working mechanism are discussed, respectively.

- The chapter 5 presents the discrimination and identification performance of the developed graphene-based e-olfaction platform towards 4 different odors assisted with machine learning techniques. In addition to the sensing measurement towards individual odor, the sensing response towards binary odor mixture is discussed as well and compared with the human olfactory perception exposed to odor mixtures.

- The chapter 6 is a practical application example for graphene-based e-olfaction towards industrial gases (PH_3, NH_3). The performance of the e-olfaction is evaluated in term of sensing sensitivity, precision, selectivity, etc. Meanwhile, the potential mechanism of the enhance selectivity is discussed *via* molecular dynamic simulation.

- The chapter 7 finalizes this thesis with conclusions and outlook, containing several open issues that have to be addressed before the real practical application of the e-olfaction sensing platform.

Chapter 2

Materials and methods

2.1 Materials

The materials utilized in this work for graphene dispersion preparation are summarized in the Table. 2.1.

2.2 Instruments

The instruments used for graphene dispersion preparation are summarized in the Table. 2.2.

2.3 Graphene dispersion preparation

In this work, the liquid phase exfoliation (LPE) method is employed to synthesize graphene dispersion as sensing materials, which is low-cost and suitable for massive production [96]. The dispersants not only could assist the exfoliation process, but also act as stabilizer to keep graphene well dispersed in aqueous media. In comparison to "modified Hummers' method", graphene flakes are functionalized non-covalently by the LPE method, which largely preserves the excellent electrical properties of graphene [107]. Depending on the specific work, different dispersants were used to achieve well stabilized graphene dispersions with different

Table 2.1 Materials in this work.

Materials	Specifications	Supplier company
Graphite	crystalline, -20+84 mesh, 99.9%	Alfa Aesar
FMNS	Riboflavin 5'-phosphate sodium salt, 73-79%, fluorimetric, $C_{17}H_20N_4O_9PNa$	Sigma-Aldrich
Eucalyptol	99.0%, $C_{10}H_{18}O$	Sigma-Aldrich
2-nonanone	99.0%, $C_9H_{18}O$	Sigma-Aldrich
Eugenol	98.0%, $C_{10}H_{12}O_2$	Sigma-Aldrich
2-phenylethanol	99.0%, $C_8H_{10}O$	Sigma-Aldrich
CuPc	Copper phthalocyanine-3,4 ', 4 ", 4 ''' - tetrasulfonic acid tetrasodium salt, $C_{32}H_{12}CuN_8O_{12}S_4Na_4$	Sigma-Aldrich
APTS	8-Aminopyrene-1,3,6-trisulphonic acid trisodium salt, $C_{16}H_8NO_9S_3Na_3$	VWR
NH_3	50 ppm, 10000 ppm	Air Products
PH_3	50 ppm	Air Products
NO	1000 ppm	Air Products

functional groups, such as flavin mononucleotide sodium (FMNS), 8-aminopyrene-1,3,6-trisulphonic acid trisodium salt (APTS), or copper phthalocyanine-3,4', 4", 4'''-tetrasulfonic acid tetrasodium salt (CuPc). With different dispersants, the preparation protocols are almost the same. The dispersant selection is determined by the specific application in this thesis work, for instance, FMNS was utilized to develop graphene-based ammonia gas sensors since it could bind ammonia molecules, APTS was applied to develop graphene-based odor sensors since it intended to form inter-molecular interaction with odor molecules, CuPc was suitable to develop graphene-based phosphine gas sensor since phthalocyanine derivatives is sensitive to detect analyte gases at ultra-low concentration.

To be specific, the protocol to prepare graphene dispersion with FMNS is demonstrated as an example, which is partially from my published article [111]. The typical procedure for graphene exfoliation was as follows: 5 mL FMNS aqueous solution at a concentration of 1 mg/mL was added into 5 mL graphite powder aqueous solution

Table 2.2 Instruments in this work.

Instruments	Model and company
Horn-type sonicator	Branson Digital Sonifier, Model 250-D, US
Centrifuge	Eppendorf, MiniSpin plus, Germany
Bath sonicator	VWR ultrasonic cleaner, type: USC 300 TH, HF 45 kHz, 80 W, US
Tip probe station	Karl Suss MicroTech, Garching, Germany
Source Meter	Keithley, 2604B, US
Function Generator	Sony Tektronix, AFG320, US
Digital Oscilloscope	Tektronix, TDS3014B, US
MFC	Mass Flow Controllers, GF040C, Brooks Instrument, US

at a concentration of 30 mg/mL, then the mixture was sonicated for 2 h incubated in an ice bath utilizing a horn-type sonicator at a 50% amplitude. Afterwards, the obtained solution was left to stand overnight. To remove the excess FMNS, the suspensions were centrifuged at 14,500 rpm for 2 min, and the top 80% supernatant was removed. The sediment was then re-dispersed in deionized (DI) water to the original volume followed by sonication for 10 min in an ice bath. The re-dispersion was then executed following the former step once time. Subsequently, the obtained suspensions were centrifuged at 4,000 rpm for 2 min, and the top 50% supernatant was used as FMNS functionalized graphene (G-FMNS) dispersion for further treatments, such as dilution treatment and freeze-drying treatment. The sediment containing the large platelets and un-exfoliated graphite particles was discarded.

2.4   Sensor device fabrication

The development of gas sensor device contains two main steps: fabrication of interdigital electrodes (IDEs) and fabrication of sensing elements. IDEs are fabricated employing a standard photolitography process as reported in our previous publication [112]. Firstly, the IDEs pattern were fabricated on Si substrate (p-type, 300 nm SiO$_2$) using photolithography techniques. 15 nm chromium and 100 nm gold were then deposited on the substrate via thermal evaporation and lift-off process. After that, the bare devices were cleaned with acetone and isopropanol, respectively. Lastly, the devices were heated to 100$^o C$ for 5 min in order to remove residual solvents and naturally cooled down to room temperature. The finger width and the gap size of the IDEs were 4 µm and 3 µm, respectively. The area of the whole chip was 2 cm^2, which contained two pads (18 mm^2) and IDEs. IDEs themselves were used active area for sensing materials deposition in next step. The fabrication of IDEs in the whole thesis work were carried out by my colleague Luis Antonio Panes-Ruiz.

While many authors employ non-deterministic methods to deposit graphene and other sensing materials on IDEs, such as drop casting, dip coating, etc., the alternating current (AC) induced dielectrophoresis (DEP) approach was employed to transfer graphene flakes on the IDEs in a deterministic way to improve the yield and the quality of the contact. The deposited graphene flakes could bridge the adjacent Au electrodes forming a homogeneous flake network [113]. The DEP parameters, including the peak-to-peak voltage (Vpp), frequency of applied signal (f), and processing time (t), exert a great influence on the morphology of deposited materials. The optimal DEP parameters were as: Vpp = 10 V, f = 200 kHz, and t = 30 s. A typical DEP process was as follows: 10 μL dispersion was pipetted onto the IDE chip in the probe station (Karl Suss, Garching, Germany) for 30 s followed by rinsing with DI water and drying with a N$_2$ gun. The fresh sensor chip then could be ready for use.

2.5   Graphene characterization techniques

In this work, functionalized graphene flakes were characterized by the below techniques, including Raman spectrum, Scanning Electron Microscope (SEM), Atomic Force Microscopy (AFM), UV-VIS absorption spectra, and Attenuated Total Reflectance-

Table 2.3 Characterization instruments.

Instrument	Model and company
Raman spectrum	Renishaw inVia BASIS spectrometer system, laser excitation wavelength 532 nm, UK
SEM	ZEISS, GeminiSEM 500, Germany
AFM	AFM Multimode 8, Bruker, Germany tapping mode
UV-VIS absorption spectra	Agilent Cary 60 Spectrophotometer
ATR-FTIR spectrum	IRAffinity-1S, Shimadzu, Japan, transition mode

Fourier Transform Infrared (ATR-FTIR) spectrum, etc. Raman spectrum was employed to characterize the quality of achieved graphene, as well as the layer information. SEM was utilized to visualize the morphology of functionalized graphene via liquid phase exfoliation and the deposited graphene on electrodes. AFM was utilized to characterize the layer information of the flakes. UV-VIS absorption spectra and ATR-FTIR spectrum were employed to verify the successful functionalization. The AFM characterization was done by Dr. Huanhuan Shi. The UV-VIS absorption spectra, Raman spectra characterization was done by was done by Dr. Vyacheslav Khavrus. The SEM characterization were done by me with the supervision of Dr.Markus Löffler. I am very thankful for their support. The detailed specification of these characterization techniques is presented in Table. 2.3.

2.6   Gas sensing measurement

The gas sensing measurements were implemented on a custom-made gas sensing setup, as schemed in Fig. 2.1, or after slight modification of the gas sample-delivery system. The setup contains three parts: sample-delivery system, gas sensing reaction chamber and signal acquisition system. Both analyte and carrier gases were introduced through the sample-delivery system and their flow rates were controlled with mass flow controllers (MFC). The flow rates ratio of both were determined by the target concentration of the analyte gas set under the frame of pre-defined ex-

perimental tasks. A complete sensing test contained both exposure phase as well as recovery phase. In the exposure phase, the carrier gas acts in dual roles, delivering analyte gas molecules to the gas chamber as well as diluting it to a certain desired concentration. The diluted analyte gas is delivered into the gas chamber and then interacts with the sensing materials on the sensor device due to the adsorption reaction, which further induces the resistance change of the sensor device. Meanwhile, the current signal of the sensor is monitored and displayed on the server PC. All these current information with respect to the operation time is recorded and saved for further use.

For instance, in the NH_3 sensing experimental task [111], the gas sensing procedure was as below. The exposures to analyte gas were followed by a recovery time under pure N_2 flow (2000 sccm/min). In this thesis work, in order to shorten the recovery time of graphene-based gas sensors, a larger flow rate (e.g.,2000 sccm/min) of pure N_2 was applied. A constant direct voltage of 0.1 V was applied to the sensors and the current was recorded in a real time with a source meter. The normalized sensing response was employed to evaluate the sensing characteristics of all gas sensors [114], which is defined as the relative change of sensor resistance and calculated using the below formula:

$$S(\%) = (R_{(t)} - R_{(0)}) \: / \: R_{(0)} \times 100 = (I_{(0)} - I_{(t)}) \: / \: I_{(t)} \times 100 \qquad (2.1)$$

Where $\Delta R_{(t)}$ is the resistance difference before analyte gas exposure and during analyte gas exposure, t is the time, $R_{(0)}$ and $I_{(0)}$ are the resistance and current before analyte gas exposure (t=0), respectively. $I_{(t)}$ is the current monitored during the exposure period. The achieved sensing response S was used as a critical parameter to evaluate the performance of the sensor device.

2.7   Molecular dynamic simulation method

In this work, in order to elucidate the underlying mechanism behind the experimental observation, molecular dynamic simulations (MDS) were conducted. All the molecular dynamic simulations were performed on GROMACS 5.1.2 platform
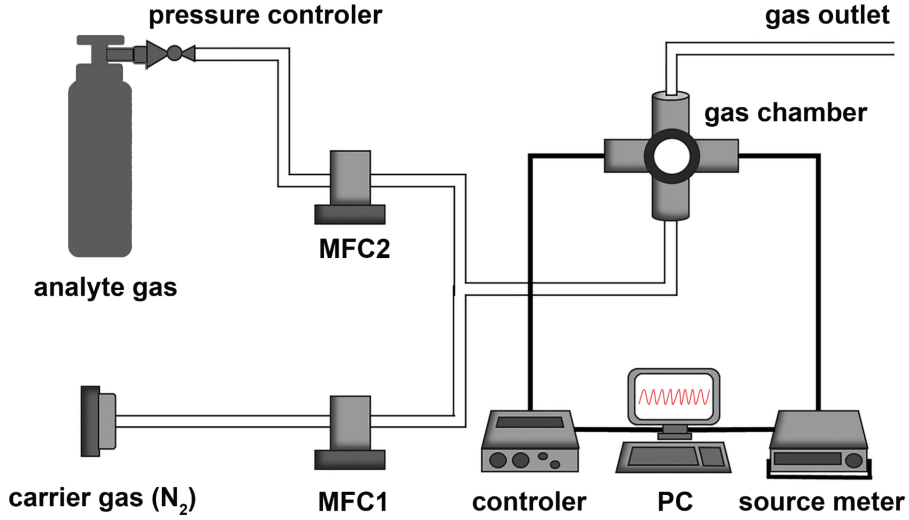
Figure 2.1 Gas sensing measurement set-up [112].

[115]. MDS solves Newton's equations of motion for a system of N interacting atoms [116, 117]:

$$m_i \frac{\partial^2 r_i}{\partial t} = F_i, i = 1, 2, 3, \ldots \ldots N \tag{2.2}$$

The forces are the negative derivatives of the potential function $V(r_1, r_2, r_3, \ldots r_N)$:

$$F_i = -\frac{\partial V}{\partial r_i}, i = 1, 2, 3, \ldots \ldots N \tag{2.3}$$

Where m_i is the mass of atom i, r_i is the position vector of atom i , F_i is the force of atom i, and V is the potential energy of the system, which could be described by forcefield, such as OPLS-AA force field [118], GROMOS 54a7 force field [119], etc.

The equations are solved simultaneously in small time step, such as 2 fs. The system runs for some time with the temperature and pressure remaining at the required values [120, 121], and the coordinate's information are written to an output file at regular intervals. The coordinates are function of time representing the trajectory of the system. After initial changes, the system usually reaches an equilibrium state after some time. By analyzing over an equilibrium trajectory, many macroscopic properties can be extracted from the output file [122].

In this thesis, there were some specific simulation tasks distributed in each chapter. In chapter 3, simulation work was performed to investigate the stabilization mechanism of exfoliated graphene in aqueous solution. In chapter 4, simulation work was done to demonstrate the interaction between NH_3 molecules and the functionalized graphene in order to elucidate the sensing mechanism of the NH_3 gas sensor. In chapter 5, the interaction between odor molecules and the functionalized graphene was modeled to demonstrate the competing adsorption mechanism between different odor molecules and functionalized graphene. In chapter 6, the interaction between $NH_3(PH_3)$ gas molecules and functionalized graphene was simulated to explain the analyte gases adsorption behavior on functionalized graphene surface.

2.8   Machine learning technique

In this work, machine learning techniques were employed to preprocess the sensing signal data as well as to perform odor/gas classification tasks to enhance the selectivity of gas sensors. Prior to conduct odor/gas classification with machine learning tools, preprocessing of the original data was carried out in order to extract specific features for each analyte gas as below procedures:

- Firstly, the time-dependent current information, consisting of 24 repetitions, was transformed into time-dependent resistance according to Ohm's Law.

- Then, the whole sensing profile was split up to 24 individual measurement profiles. Each profile was composed of the analyte gas exposure profile and analyte gas flushing profile.

- Thirdly, the fraction change of sensor resistance was derived and the sensing response profile was obtained.

- Afterwards, data normalization was carried out using L2 norm algorithm.

- Finally, multiple features were extracted from each response profile and represented for each analyte gas.

Table 2.4 Confusion matrix table.

		Actual Values	
		Positive	Negative
Predicted Values	Positive	True Positive (TP)	False Positive (FP)
	Negative	False Negative (FN)	True Negative (TN)

Following that, the machine learning techniques were applied to classify these data, such as supervised machine learning and unsupervised machine learning.The main distinction between them is the use of labeled dataset. Supervised learning uses labeled input and output data while unsupervised learning not. PCA and LDA are two most popular algorithms of unsupervised learning and supervised learning, respectively. Both algorithms aim to look for linear combinations of the features which best explain the data. PCA is to find the directions that maximize the variance in a dataset. LDA is to find the directions that maximize the separability between groups. In this thesis work, on one hand, clustering analysis was performed for the feature data of all the odors/gases by unsupervised machine learning. On the other hand, part of the feature data (e.g., 75% data) was employed to train the classifier algorithm and the rest (e.g., 25% data) was used to verify the identification performance of gas sensor towards a variety of gases using supervised machine learning techniques.

In order to evaluate the clustering performance or classification performance of the sensors towards different gases coupled with machine learning techniques in this work, several performance indicators were considered, such as, accuracy, precision, sensitivity, specificity, F1-score, purity, etc. These performance metrics were calculated based on the confusion matrix, as shown in Table. 2.4. In our work, the above machine learning analyses were conducted by a self-developed script on Python platform. Here are some definitions of the performance indicators for machine learning techniques evaluation [123, 124].

- Accuracy denotes the ratio of the number of correct predictions to the total number of input samples achieved by classifier algorithms.

$$Accuracy = \frac{TP + TN}{TP + FP + TN + FN} \tag{2.4}$$

- Sensitivity denotes the ratio of the number of correct positive results to the number of all relevant samples that should have been identified as positive.

$$Sensitivity = \frac{TP}{TP + FN} \tag{2.5}$$

- Specificity denotes the ratio of negatives that are correctly identified.

$$Specificity = \frac{TN}{TN + FP} \tag{2.6}$$

- Precision denotes the ratio of the number of correct positive results to the number of all predicted positive results.

$$Precision = \frac{TP}{TP + FP} \tag{2.7}$$

- F1-score indicates the harmonic mean of the sensitivity and the precision.

$$F1 - score = 2 \times \frac{TP}{2TP + FP + FN} \tag{2.8}$$

Chapter 3

Stabilization mechanism of aqueous graphene dispersions

In this chapter, the stabilization mechanism of amphiphilic dispersants functionalized graphene in aqueous solution are investigated *via* classical molecular dynamic simulation. Particularly, flavin mononucleotide sodium (FMNS), will be demonstrated as an example of amphiphilic dispersants. This simulation work provides a basis for the mechanism understanding of functionalized graphene by FMNS-like dispersants strategy and paves a path to design highly efficient and biocompatible dispersants for liquid phase exfoliation of defect-free, few layers graphene. The content of this chapter is largely based on my published article [125].

3.1   Motivation

Graphene shows great promise for biomedical and sensing applications, especially for drug delivery, bio-sensing and tissue engineering [126]. However, one of the big challenges remains producing high-quality pristine graphene. So far, numerous bottom-up and top-down approaches have been developed, such as micromechanical cleavage [90], chemical vapor deposition [127], epitaxial growth on SiC substrates [128], electrochemical approaches [129], and the chemical reduction of graphene oxide [130]. Among those strategies, the liquid-phase exfoliation of graphene from graphite, assisted by dispersants, has gained prominence recently [131]. This method could provide stabilized graphene in aqueous solution with high yield and good quality, which may advance the bio-medical and sensing applications of graphene
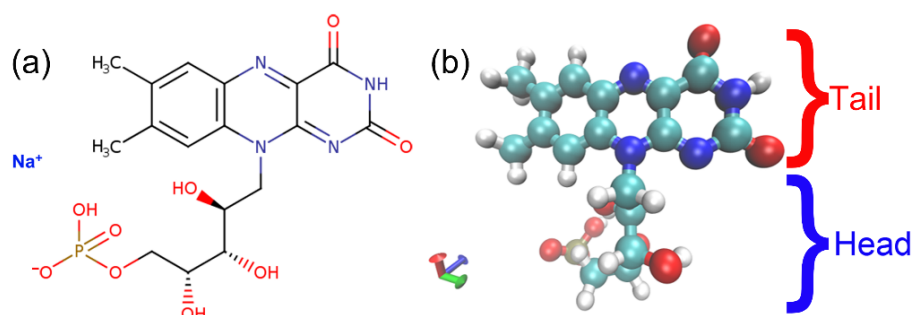
Figure 3.1 Schematic of FMNS molecules. (a) Chemical structure of FMNS. (b) Ball-and-stick model representation of FMNS. The isoalloxazine ring group is defined as the FMNS tail, while both the ribitol group and phosphate group are defined as the FMNS head. Color code: nitrogen (blue), oxygen (red), carbon (cyan), hydrogen (white) and phosphorous (tan).

[132, 133]. In this context, various dispersants have been investigated. Nevertheless, most of dispersants are not biodegradable or biocompatible [134, 135].

Very recently, S. Villar-Rodil et al. reported an innocuous and readily available derivative of vitamin B$_2$, flavin mononucleotide sodium (FMNS, C$_{17}$H$_{20}$N$_4$O$_9$PNa), schemed in Fig. 3.1, as a highly efficient biocompatible dispersant for the exfoliation and production of stable aqueous dispersions of defect-free, few-layer graphene flakes [136]. The attained graphene concentration in aqueous solution was up to 50 mg/mL using a relatively low amount of FMNS compared with abovementioned dispersants, and the processed graphene films presented excellent electrical conductivity [136]. This benign and readily available biocompatible dispersant outperformed the other biomolecules in the preparation of stabilized graphene in aqueous solution, and showed great potential for bio-medical and sensing applications [137, 138]. However, the stabilization mechanism of the FMNS dispersant for the functionalized graphene has not yet been fully addressed. In this work, classical molecular dynamics simulations will be performed to gain deep information on the influence of the dispersants on the stabilization of functionalized graphene in aqueous dispersion.

3.2   Modelling

The simulation work was divided into two parts: the simulation of FMNS morphology on monolayer graphene flakes, and the calculation of the PMF of pairs of graphene flakes coated with FMNS. All calculations were performed on platform GROMACS 5.1.2 [115]. Water molecules and FMNS molecules were modelled adopting the SPC/E model [120], and the OPLS-AA force field [118], respectively. The molecular topology of FMNS was obtained from the LigParGen server by submitting the PDB file of the FMNS (Na$^+$ excluded) [139]. Force field calculations were performed using $1.14 * CM1A$ method for charged molecules [140]. Bond lengths in the FMNS were constrained applying the parallel version of the LINCS algorithm while the bond lengths and angles in water molecule were constrained applying the SETTLE algorithm [141]. A monolayer graphene flake (size $4\ nm \times 4\ nm$, containing 680 carbon atoms) was selected as a representative monolayer graphene system. The position and orientation of the flakes were constrained during the simulation, wherein all carbon atoms were treated as uncharged Lennard-Jones (LJ) spheres using LJ parameters from the literature [142]. Van der Waals attraction and hard-core steric repulsion were treated with a cut-off distance of $1.0\ nm$ [143]. Long-range electrostatic interactions were treated utilizing the particle mesh Ewald (PME) approach [144]. The simulation was conducted under the NPT ensemble (the number of atoms, pressure of 1 bar, temperature of 300 K, are constant) to mimic the experimental conditions. The velocity-rescaled Berendsen thermostat was applied to maintain a constant temperature [121] and the Berendsen barostat was applied to maintain a constant pressure in the system [120], respectively. Periodic boundary conditions were applied in all three directions. The time step during the whole simulation was 2 fs and the trajectory was saved every 2 000 steps.

For the FMNS morphology on the single layer graphene flake, three cases with different amount of the FMNS molecules were studied, wherein the graphene flake size was the same. The simulation box size of the cases containing 8 FMNS and 18 FMNS was $9\ nm \times 9\ nm \times 9\ nm$ while the box size of the case containing 36 FMNS was $12\ nm \times 12\ nm \times 12\ nm$. The FMNS molecules were aligned parallel to the graphene flake in each box to obtain the initial configuration for each case [145]. For the calculation of the PMF of pairs of graphene flakes coated by FMNS, the final configurations of the morphology simulations which had the largest FMNS

Table 3.1 General details of simulations in this work. N_G: the number of graphene flakes. N_{FMNS}: the number of FMNS molecules. N_{SOL}: the number of water molecules. N_{all}: the total number of atoms. V: simulation box size. t: simulation time. C_G: the concentration of graphene. C_{FMNS}: the concentration of FMNS. Case A: high surface coverage. Case B: low surface coverage. Note: the graphene flake size in all simulations is $4\,nm \times 4\,nm$, containing 680 carbon atoms.

	Morphology simulation			PMF simulation	
Case	8 FMNS	18 FMNS	36 FMNS	A	B
N_G	1	1	1	2	2
N_{FMNS}	8	18	36	22	12
N_{SOL}	23486	23284	53964	54978	54988
N_{all}	71554	71468	164444	167438	166948
$V(nm^3)$	9×9×9	9×9×9	12×12×12	12×12×12	12×12×12
$t(ns)$	100	100	100	5	5
C_G/C_{FMNS}	2.13:1	0.95:1	0.47:1	/	/

surface coverage were employed as the starting configuration. A larger simulation box of size $12\,nm \times 12\,nm \times 12\,nm$ was created, and the same configuration of the graphene flake with adsorbed molecules at the distance of $3\,nm$ away from the original one was replicated. Subsequently, the water molecules and sodium counter ions were introduced into this box. The details on the model configural information refer to Table. 3.1.

In order to obtain a series of configurations with different distances d between the centers of mass (COM) of the graphene flakes, steered MD was used [146]. In detail, one graphene flake was fixed, in $x/y/z$ direction and the other graphene flake, only in y/z direction. A harmonic potential with a force constant k = 600 000 $kJ/(mol \cdot nm^2)$ was applied to the COM of the second flake, which pulled it close to the first flake by setting a velocity of 0.005 nm/ps. The pulling time was based on the distance d between the graphene flakes at the beginning. Due to the very slow pulling rate, the FMNS molecules adsorbed on the surface of the graphene flakes
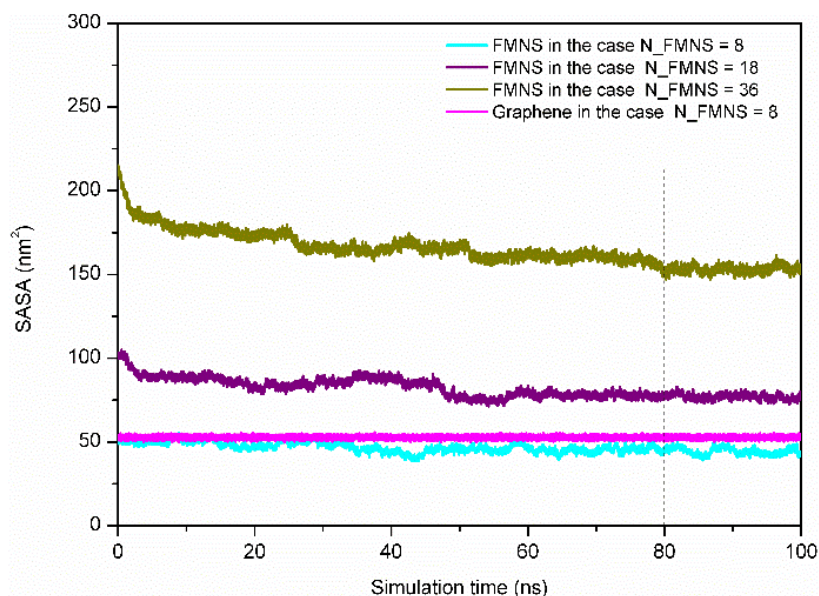
Figure 3.2 SASA of FMNS as a function of simulation time, both in three different cases and the representative result for graphene.

could freely reorganize on the graphene flake surface [147]. In this case, a series of configurations with different COM distances in an "evolutionary manner" was obtained [145]. The constraint pulling was employed to calculate the interaction force between graphene flakes along x axis. The PMF was then calculated by numerically integrating the constraint pulling force using the trapezoidal rule at different distances, as described in a previous publication [148].

3.3 FMNS morphology on graphene surface

To investigate the morphology of FMNS on the surface of the graphene flakes, three different cases are studied with 8, 18 and 36 FMNS molecules, respectively. The solvent accessible surface areas (SASAs) of the flavin mononucleotide ions and graphene as a function of time was calculated to verify that all the simulations have reached equilibrium [149]. As the SASA results shown in Fig. 3.2, it can be seen that the systems have reached equilibrium after about 80 ns simulation time. Correspondingly, the result analysis is extracted from the last 20 ns of each trajectory.
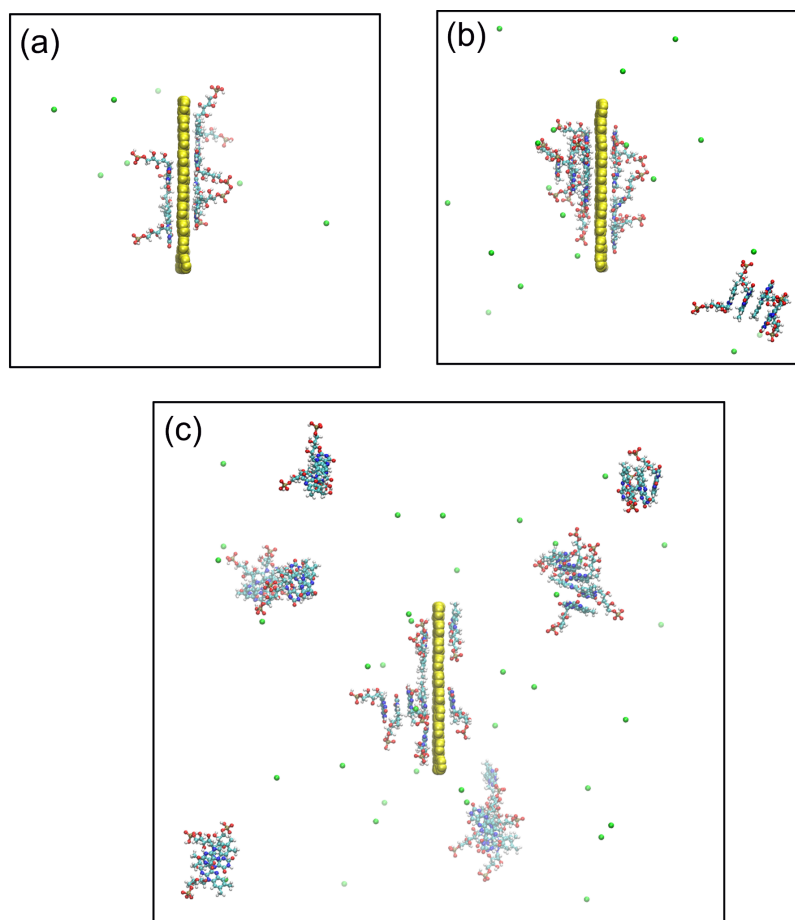
Figure 3.3 Post-equilibrated representative morphology snapshots of FMNS molecules and the graphene flake (yellow) in three different cases: Side views of cases containing (a) 8, (b) 18 and (c) 36 FMNS molecules. Sodium counterions are shown in green and water molecules are not shown for clarity.

The representative morphology results are shown in Fig. 3.3. For the case with 8 FMNS molecules, as shown in Fig. 3.3 (a), it is found that all FMNS molecules aggregate on the surface of the graphene flake. The tail groups of FMNS are adsorbed to the graphene surface parallelly while the head groups extend toward the water. This feature is similar to the behavior of FMNS on a single wall carbon nanotube (SWCNT) surface [147]. For the case with 18 FMNS molecules, as shown in Fig. 3.3 (b), most of the FMNS molecules aggregate on the graphene surface. The orientation behavior of the tail and the head groups are the same as in the case with 8 FMNS. However, the formation of several clusters of FMNS molecules was observed. For the case with 36 FMNS molecules, as shown in Fig. 3.3 (c), only a small portion of the FMNS molecules is observed to stick to the surface of the graphene flake parallelly while
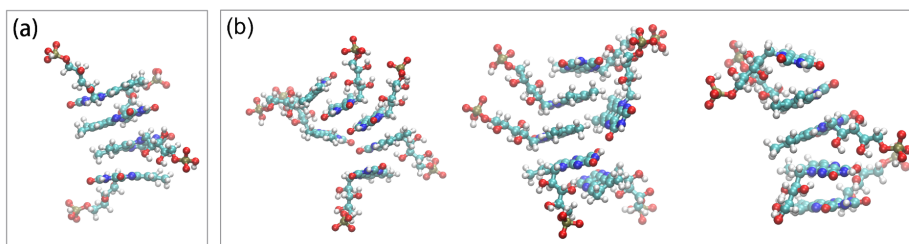
Figure 3.4 FMNS cluster formation in different cases: (a) representative FMNS cluster in case of 18 FMNS, (b) representative FMNS clusters in case of 36 FMNS in the simulation box.

most of the FMNS molecules favor to stay in the solvent in the form of clusters. This finding provides further evidence that FMNS molecules possess a tendency to form dimer structures at high concentrations, which agrees well with the experimental results [150].

As shown in Fig. 3.4, the unabsorbed FMNS molecules tend to form sandwich-like clusters which is favored by $\pi - \pi$ interactions. This behavior is different from other dispersants which tend to form a mono-dispersant layer at low concentrations and hemicylindrical micelles or micelles at high concentrations [151]. Meanwhile, it is noted that the negatively charged FMNS head groups favor to keep away from each other due to the electrostatic repulsion.

In order to characterize the space distribution of the head and tail groups around the flakes, their radial distribution functions relative to the COM of the graphene flake are shown in Fig. 3.5. From the peak positions shown in Fig. 3.5 (a)-(c), it can be seen that the tail groups prefer to approach to the graphene surface while the head groups prefer to keep away from graphene, corroborating the morphology observation in Fig. 3.3. Among these cases, the tail group in case of 8 FMNS molecules shows the strongest peak at around 0.41 nm while the tail group in case of 36 FMNS molecules shows the weakest peak at around 0.44 nm. The first peak position for the tail group has a shift away from graphene with increasing amount of FMNS molecules. Besides, the second peaks for the tail group appear due to the FMNS cluster formation except in the case of 8 FMNS. In case of 18 FMNS, the first peak and the second peak for the tail group are found at 0.42 nm and 0.72 nm, respectively. In case of 36 FMNS, the second peak is found at around 5.80 nm. The head groups in these cases show similar behavior as the tail groups. The sodium counterions were mostly close to the head groups because of the electrostatic attraction.
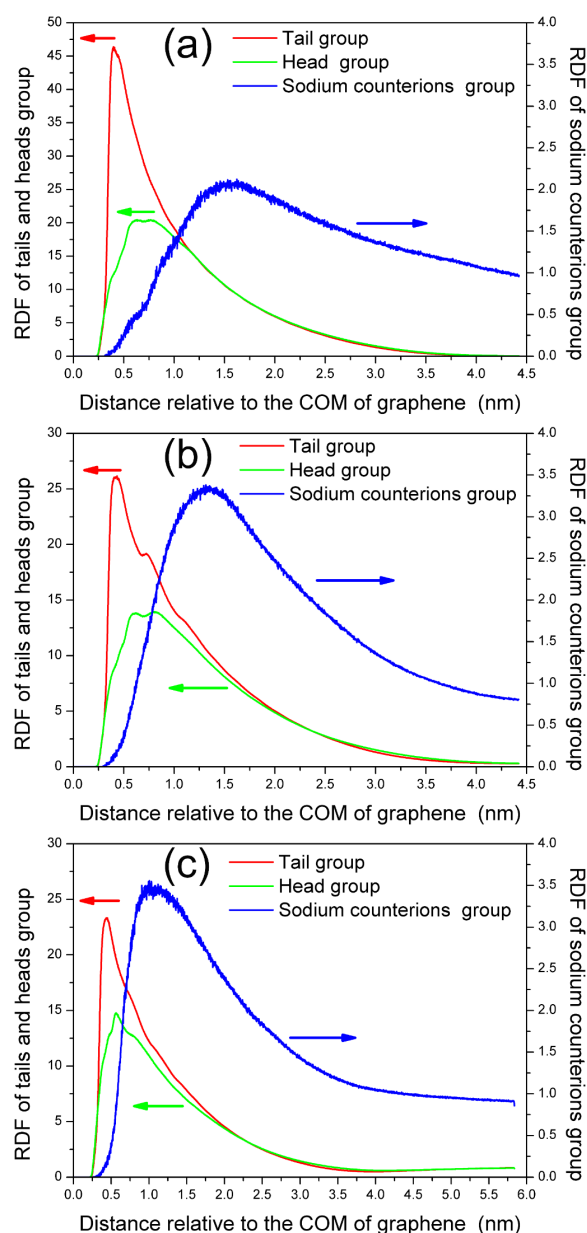
Figure 3.5 RDF results of FMNS tail and head groups as function of the relative distance to the COM of the graphene flake in different cases (a) 8 FMNS molecules (b) 18 FMNS molecules and (c) 36 FMNS molecules.

Further, the density distributions of different groups in the three cases are investigated to characterize the different distributions along x axis, as shown in Fig. 3.6 (a)-(c). For the case of 8 FMNS molecules, shown in Fig. 3.6 (a), there are two strong peaks in the density distribution profile of both the tail groups and the head groups, which are very close to the COM position of the graphene flake (x=0). The right peaks
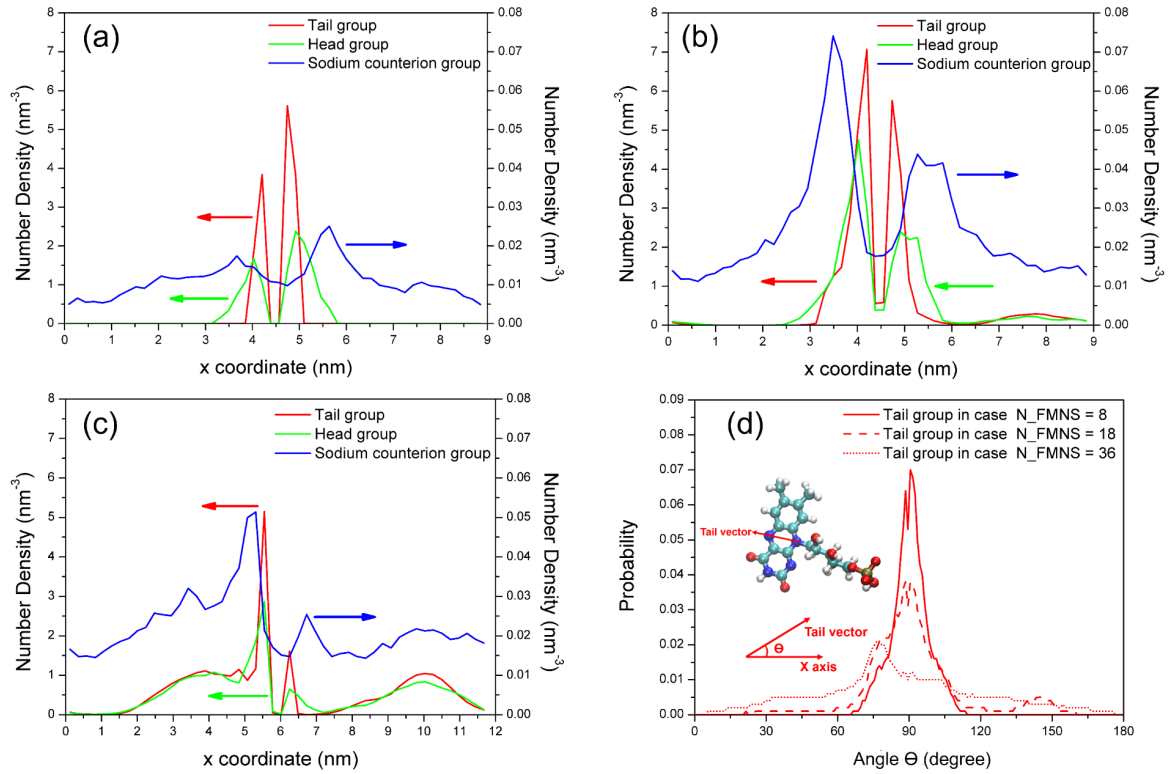
Figure 3.6 Density distribution of the different groups along x coordinate in different cases: (a) 8 FMNS molecules, (b) 18 FMNS molecules and (c) 36 FMNS molecules. The Graphene flake is fixed at position x=4.5 nm in case of 8 and 18 FMNS molecules, and at x=6.0 nm in case of 36 FMNS molecules. (d) Tail group orientation distribution in the three different cases, the inset shows that the orientation angle θ.

of both groups are higher than the left peaks, which is consistent with the morphology observation in Fig. 3.3 (a): three molecules on the left side and five molecules on the right side. Furthermore, the peak position of the tail groups is closer than the peak position of the head groups to the graphene flake, which can be explained by the hydrophilic behavior of the phosphate group in the head of FMNS which prefer to stay in the solvent while the hydrophobic nature of the isoalloxazine group in the tail of FMNS which tends to stick to the graphene surface. For the density distribution profile of the sodium counterions, there are two main peaks observed close to the positions of the head groups due to the electrostatic interaction.

In the case of 18 FMNS, shown in Fig. 3.6 (b), additionally to the two main peaks close to the COM of the graphene flake (x =0 nm), one more peak is found near x = 3.2 nm, which is the result of the small FMNS cluster formation. This corroborates

the morphology shown in Fig. 3.3 (b). From Fig. 3.6 (c), in addition to the peaks located near the COM of the graphene flake (x = 0) in the profiles of both groups, several peaks can be identified away from the COM of the graphene flake (x=-2 nm and x=4 nm). These originate from the FMNS-cluster formation as seen in Fig. 3.3 (c). To quantify the precise orientation of the tail groups relative to the graphene flake, the angle θ was used as illustrated in Fig. 3.6 (d). The tail vector is defined as connecting two nitrogen atoms in the tail group and the angle θ is the angle between the tail vector and the positive direction of the x axis, as schemed in the inset in Fig. 3.6 (d). For the cases of 8 FMNS and 18 FMNS molecules, the orientation angle θ is mainly concentrated around 90°, which means that the tail groups of the FMNS molecules aggregated on the graphene flake favor to stay parallel to the surface. However, for the case of 36 FMNS molecules, most of them form small clusters and are distributed uniformly in the box. Only for the molecules aggregated on the surface of graphene flake, the orientation angle is $\theta = 90^o$.

3.4   The PMF of functionalized graphene flakes

The potential of mean force (PMF) is used to characterize the interaction between two graphene flakes in the presence of an aqueous medium and FMNS molecules. A positive PMF implies an effective repulsion while a negative PMF indicates an effective attraction of the flakes [147]. The PMF results for the cases considered in this study are presented in Fig. 3.7. The three profiles in Fig. 3.7 are obtained for high FMNS surface coverage, low surface coverage, and no surface coverage, respectively. Here, the final configuration of the case of 18 FMNS is used as the starting configuration for high surface coverage, for which there are 11 FMNS molecules adsorbed on the surface of each flake. All the FMNS molecules whose tail groups are located within 7 nm from the graphene flake are defined as adsorbed molecules. For low surface coverage the number of adsorbed FMNS molecules is decreased to 6 molecules on each flake as the starting configuration. This corresponds to surface coverages of 0.34 molecules/nm^2 and 0.19 molecules/nm^2, respectively. The PMF of the pairs of bare graphene flakes without FMNS was done for comparison. The PMF has been set to zero at the large COM distance between pairs of graphene flakes (d = 3.0 nm).
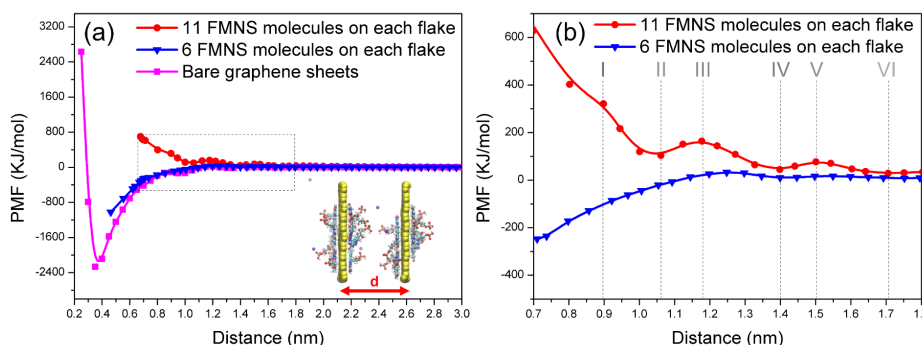
Figure 3.7 The PMF results of graphene flakes with/without functionalization. (a) The profiles of PMFs of pairs of graphene flakes coated by or without FMNS molecules. Inset shows the distance d between a pair of parallel graphene flakes. (b) The zoom of the dashed box in the left panel, seven critical positions are labelled on the profile.

As one can see from Fig. 3.7 (a), the PMF of bare graphene flakes displays a pronounced minimum at the distance of d = 0.35 nm which corresponds to the typical interlayer distance in graphite. From 0.35 nm to 3.0 nm, the PMF is negative, which indicates an attractive interaction between two bare graphene flakes in solution. The well depth of the PMF at the minimum is -2268 kJ/mol. Considering the area of graphene flake, the PMF per unit area is -142 $kJ/(mol \cdot nm^2)$, which is in good agreement with the previously reported PMF per unit area of -153 $kJ/(mol \cdot nm^2)$ [152].

For the case of low surface coverage, the PMF shows attractive behavior from d = 0.45 nm to d = 1.10 nm, and it shows repulsive behavior from d = 1.10 nm to d = 3.0 nm. It reaches its highest energy barrier of +33 kJ/mol at d = 1.25 nm. For high surface coverage, one sees that the adsorbed FMNS molecules cause relatively strong repulsion already at d = 0.7 nm, which can hinder the aggregation of graphene flakes efficiently. The highest repulsive energy of +705 kJ/mol appears at d =0.68 nm (the shortest distance with reliably calculated PMF) [153]. The first local maximum energy barrier appears at d=1.18 nm and the PMF energy barrier reaches up to 164 kJ/mol. The PMF energy barrier per area is 10.25 $kJ/(mol \cdot nm^2)$.

To evaluate the influence of FMNS on the dispersion and stabilization of the exfoliated graphene flakes, the calculated surface coverage of graphene flakes by different conventional dispersants at roughly the same PMF energy barrier is compared, as shown in Table. 3.2. To achieve the PMF energy barrier of around 10 $kJ/(mol \cdot nm^2)$, the surface coverage of graphene flake by FMNS is 0.34 $molecules/nm^2$ as

Table 3.2 Comparison results of different surfactants for the stabilization of aqueous graphene dispersions from both simulation and experimental works.

N: relative amount of surfactant, calculated as follows, number of surfactants/numbers of carbon atoms in graphene flake. S: surface coverage of graphene by surfactant, calculated as follows, number of surfactants adsorbed on each graphene flake/both sides area of each graphene flake, unit: $molecules/nm^2$. E: PMF barrier is the barrier of the first local maximum energy barrier on the PMF profile, unit: $kJ/(mol \cdot nm^2)$. C: Obtained graphene concentration reported experimentally in other's work ($\mu g/mL$).

Surfactants	Simulation results			Experimental results
	N	S	E	C
SDS	0.048	1.00	15.00 [154]	12.00 [155]
SDBS	0.029	0.58	11.40 [156]	20.00 [155]
SC	0.026	0.49	10.00 [153]	27.00 [155]
FMNS	0.026	0.34	10.25	200.00 [157]
	this work	this work	this work	

shown above, while the surface coverage of graphene flake by SDBS is around 0.58 $molecules/nm^2$ [156], and the surface coverage of graphene flake by SC is around 0.49 $molecules/nm^2$ [153], respectively. Those theoretical results provide evidence that FMNS is performing better than the other commonly used dispersants with respect to the dispersion and stabilization of exfoliated graphene flakes. This result is consistent with the reported experimental work which showed that FMNS is an extremely efficient dispersant for the preparation of dispersions of few-layer aqueous graphene flakes [136].

Fig. 3.7 (b) is a zoom into the dashed frame in Fig. 3.7 (a) with seven critical points marked on the profile. On the PMF profile of graphene flakes with high surface coverage (red line), positions II, IV, VI denote local energy wells while positions III and V correspond to local energy barriers. On the PMF profile of graphene flakes with low surface coverage, positions III and V indicate energy barrier positions while position VI is a local energy well. The density distribution of the FMNS molecules in the case of high surface coverage corresponding to the 6 critical positions are plotted in

Figure 3.8 Density distribution results of FMNS in high surface coverage case. (Left panel) Density distribution of FMNS molecules along x coordinate in case of 11 FMNS molecules on each graphene flake. The red lines marked the position of the graphene flakes. The inset images show corresponding morphologies. The color code is the same as in Fig. 3.1, water molecules are not shown for clarity. (Right panel) The 2D density map of the FMNS molecules existed in the confined volume between a pair of parallel graphene flakes with 11 FMNS molecules on each flake for the critical positions I to VI. The maximum value of density for each image can be found in Table. 3.3

Fig. 3.8, and the inset images are the representative snapshots. With decreasing distance d between flakes from position VI to position I, the density distribution peak of the FMNS molecules between the two graphene flakes decrease from two broad peaks to one sharp peak. For the distance with a local high energy barrier, including positions III and V, it is found that the head groups of the FMNS between the two flakes try to aggregate tightly and form one strong density peak, just like a fastened zipper with two head group chains. However, for the distances of local energy wells, including positions II, IV and VI, it is observed that the head groups of the FMNS between the two flakes kept well and so two separate peaks show on the density profile, just like an unfastened zipper with two head groups' chains. This agrees well with previously reported results [154]. This can also be seen on the corresponding morphology image. In order to further verify this behavior, the density map for the FMNS molecules between the two graphene flakes to see the overlap of molecules
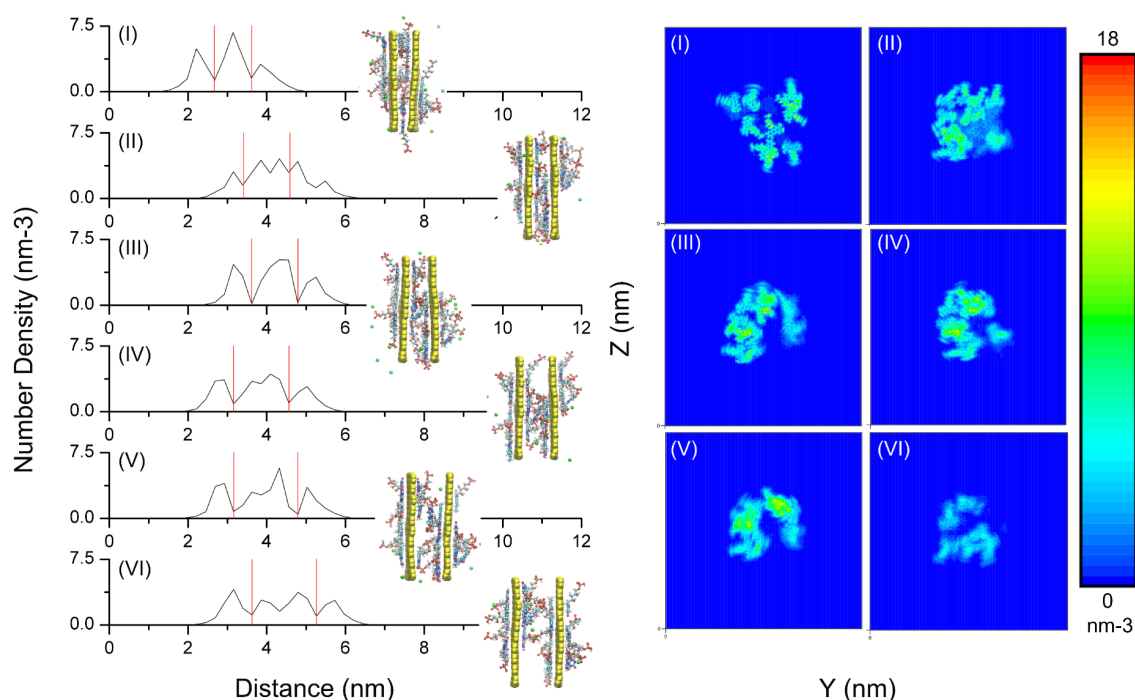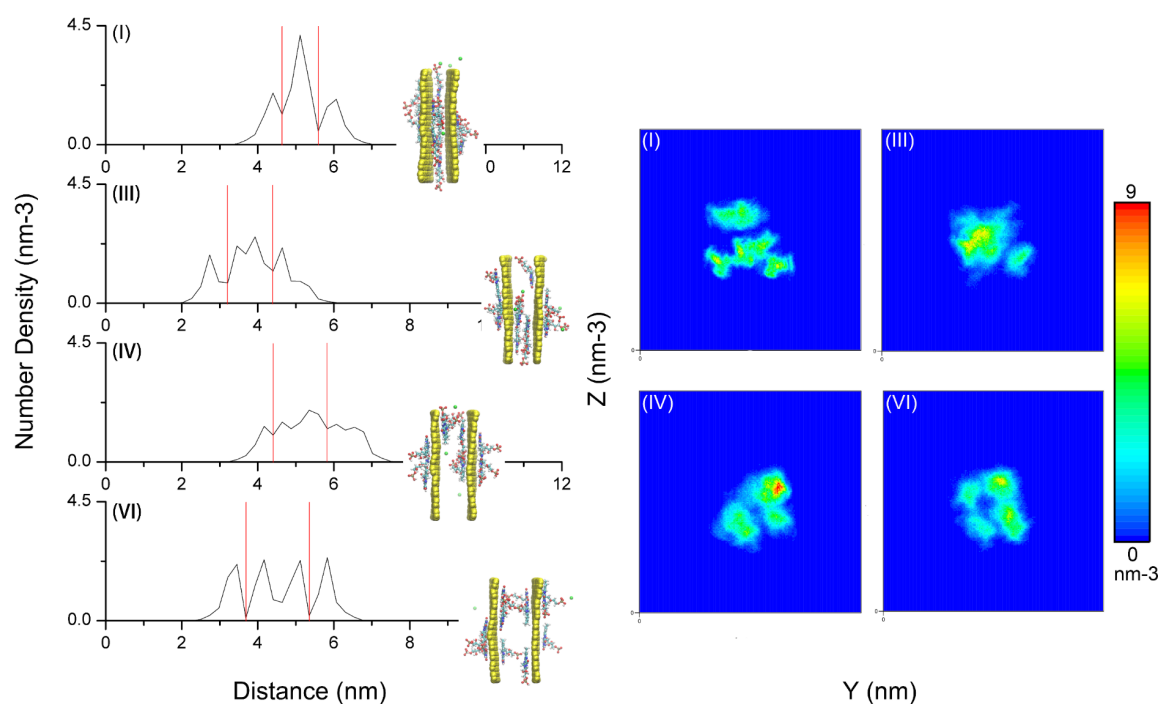
Figure 3.9 Density distribution results of FMNS in low surface coverage case. (Left panel) Density distribution of FMNS molecules along x coordinate in case of 6 FMNS molecules on each graphene flake. (Right panel) The density map of the FMNS molecules located in the confined volume between a pair of parallel graphene flakes with 6 FMNS molecules on each flake for the critical positions I, III, IV and VI. The maximum value of density for each image can be found in Table. 3.3.

Table 3.3 The maximum density value of FMNS molecules at both high surface coverage case and low surface coverage case at different critical positions. Case A: high surface coverage, 11 FMNS/flake. Case B: low surface coverage, 6 FMNS/flake.

	Position		
Case	I	II	III
A	15.7	12.9	17.7
B	7.07	/	7.76

is plotted, as shown in Fig. 3.8. It is found that the maximum density values for the positions of the energy barriers are higher than those at the positions with the next energy wells. The maximum values of the density are given in Table. 3.3 [147].
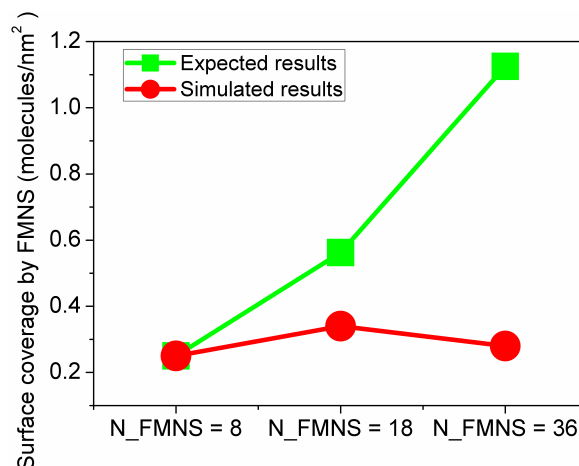
Figure 3.10 Surface coverage of graphene flakes by FMNS molecules in three different cases with N=8, 18 and 36 molecules in the simulation box.

At the same time, the density distribution of the FMNS in the cases of low surface coverage as well as the density map of the FMNS is plotted, as shown in Fig. 3.9. Although position I shows a low negative PMF, there is one density peak found in Fig. 3.9, because FMNS molecules between two graphene flakes are much more mobile and some can even can escape the volume between two graphene flakes.

3.5   Surface coverage of graphene by FMNS molecules

From the morphology results shown in Fig. 3.4, it is already concluded that upon increasing the amount of FMNS molecules, some of them aggregate to form clusters. Thus, not all molecules in the solution will be adsorbed on the flake. The final surface coverage of a single flake with FMNS molecules is shown in Fig. 3.10. Here, the surface coverage is defined as the total number of adsorbed FMNS molecule per area of the graphene flake. In the three cases considered before, the total available surface area for FMNS adsorption is the area of both sides of the graphene flake, i.e., $32\,nm^2$. Adsorbed molecules on the graphene flake are supposed to keep graphene flakes away from each other in an aqueous medium *via* electrostatic repulsion and stabilize graphene dispersions. From the results shown in Fig. 3.10, it can be found that an unusual trend different from the expected results: with the number of FMNS molecules in the solution increasing, the surface coverage of graphene increases first and then decrease again, this can be attributed to the cluster formation in case

of a sufficiently high concentration of FMNS molecules, as already shown in Fig. 3.3 (c). Experimentally, D. Frackowiak and collaborators have previously reported that the FMNS molecules tend to form dimers in an aqueous media, and a large fraction of FMNS molecules participate in forming dimeric structures as the FMNS concentrations increase [150]. Our simulation results are consistent with this experimentally observed behavior.

The formation of FMNS dimers and larger clusters prohibits adsorption of FMNS molecules on the graphene flake surface [136]. Consequently, a lower surface coverage of FMNS molecules on the graphene flake is obtained. As shown in Fig. 3.7 , a higher surface coverage implies a stronger repulsion of flakes to avoid aggregation. In case of lower surface coverage, the repulsion is lower and the graphene flakes tend to aggregate more easily. This observation might explain the origin of the observed relationship between the concentration of FMNS and the stabilization of graphene dispersions in a recent experimental work [136]. Our simulation results indicate that the optimal mass ratio between FMNS and monolayer graphene is 1.06 shown in the case of N_{FMNS} = 18 and achieve the highest surface coverage of graphene flake by FMNS (0.34 $molecules/nm^2$).

3.6   Summary

In this chapter, the stabilization mechanism of functionalized graphene in dispersant aqueous dispersion are investigated using all-atom MD simulations. The morphology of FMNS on a monolayer graphene flake is presented. The radial distribution function (RDF) and the density distribution of FMNS molecules, as well as their orientations are discussed. Then, the PMF of pairs of parallel graphene flakes is calculated. Finally, based on the PMF results, the relationship between FMNS surface coverage on monolayer graphene flake and FMNS concentration is discussed. These results indicate that the optimal mass ratio between FMNS and monolayer graphene is about 1.06 leading to a surface coverage of 0.34 FMNS $molecules/nm^2$ on the graphene flakes. The simulations support the high efficiency of FMNS as a dispersant.

Chapter 4

Highly sensitive pristine graphene-based gas sensors

With the stabilization mechanism of functionalized graphene in aqueous dispersion in mind, in this chapter, non-covalently functionalized graphene by FMNS will be prepared experimentally for the potential application as gas sensing materials in a chemiresistive type NH_3 gas sensor at room temperature. Meanwhile, the roles of FMNS from graphene preparation to NH_3 exposure sensing are elucidated *via* all-atom molecular dynamics simulations. The content of this chapter is mostly based on my published article [111].

4.1   Motivation

Ammonia (NH_3) detection plays a critical role in environmental monitoring and inspection in order to secure public safety [158]. At present, sensing materials of most commercial ammonia sensors consist of either polymer materials [159], or metal oxide semiconductors [160]. The limitations of these sensors include: high cost, limited life time, high working temperature, high power consumption, low sensitivity, poor selectivity, and insufficient repeatability [161]. As an alternative, graphene, , a one-atom-thick two-dimensional carbon nanomaterial possessing excellent physical properties [162], has been extensively investigated as a material for ammonia gas sensors in recent decades [163]. It was shown to yield excellent performance in terms of sensitivity, reversibility and work temperature, as presented in the chapter 1.
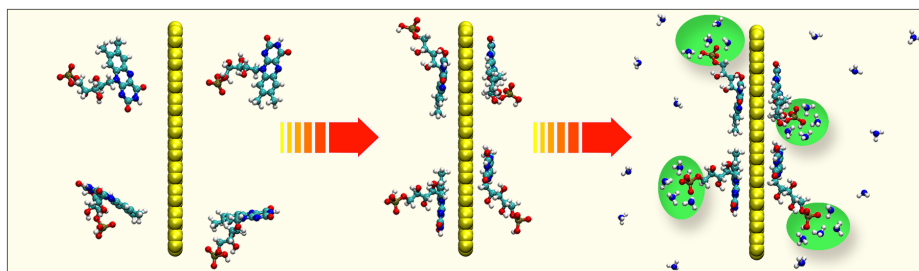
Figure 4.1 Role of FMNS for graphene-based ammonia gas sensors: stabilizer for graphene dispersions and carrier dopants for graphene flakes as well as specific active anchor sites for NH$_3$ molecules. Color code: carbon (cyan), oxygen (red), nitrogen (blue), hydrogen (white), phosphorous (tan), graphene flake (yellow).

In this work, graphene is efficiently exfoliated from graphite utilizing FMNS and the sensing characteristics of Graphene/FMNS flakes (G-FMNS) towards ammonia gas are systematically investigated. The FMNS molecules function in multiple roles, as a dispersant and a stabilizer for the graphene dispersion, as carrier dopant for graphene flakes and as active anchor sites for ammonia molecules with a specific interaction, which is illustrated in Fig. 4.1.

4.2   Graphene dispersion preparation and characterizations

The fabrication workflow of graphene-based gas sensors is shown in Fig. 4.2, in which the graphene exfoliation, sensor fabrication has been described in Chapter 2. The chemical structure of flavin mononucleotide sodium salt (FMNS, C$_{17}$H$_{20}$N$_4$Na-O$_9$P) is displayed in Fig. 4.3 (a). To simplify the discussion of this structure, the large isoalloxazine ring group is defined as FMNS tail, and the rest is defined as FMNS head. In order to measure thickness of Graphene-FMNS flakes following dispersion preparation, 10 μL Graphene-FMNS dispersion was drop-casted on the SiO$_2$/Si substrate. The droplet was from the supernatant of Graphene-FMNS dispersion after removal of excess FMNS molecules centrifuged at14500 rpm and centrifugation at 4000 rpm. The apparent thickness ranges from several nm to tens nm, as shown in Fig. 4.3 (b). Nevertheless, for graphene flakes exfoliated by surfactants, analyzing the actual layer number of the flake from AFM results is not forthright [136]. Similar to the reported works, the AFM-derived step height of within individual ex-
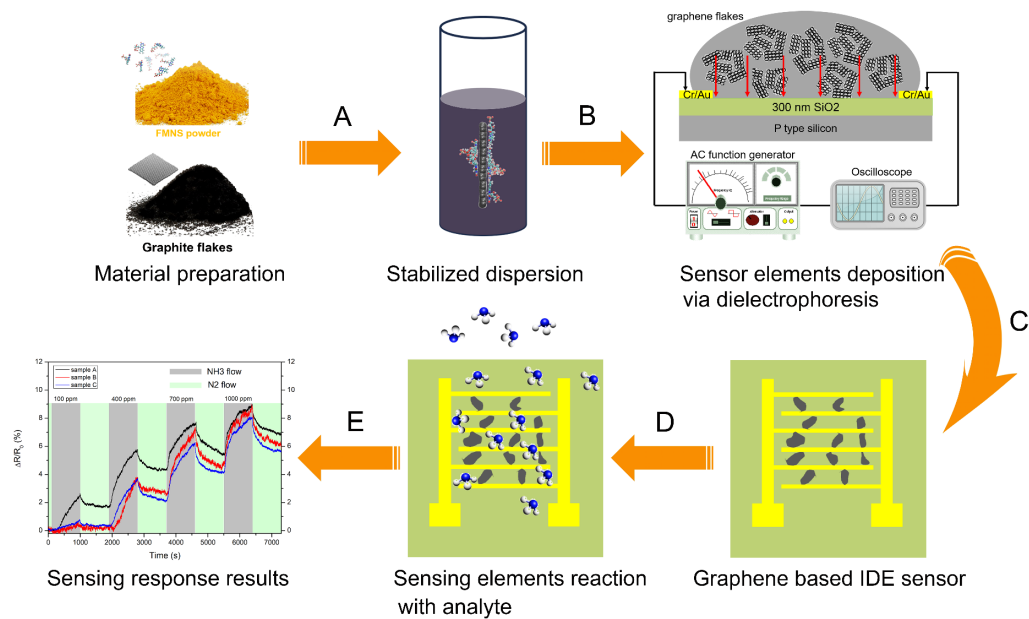
Figure 4.2 Schematic of the workflow to prepare graphene-based gas sensors. (A) Ultra-sonication in DI water and centrifugation. (B) 10 μL droplet deposition. (C) Flushing with DI water and drying with dry N$_2$ flow. (D) Exposure to NH$_3$ analyte gas. (E) Data analysis.

foliated flakes is proportional to 1.0 nm, indicating that each layer contributes with that amount to the apparent thickness. Further, FMNS molecule was about 1 nm high, so it is rational to assume that the measured thickness of the flake contains around 1 nm from the FMNS molecules adsorbed between the graphene flake and the substrate [164]. Consequently, a measured apparent flake thickness of around 2 nm suggests single-layer graphene, and each layer that stacks on the flake would increase this value by around 1 nm. Hence, the AFM results reveal that mainly multi-layer graphene flakes were obtained in the exfoliation using FMNS [165].

The lateral size of Graphene-FMNS flakes was characterized by SEM, as shown in Fig. 4.3 (c). To remove the excess FMNS molecules, the dispersion after ultra-sonication step was centrifuged at 14500 rpm twice. Then the sediment was re-dispersed with DI water and separated employing different centrifugation rate of 4000 rpm. The supernatant was drop-casted onto SiO$_2$/Si substrate for SEM characterization while the sediments containing large un-exfoliated flakes were discarded [157].It is found that the flakes range from 100 nm to 1000 nm after centrifugation at 4000 rpm. Larger flakes (up to 3000 nm) can be obtained centrifuged with a lower centrifugation speed (at 1000 rpm), as shown in Fig. 4.3 (d).
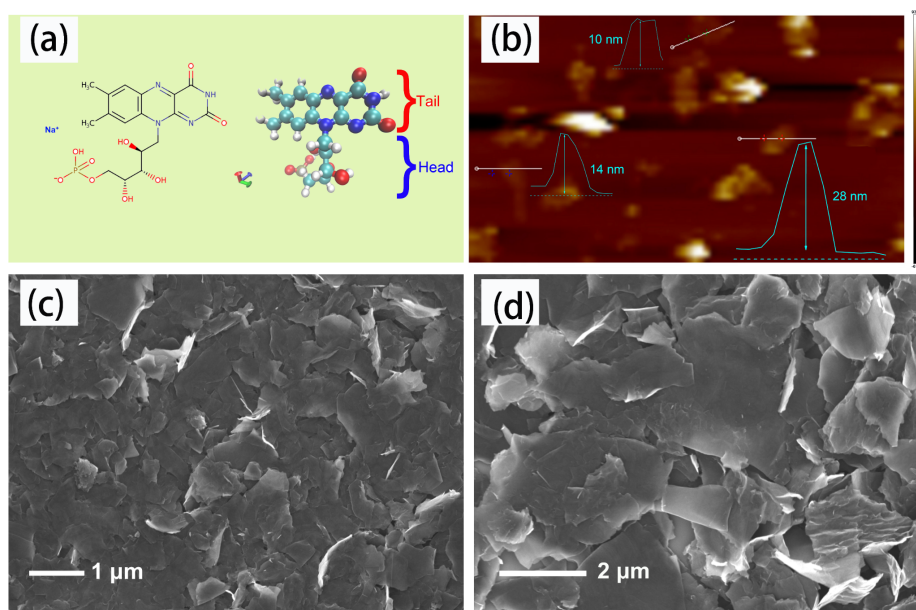
Figure 4.3 Morphology characterization for FMNS functionalized graphene flakes on silicon substrate. (a) Chemical structure of FMNS (left panel) and ball-and-stick model representation of FMNS (right panel). Color code: nitrogen (blue), oxygen (red), carbon (cyan), hydrogen (white) and phosphorous (tan). (b) AFM characterization of Graphene-FMNS flakes. (c) (d) SEM characterization of Graphene-FMNS flakes.

Fig. 4.4 (a) displays the Raman spectrum of the graphene flakes, which shows the evidence that the graphene flakes are of high structural quality. Four main signals are observed from the Raman spectra: the disorder related D band at around 1352 cm^{-1} and D' band at around 1623 cm^{-1}, G band at around 1583 cm^{-1}, 2D band at around 2703 cm^{-1}. Additionally, a few combinations of them are also observed: D + D" at around 2453 cm^{-1}, D + D' at around 2952 cm^{-1}. The G band is attributed to the sp^2-hybridized carbon bonds in the graphene lattice [166]. The existence of D band indicates the presence of edge defects in the graphene flakes induced by horn ultra-sonication exfoliation [136]. The basal planes of the graphene flakes are not damaged largely corroborated by the low ratio of the D to G peaks intensity (I_D/I_G = 0.29), which is much lower than that of chemically reduced graphene oxide (I_D/I_G > 1.0) [167, 168]. It has been recently demonstrated that the ratio of the D band to the D' band intensity ($I_D/I_{D'}$) can be employed experimentally to obtain information on the nature of defects in graphene [169]. In this case, the ratio ($I_D/I_{D'}$) is around 2, implying that the structural disorder of the graphene flakes is dominated by the edges, showing a good consistency with the former results. The featured 2D band and the ratio of the 2D band to the G band intensity (I_{2D}/I_G = 0.59) can
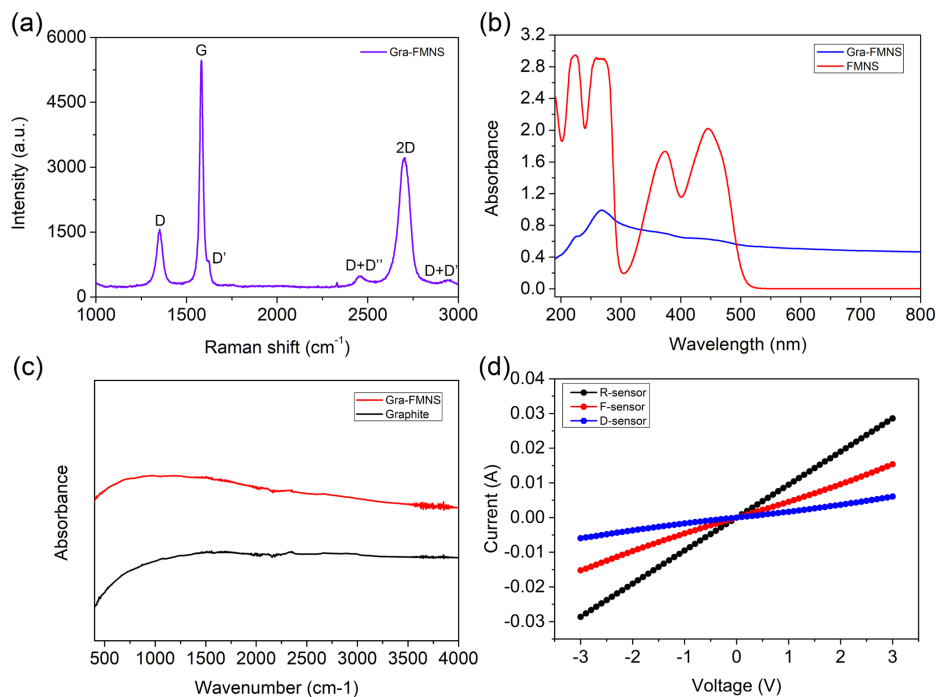
Figure 4.4 Characterization for FMNS functionalized graphene flakes. (a) Raman spectrum characterization of Graphene-FMNS flakes. (b) UV-vis absorption spectra of both Graphene-FMNS flakes and pure FMNS. (c) ATR-FTIR characterization of Graphene-FMNS flakes. (d) Electrical characterization of different graphene-based sensors.

be interpreted as a typical result for multi-layer graphene flakes [170], which is well consistent with the above AFM results.

Fig. 4.4 (b) shows the UV-vis absorption spectra of both Graphene-FMNS dispersion after purification and pure FMNS solution. On the pure FMNS curve (red), four strong absorption bands at around 225 nm, 266 nm, 373 nm, and 446 nm are observed, which are the characteristic absorption bands of FMNS in water [157]. On the Graphene-FMNS curve (blue), one strong absorption band at around 268 nm is observed, which is interpreted as the combination of two overlapping absorption bands at 266 nm and 270 nm arising from FMNS and graphene dispersion, respectively [171]. Additionally, some vanishing absorption bands on the Graphene-FMNS curve match the bands of FMNS in the red curve, suggesting the successful removal of excess FMNS molecules and coupling of rest FMNS to graphene flakes, which can be further verified by the FTIR spectra shown in Fig. 4.4 (c). Therefore, the Graphene-FMNS flakes could be colloidally stabilized in the aqueous dispersion utilizing relatively little amounts of FMNS.

Figure 4.5 Typical morphology characterization of Graphene-FMNS sensing elements for graphene-based sensors (D-sensors).
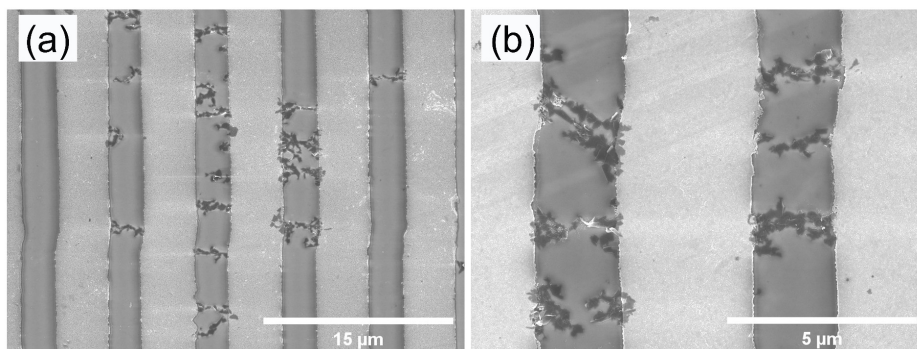
A typical attenuated total reflection Fourier transformed infrared (ATR-FTIR) spectrum of the dried powder of Graphene-FMNS flakes is displayed in Fig. 4.4 (c). Graphite powder without FMNS was used as reference. The spectra were intrinsically featureless and there were no apparent bands that came from the specific molecular groups of FMNS (especially in the range 1500-1800 cm^{-1}) [172], indicating that the excess FMNS molecules have been removed and the graphene flakes were stabilized by a very little amount of FMNS molecules. The current versus voltage (I-V) curve of the sensors in Fig. 4.4 (d) demonstrates excellent linearity from -3 V to 3 V, suggesting a good ohmic contact between the Graphene-FMNS flakes and the electrodes. A Schottky barrier at the interface between Graphene-FMNS flakes and the IDE electrodes would suppress charge transport [173], whist a low resistance ohmic contact provides a direct injection channel at the interface and minimizes the interface's influence on the intrinsic sensing properties of the Graphene-FMNS flakes. The resistances for these sensors with different treatments are 105 Ω (reference sensor, R-sensor), 253 Ω (freeze-drying treatment sensor, F-sensor), and 685 Ω (dilution treatment sensor, D-sensor).

After graphene flakes transferring onto electrode device, the morphology of deposited G-FMNS flakes were characterized by SEM. In this work, G-FMNS flakes were deposited on the gaps between interdigitated electrodes utilizing the DEP technique. Thus, they bridge adjacent electrodes and act as sensing elements of a chemiresistive type sensor. To investigate the influence of the morphology of G-FMNS flakes on the sensing characteristics, three groups of G-FMNS flakes were prepared and applied for three groups of graphene-based sensors, termed R-sensor (reference sensor, no further treatment for the G-FMNS flakes dispersion following sonication
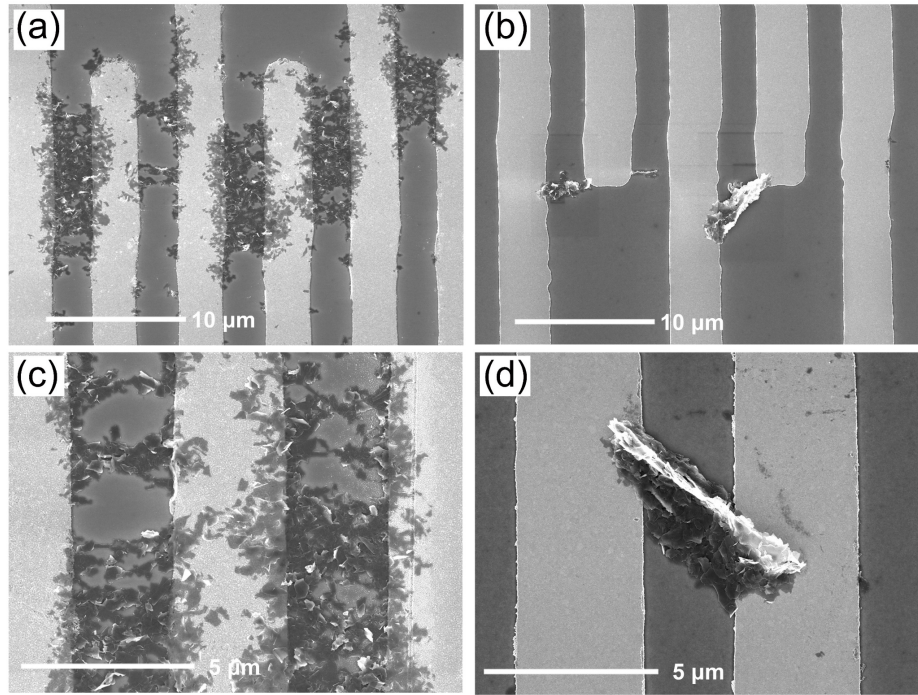
Figure 4.6 Typical morphology characterization of Graphene-FMNS sensing elements for R-sensor and F-sensor. Termed R-sensor (reference sensor, no treatment for the Graphene-FMNS flakes dispersion before DEP deposition), F-sensor (the Graphene-FMNS flakes dispersion was treated with freeze-drying before DEP deposition). (a) and (c) R-sensor. (b) and (d) F-sensor.

and centrifugation, namely reference dispersion, before DEP deposition), F-sensor (the G-FMNS flakes dispersion was treated with freeze-drying and then re-dispersed in DI water before DEP deposition), and D-sensor (the G-FMNS flakes dispersion was diluted 10 times compared with the reference dispersion before DEP deposition) in this work.

The morphology of G-FMNS flakes for the D-sensor were characterized by SEM. As shown in Fig. 4.5, G-FMNS flakes form networks to bridge the electrodes on the IDE device. These flakes stack on each other to generate compact conducting path, which ensures good ohmic contact between the G-FMNS flakes and the electrodes and exhibits very low resistance. The morphology of G-FMNS flakes for the sensor 'R-sensor' and 'F-sensor' was discussed in Fig. 4.6. For the R-sensor displayed in Fig. 4.6 (a) and (c), the Graphene-FMNS flakes form dense networks bridging the electrodes. Due to the relatively high concentration of Graphene-FMNS flake dispersion, these flakes stack on each other to generate a thick conducting layer. This ensures the low ohmic contact between the Graphene-FMNS flakes and the electrodes, and the R-

sensor exhibits very low resistance. Freeze-drying has been previously reported and employed to create porous structured material [174, 175]. As illustrated in Fig. 4.6 (b) and (d), Graphene-FMNS flakes prefer to aggregate together to form large and porous flakes under freeze-drying process. This porous structure enlarges the surface area of the sensor elements while it makes the structure looser, which in turn increase the electrical resistance of the sensing elements.

4.3   Sensing performance of sensors towards NH$_3$

Following achieving graphene dispersion, sensor device was fabricated as the standard method described in chapter 2. To investigate sensing characteristics of the developed graphene-based gas sensors, sensing measurements were conducted utilizing the homemade gas sensing setup at room temperature (25 ^oC), as depicted in Fig. 2.1 in chapter 2. The sensor response is defined as a relative change of resistance in percent. As illustrated in Figure Fig. 4.7 (a), D-sensor shows 2.8% response upon exposure to 10 ppm NH$_3$ for 30 minutes. Thereafter, the electrical resistance recovers slowly to the baseline under the N$_2$ flow flushing. In Figure Fig. 4.7 (b), under 1000 ppm NH$_3$ cycling cycles of NH$_3$ exposure and N$_2$ flushing. Sensing behavior to different concentration of NH$_3$ ranging from 100 ppm to 1000 ppm is shown in Figure Fig. 4.7 (c), the sensor exhibits 5.5% response upon exposure to 100 ppm NH$_3$ for 15 minutes and 18.5% response upon exposure to 1000 ppm NH$_3$ for 15 minutes. Sensor response with the relationship of NH$_3$ concentration (from 100 ppm to 1000 ppm) was plotted and fitted, as shown in Figure Fig. 4.7 (d). The slope of the linear regression fitting for D-sensor is 0.014 %/ppm.

In the sensing measurement, it should be noted that before performing the sensing measurements, the electrical resistance of each sensor was stabilized under continuous N$_2$ flushing for at least 2 hours, as shown in Figure Fig. 4.8 (a). Sensing results for both R-sensor and F-sensor are illustrated in Fig. 4.8 while sensing results for D-sensor are shown in Figure 3 in the main text. The R-sensor, shows 0.29% resistance increase upon exposure to 10 ppm NH$_3$ for 30 minutes, as can be seen in Fig. 4.8 (b). Thereafter, the electrical resistance recovers to the baseline under the N$_2$ flow and approaches its original baseline after 2.5 hours. To evaluate the reproducibility of the sensor performance, an exposure cycling test with 1000 ppm NH$_3$ was carried out, as shown in Fig. 4.8 (e). It is observed that after 4 cycles of
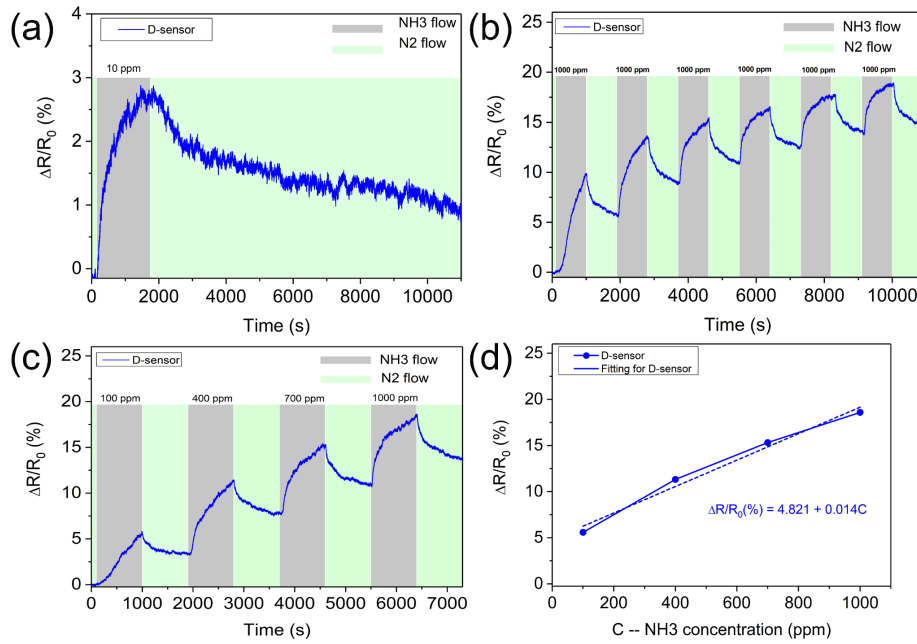
Figure 4.7 Typical sensing characteristics of graphene-based sensors (D-sensor) towards NH_3 gas. (a) Dynamic response of sensors upon exposure to ultra-low concentration of NH_3 at 10 ppm. (b) Dynamic response of sensors under 1000 ppm NH_3 cycling exposure. (c) Dynamic response of sensors upon exposure to successive different concentrations of NH_3 ranging from 100 ppm to 1000 ppm. (d) Linear fitting of D-sensor response as a function of NH_3 concentration from 100 ppm to 1000 ppm.

NH_3 exposure and N_2 flushing, the sensor exhibits stable response of around 3.9% upon 1000 ppm NH_3. When the R-sensor is exposed to different concentrations of NH_3 ranging from 100 ppm to 1000 ppm, the response reaches 0.43% at 100 ppm and finally reaches 2.33% at 1000 ppm as shown in Fig. 4.8 (h). Followed the NH_3 exposure each time, the sensor demonstrates partial recovery under N_2 flow-flushing for 15 minutes. The F-sensor, upon exposure to 10 ppm NH_3 for 30 minutes shows 2.0% response, see Fig. 4.8 (c). As shown in Fig. 4.8 (i), the F-sensor exhibits 2.5% response upon exposure to 100 ppm NH_3 for 15 minutes and 8.8% response upon exposure to 1000 ppm NH_3 for 15 minutes. Under 1000 ppm NH_3 exposure cycling test, as shown in Fig. 4.8 (f), the F-sensor possess as similar response characteristics as the R-sensor. The F-sensor shows a stable response of around 12.5% after 4 cycles of NH_3 exposure and N_2 flushing. The results of these three groups of sensors, R-sensor, F-sensor, D-sensor are reproducible, as shown in Fig. 4.9 (a).

For the developed graphene-based gas sensors, sensing response time and recovery time were also investigated. The response time was defined as the time re-
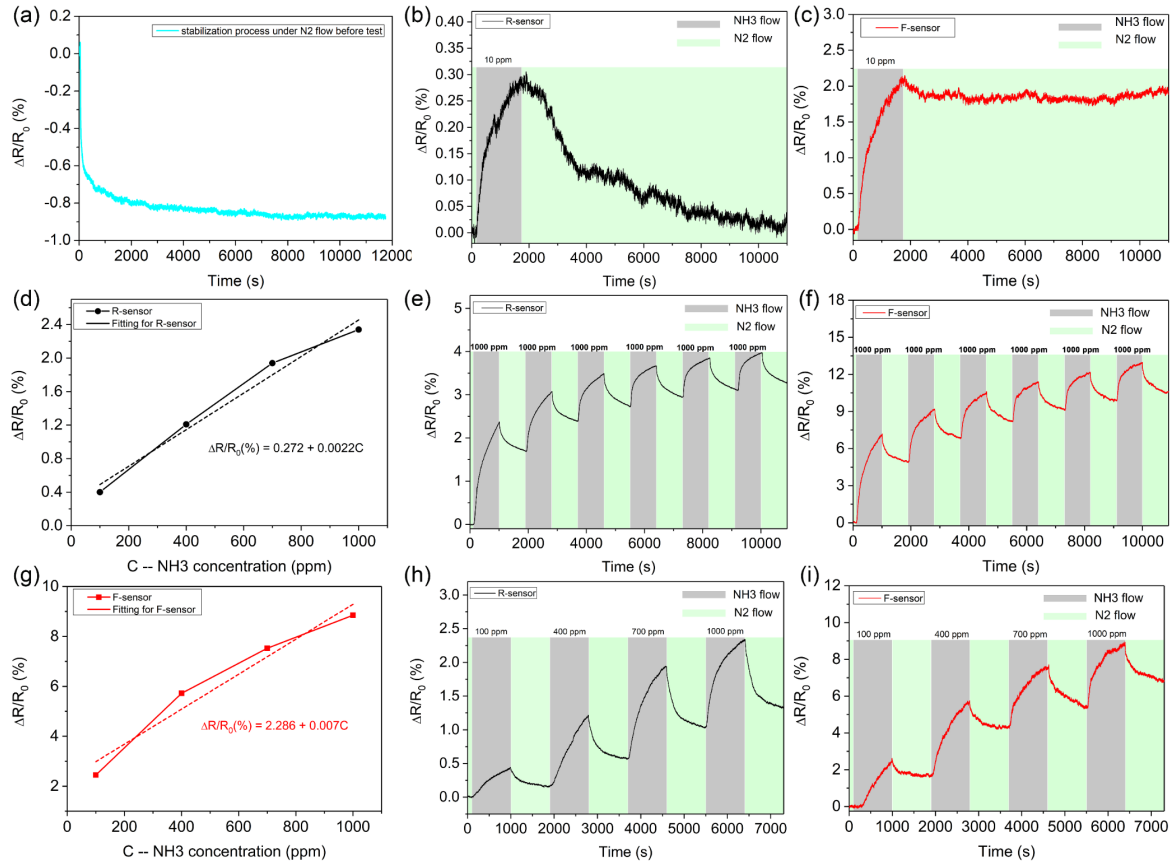
Figure 4.8 Typical sensing characteristics of graphene-based sensors (R-sensor and F-sensor) towards NH_3 gas. (a) Sensor stabilization process under N_2 flow. Typical dynamic response of sensors upon exposure to low concentration of NH_3 at 10 ppm: (b) R-sensor, (c) F-sensor. (d) Response linear fitting of reference sensor (R-sensor). Typical dynamic response of sensors under 1000 ppm NH_3 cycling exposure test, (e) R-sensor, (f) F-sensor. (g) Response linear fitting of F-sensor. Typical dynamic response of sensors upon exposure to successive different concentrations of NH_3 ranging from 100 ppm to 1000 ppm, (h) R-sensor, and (i) F-sensor.

quired for the sensor resistance to reach 63.2% of the estimated maximum during the NH_3 exposure period, corresponding with a one-time constant in a first-order dynamic system; and the recovery time was defined as the time required for resistance to decrease to 63.2% from the maximum value reached during exposure to NH_3 towards to the recovered state [176]. The response time and the recovery time correspond with the one-time constant in a first-order dynamic system. To analyze the response time and recovery time for each sensor, the dynamic response versus time curve for the corresponding period was fitted by the exponential decay formula:
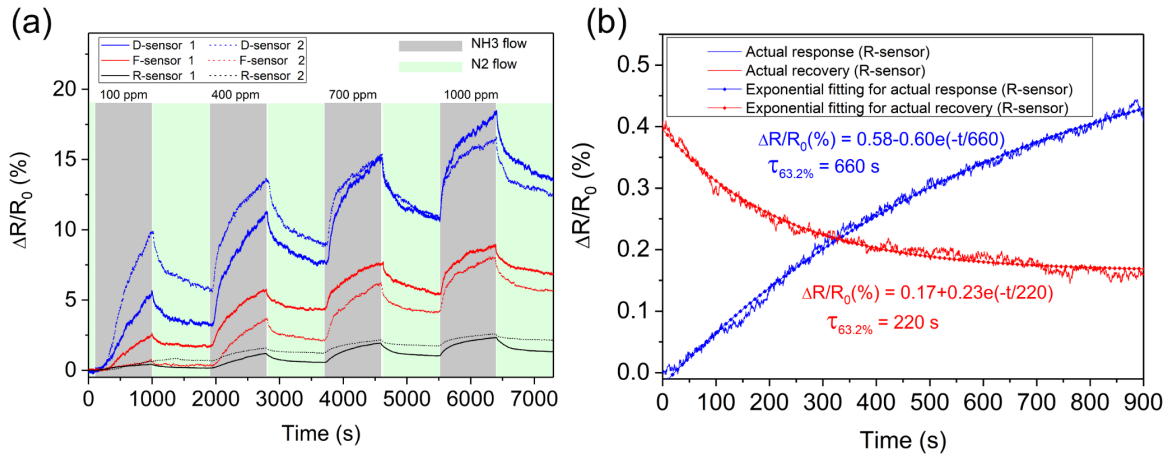
Figure 4.9 Reproduced sensing measurement results and the responding curve fitting. (a) Reproduceable results of D-sensor, F-sensor, R-sensor exposure to different concentration of NH$_3$. (b)Sensor dynamic response exponential fitting and sensor recovery exponential fitting upon exposure to 100 ppm NH$_3$

$$\Delta R/R(\%) = Ae^{\frac{-t}{t_0}} + B \tag{4.1}$$

in which t_0 and B were the response/recovery time and the steady-state response, respectively. For example, the response curve fitting for the reference sensor (R-sensor) upon 100 ppm NH$_3$ is demonstrated in Fig. 4.9 (b),

$$\Delta R/R(\%) = (-0.60)e^{\frac{-t}{660}} + 0.58 \tag{4.2}$$

so the response time t0 is 660 s. Similarly, the recovery curve fitting for the R-sensor upon 100 ppm NH$_3$ gives:

$$\Delta R/R(\%) = (0.23)e^{\frac{-t}{220}} + 0.17 \tag{4.3}$$

so the recovery time is 220 s. As displayed in Fig. 4.8 (d) and (g), the response increases monotonically with the rising of NH$_3$ concentration. The slope of the linear regression fitting for D-sensor is 0.014 ppm^{-1}, suggesting the best sensitivity among these three developed sensors.

Figure 4.10 Sensor response upon exposure to different concentrations of NH_3 ranging from 1000 ppm to 100 ppm: (a) R-sensor, (b) F-sensor, (c) D-sensor. (d) D-sensor response upon exposure to 100 ppm NO gas.
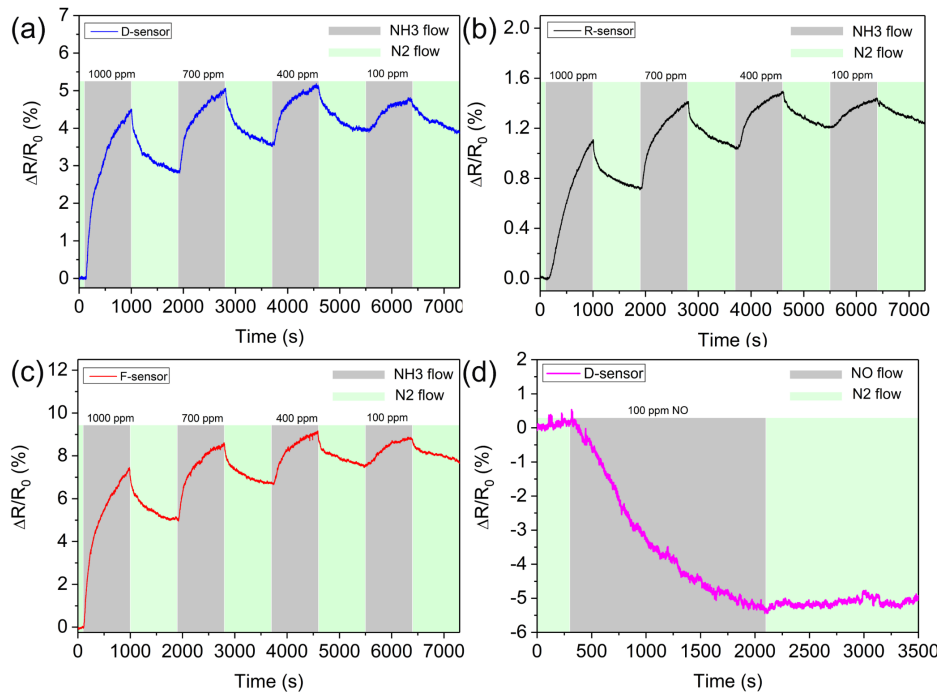
Additionally, sensing characteristics upon exposure to a decreasing concentration of NH_3 ranging from 1000 ppm to 100 ppm were also investigated, as shown in Fig. 4.10 (a) - (c). With the NH_3 concentration decreasing, the sensors show an increasing gross response as well as a decreasing net response, which can be attributed to the partial recovery within 15 minutes purging time. To investigate the specific sensing response of the developed graphene-based gas sensor, the D-sensor was exposed to 100 ppm of NO gas. As shown in Fig. 4.10 (d), D-sensor shows a 5.5% response upon to 100 ppm NO and shows no recovery at the same conditions as NH_3 sensing. NO exhibits electron withdrawing behavior and shifts Fermi level towards the band gas while NH_3 exhibits electron donating behavior [174].

In terms of the sensitivity and recovery, the D-sensor exhibits the best sensing performance among the developed sensors (R-sensors, F-sensors, D-sensors), demonstrating 2.8% response towards 10 ppm NH_3 and 18.5% response towards 1000 ppm NH_3, which could be attributed to a thinner deposition layer than the R-sensor and more homogeneous deposition layer than the F-sensor, respectively. This indicates that the sensing performance could be affected by the morphology

Table 4.1 Characteristics of graphene-based gas sensors for ammonia detection. C_{NH_3}: the concentration of ammonia, unit: ppm. MC:micromechanical cleavage. ME:mechanical exfoliation. PECVD: plasma enhanced CVD. LPE: liquid phase exfoliation. HM: Hummers' method. MHM: modified Hummers' method. EP: electro-polymerization. CP: chemical polymerization. Conditions: the temperature conditions of response and recovery, respectively.

Materials	Methods	C_{NH_3} (ppm)	Response (%)	Conditions
graphene [101]	MC	1	4	RT/150 ^oC
few layer graphene [102]	ME	1000	1	RT/RT
vertically aligned graphene [109]	PECVD	10000	13	RT/RT
graphene foam [177]	CVD	1000	30	RT/120 ^oC
graphene [178]	CVD	1000	90	RT/200 ^oC
graphene/Au particle [179]	CVD	60	8	RT/infrared
graphene nanomesh [180]	CVD	100	3.8	RT
graphene/PANI [4]	CP	20	3.65	RT
graphene/Pd decoration [181]	CVD	100	2.1	150 ^oC
graphene [182]	LPE	100	0.3	RT/RT
fluorinated graphene [183]	PECVD	100	3.8	RT/RT
Graphene [184]	CVD	1300	1.5	RT
Ti/graphene [185]	CVD	400	17.9	RT/UV
graphene/polypyrrole [186]	CVD, EP	1	1.7	RT
graphene/V$_2$O$_5$ [187]	CVD	100	295	RT+UV
Graphene-FMNS,our work	LPE	10/1000	2.8/18.5	RT/RT/RT
rGO-CuPc [188]	MHM	3200	15.4	RT
P doped graphene [189]	HM	100	5.5	RT
rGO/Pt decoration [190]	MHM	1000	10	RT
3D rGO micro-pillar [191]	ALD	10	60	RT
sulfonated rGO hydrogel [192]	MHM	20	7.1	RT

of graphene deposited on the sensors. The D-sensor sensitivity even outperforms some of the recently reported graphene-based NH$_3$ sensors in literatures, as listed in Table. 4.1. There, however, most of the graphene-based sensing element materials were fabricated by more complicated and much costlier processes, like either CVD or the modified Hummers' method.

4.4   The roles of FMNS on NH$_3$ gas sensing

The role of FMNS for the graphene exfoliation and stabilization of its aqueous dispersion was previously reported experimentally [171]. Additionally, the underling mechanism has been studied in chapter 3 *via* all-atom molecular dynamics simulations [125]. The FMNS case model contained one monolayer graphene flake, 2 FMNS molecules, and 20 NH$_3$ molecules. The bare case model was also created for the reference, involving one monolayer graphene flake and 20 NH$_3$ molecules. The monolayer graphene contained 680 C atoms and was 4 nm x 4 nm large in both cases. The simulation box size was 9 $nm \times$ 9 $nm \times$ 9 nm. The modeling parameters setting refer to the modelling part in chapter 3.

The starting configurations of both models are displayed Fig. 4.11 (a) and (c), all the NH$_3$ molecules distributed randomly in the simulation box whilst the FMNS molecules were aligned parallel to the graphene flake in the FMNS case. The representative snapshots after equilibration are displayed in Figure Fig. 4.11 (b) and (d). In the bare case, just a few NH$_3$ molecules attached to the graphene flake. In the FMNS case, the tails of FMNS molecules were attached to the graphene flake firstly and then the NH$_3$ molecules were anchored to the FMNS heads. This kind of interaction between NH$_3$ molecules and FMNS heads can be attributed to the hydrogen bond formation. The FMNS molecules attach non-covalently to the surface of graphene flakes *via* π - π stacking interactions. The hydrophilic nature of FMNS further stabilizes the G-FMNS flake dispersion in the solution.

Typical morphology of NH$_3$ molecules in both cases are analyzed, as shown in Fig. 4.12 . In the FMNS case, FMNS sticks to the surface of the graphene flakes due to the π - π stacking interaction [125]. Intriguingly, phosphate groups of FMNS molecules act as anchor sites to attract NH$_3$ molecules surrounding the FMNS heads, as shown in Fig. 4.12 (a)-(b). Instead, in the Bare case, considering that there are no effective and available anchor sites for NH$_3$ molecules, the NH$_3$ molecules distribute randomly and avoid the graphene flake, as shown in Fig. 4.11 (a)-(d). Additionally, the number density distribution of both FMNS heads and NH$_3$ molecules in the FMNS case as well as the number density distribution of NH$_3$ molecules in the Bare case are displayed in Fig. 4.12 (c). In the FMNS case, FMNS molecules exhibit two peaks at both sides of graphene flake owing to the π - π stacking interaction.
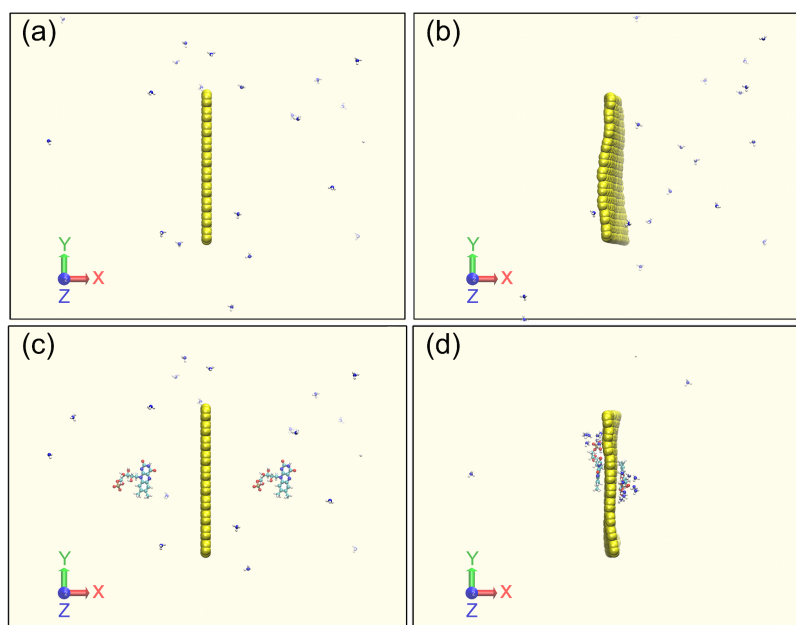
Figure 4.11 Representative snapshots for Bare case and FMNS model upon exposure to NH$_3$, respectively. (a) Starting configuration of bare model. (b) Representative morphology snapshot in bare model. (c) Starting configuration of FMNS model. (d) Representative morphology snapshot in FMNS model. Color code is the same as shown in Scheme1.

NH$_3$ molecules show similar behavior to FMNS molecules in the FMNS case, while the NH$_3$ molecules display no peaks since NH$_3$ molecules are distributed over the whole simulation box in the Bare case. This further corroborates the morphology observations as shown in Fig. 4.12 (a)-(b).

Radial distribution function (RDF) of NH$_3$ molecules relative to the phosphorus atom in the FMNS case are illustrated in Fig. 4.12 (d). The average distance of NH$_3$ molecules from the phosphorus atom of FMNS molecules is around 0.39 nm. According to the criteria of the formation of hydrogen bonds in Visual Molecular Dynamics (VMD) (default cut-off distance 3.0 Å, and default cut-off angle 20°) [193], the representative morphology of both NH$_3$ molecules and FMNS molecules in the FMNS case were analyzed, and it is found that hydrogen bonds were formed between NH$_3$ molecules and FMNS head groups, as displayed in the inset of Fig. 4.12 (d). This interesting finding agrees well with the expectation that NH$_3$ molecules can form hydrogen bonds with –OH groups existing in FMNS. In previous publications on r-GO based ammonia gas sensors, their sensitivity was enhanced compared to pristine graphene based sensors for the reason that NH$_3$ molecules could be efficiently adsorbed by the abundant oxygen containing functionalization groups
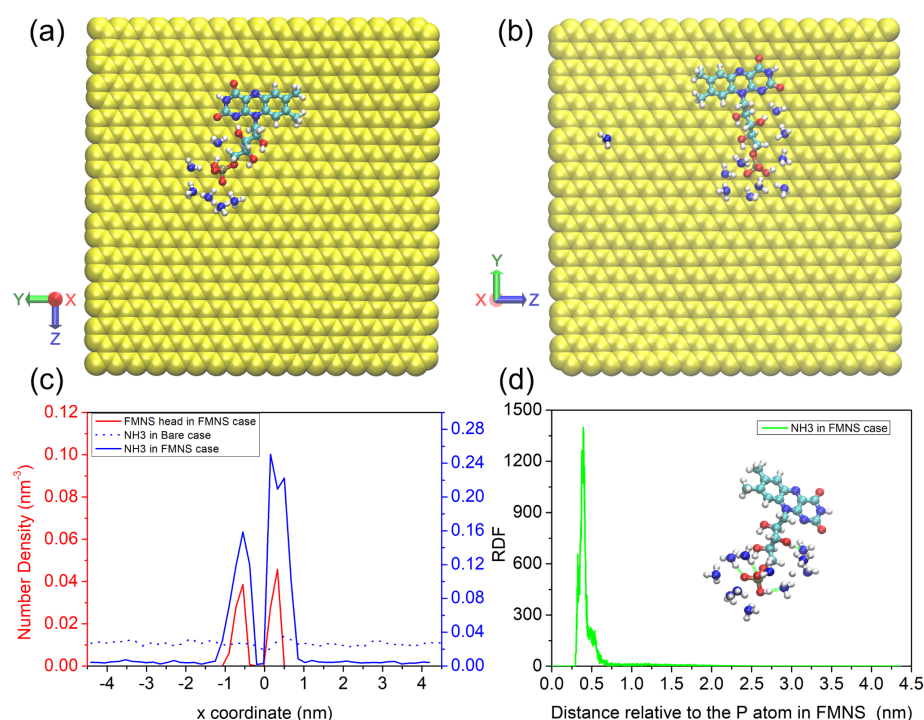
Figure 4.12 Representative morphology snapshots of NH_3 molecules on the monolayer graphene flakes non-covalently functionalized by FMNS molecules in FMNS model. (a) Top view. (b) Bottom view. (c) Density distribution of FMNS molecules and NH_3 molecules along x coordinate in both bare model and FMNS model, respectively. (d) Radial distribution functions (RDF) of NH_3 molecules as function of the relative distance to the center of mass of FMNS molecules in FMNS model. Color code is the same as shown in Fig. 4.1.

(epoxy groups, hydroxyl groups, carboxyl groups, etc.) on the rGO surface through hydrogen bond interactions [192]. In the current work, the same purpose is achieved intentionally by the adsorption of FMNS molecules on pristine graphene *via* π - π stacking interaction. The molecules provide artificial reactive sites due to the abundant hydroxy groups, which can trap NH_3 molecules efficiently *via* hydrogen bonding interaction.

4.5   Working mechanism of gas sensing

Pristine graphene is chemically inert and weakly interacts with analyte gas [186],for example, intrinsic response of mechanical exfoliated graphene is very small, even upon exposure to high concentration (1000 ppm) NH_3 gas [102]. Functionalization of graphene either by non-covalent approaches or by covalent approaches has been
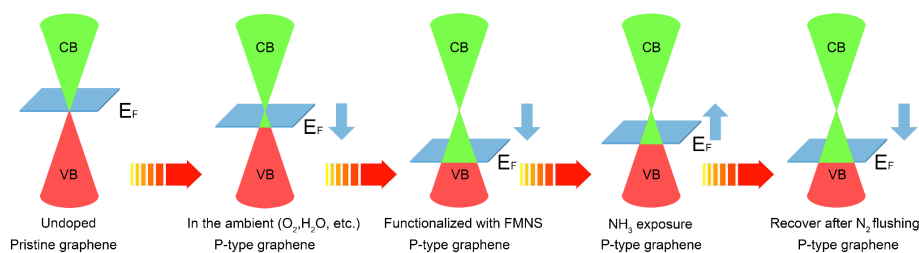
Figure 4.13 Shift of Fermi level in graphene flakes in FMNS model.

proven to be an effective way to prompt the interaction between graphene and analyte gas that was shown both theoretically and experimentally [103]. Covalent functionalization usually involves harsh chemicals and damages the sp^2 electronic structure in graphene, whilst non-covalent functionalization remains the intact structure as well as the excellent electrical property of graphene and gains prominence [194].

In this work, graphene was non-covalently functionalized with FMNS molecules *via* π - π stacking interaction and acted as support substrate layer of sensing element. FMNS molecules exhibit several critical roles from the graphene preparation to gas sensing. At the exfoliation stage, the FMNS molecules attach tightly to the surface of graphene flake due to π - π stacking interaction and keep the colloidal dispersion stabilized in aqueous solution by creating high potential of mean force energy barrier between the graphene flakes [125] As sensing element material, pristine graphene is a semimetal with a zero band gap. [195]. However, in the ambient conditions, pristine graphene usually shows p-type semiconductor behavior with holes carriers as the major carriers due to the absorption of water or oxygen molecules, which shifts the Fermi level of graphene in the valence band due to an increase of hole carriers concentration [181]. Additionally, the electronic structure of graphene can be modulated by doping with various aromatic molecules through π - π stacking interaction [196].

Here, FMNS molecules present electron-withdrawing groups. They impose p-type doping on graphene, which in turn shifts the Fermi level further into the valence band. This leads to a further increase of hole carrier's concentration in the graphene flake. Theoretical studies reveal that NH$_3$ is one of the strongest electron donors with considerable amount of electron transfer to graphene (arouond $0.027e^-$) compared with other electron donors [197, 103]. Upon exposure to NH$_3$ gas, electrons from NH$_3$ molecules are indirectly shifted towards graphene through
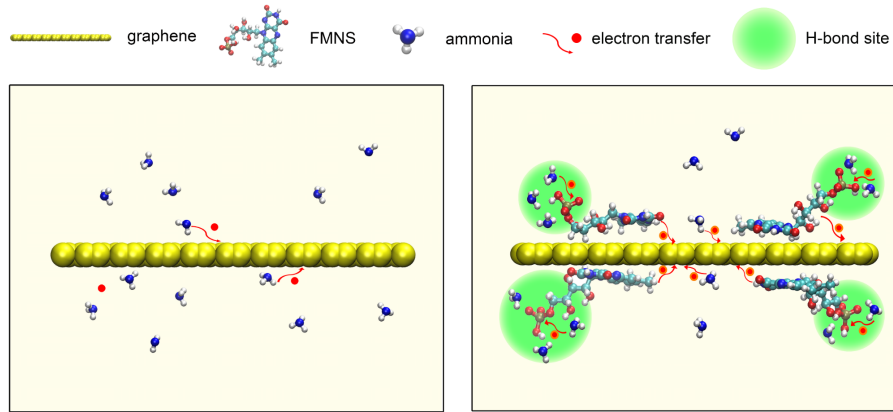
Figure 4.14 Charge carriers transfer from NH_3 molecules to graphene flakes. (Left panel) Few carriers transfer from NH_3 to graphene. (Right panel) Increased carriers transfer from NH_3 to graphene *via* FMNS anchor sites due to the hydrogen bond formation in FMNS model. Color code is the same as shown in Fig. 4.1

the intermediate FMNS molecules [103], inducing n-type doping as well as a Fermi level shift towards the Dirac point. Graphene has carrier-density-dependent conductivity, the resistivity follows the standard dependence:

$$\rho^{-1} = \sigma = ne\mu \qquad (4.4)$$

where σ is conductivity, μ is carrier mobility, n is carrier concentration [90].

Following the depletion of holes in graphene, the conductance of graphene is decreased and in turn the electrical resistance is increased, that is seen in ammonia exposure experiments as shown in Fig. 4.7. During flushing of sensors with pure nitrogen, weak hydrogen bonds are broken and NH_3 molecules are released taking electrons back. The donated electrons are returned from graphene to FMNS, and the Fermi level is shifted towards the valence band. In the experiment, this is seen as a returned to a lower sensor resistance, namely sensor recovery. The corresponding shifts of Fermi level in graphene flakes are schemed in Fig. 4.13.

To summarize, in the Bare case, weak binding interaction takes place between NH_3 molecules and graphene flakes since there is no FMNS functionalization of graphene [186]. Very few electrons from NH_3 molecules can be transferred to graphene, which results in a weak response of a graphene-based gas sensors even upon exposure to high concentrations of NH_3 gas [198]. In the FMNS case, FMNS molecules

not only work as p-type dopant to graphene but also as active anchor sites for NH_3 molecules due to hydrogen bonding interaction, more electrons are transferred from NH_3 molecules to graphene and render graphene responsive even upon exposure to low concentrations of NH_3, as schemed in Fig. 4.14. Adsorption of NH_3 molecules on FMNS through specific hydrogen bonding interaction is much weaker than covalent bonding [199], bestowing a good recovery for the G-FMNS based sensor towards NH_3 sensing [200].

4.6 Summary

In this chapter, pristine graphene non-covalently functionalized by FMNS has been produced for the application as NH_3 sensing materials in a chemiresistive type gas sensor. Raman characterizations indicate that the graphene flakes exhibit good structural quality with few defects. The optimized ammonia sensors demonstrate outstanding performance: ultralow limit-of-detection (1.6 ppm), excellent sensitivity (2.8%, 10 ppm; 18.5%, 1000 ppm), reproducibility, reversibility, low power consumption (work temperature, 25 ^{o}C) as well as low cost. Additionally, the roles of FMNS from graphene preparation to NH_3 sensing are elucidated *via* all-atom molecular dynamics simulations: (1) stabilizer for the graphene dispersion, (2) p-type dopant for graphene-based sensing element, and (3) active adsorption sites for NH_3 gas sensing.

Chapter 5

Highly selective pristine graphene-based gas sensors

Selectivity is a long-standing issue for chemiresistive type gas sensors. In this chapter, machine learning techniques will be employed for the signal processing in order to enhance the selectivity of the gas sensors. Additionally, with unsupervised or supervised machine learning algorithms, sensing signals of various odors could be clustered/separated, which facilitates the odors discrimination and identification. The developed strategy may facilitate miniaturization of e-noses, digitization of smells, and identification of VOCs in various emerging applications.

5.1   Motivation

Olfaction is an evolutionary old and rather simply constructed sensory system, and it provides sophisticated access to information about our surroundings [201]. The olfactory system consists of the region from the olfactory epithelium to the olfactory cortex [202]. Odorants, which are volatile and hydrophobic compounds possessing molecular masses of smaller than 300 Daltons [203], reach the mucus-covered olfactory epithelium and then bind to specific olfactory receptors in nasal cavity, and subsequently the odorant information is conveyed from the olfactory sensory neurons to the olfactory cortex of the cerebrum, in which odor perception takes place [204]. By means of learning or training, the human brain could memorize different potentials or signals induced by different odorants, which enable human beings with the ability to identify odors [205]. Inspired by the biological example, electronic

noses (e-noses) in combination with efficient machine learning techniques aim to achieve a similar performance and thus to digitalize the sense of smell [206]. In this scenario, e-nose, or artificial nose, refers to an instrument, which comprises an array of electronic chemical sensors with partial specificity and an appropriate pattern-recognition system, capable of recognizing simple or complex odors, defined by Gardner in 1993 [207]. Over the past decades, a variety of gas sensors have been developed for e-nose systems, which demonstrate promising potential in a wide range of applications [208–210, 22, 211].

Despite the significant progress of e-noses, their development still remains challenging due to the complex layout design of sensor array with multitude of receptor types or sensor materials, and the need of high working temperature. For instance, the critical hardware component of a typical e-nose system is a sensor array consisting of a number of diverse sensors with semi-selectivity [212–215], which is analogous to the olfactory receptors in human olfactory system. Metal-oxide-semiconductor (MOS) type gas sensors have prevailed in commercial e-nose market owing to their merits of low cost, feasible fabrication, good sensitivity, etc [216, 217]. Nevertheless, as presented in chapter 1, MOS type sensors usually operate at an elevated temperature in the range of 200–500 ^{o}C since thermal energy is essential to activate the adsorption of ionized oxygen species as well as to overcome the barriers of sensing reactions, in which a heater has to be taken into the consideration of design in the sensor device [218]. Therefore, a lot of commercialized e-nose products are usually large, expensive, non-portable and laboratory instruments. On the other hand, graphene is an excellent candidate of sensing materials as discussed in the chapter 1 and chapter 4.

Typically, in feature extraction and pattern recognition algorithm of e-nose systems, single thermodynamic feature per sensor (e.g., maximum response or steady-state response S) is prevalently utilized [219]. By contrast, kinetically transient-state features are generally undervalued, which are inherent to the adsorption or desorption interaction between gas molecules and sensing element materials as well as could provide robust quality information [209]. In addition to significantly enhancing gas discriminating performance, e-nose system utilizing transient features exhibit benefits over the conventional algorithms, for instance, improved selectivity, reduced acquisition time as well as prolonged sensor lifetime, etc [220]. Given the fact that multiple transient features could be readily extracted from the sens-

Table 5.1 Physical properties of odor in this work.

Odor	Property	Smell
Eucalyptol(Euca)	Molar mass: 154 g/mol Boiling point: 172 °C Density: 922 kg/m³	Eucalyptus
2-Nonanone(2Nona)	Molar Masse: 142 g/mol Boiling point: 195 °C Density: 820 kg/m³	Fruity/floral
Eugenol(Euge)	Molar mass: 164 g/mol Boiling point: 254 °C Density: 1060 kg/m³	Clove
2-Phenylethanol(2Phe)	Molar mass: 122 g/mol Boiling point: 225 °C Density: 1020 kg/m³	Rose

ing response profile, molecule discrimination capabilities could be maximized while largely scaling down the number of gas sensors involved in the e-nose systems.

In this work, a highly discriminative and ultrasensitive electronic olfaction (e-olfaction) platform for the detection, discrimination, and identification of basic odor molecules is demonstrated, based on the use of a single-channel nano-sensor utilizing non-covalently functionalized graphene as sensing element material. Four odors, including eucalyptol (Euca), 2-nonanone (2Nona), eugenol (Euge), and phenethyl alcohol (2Phe), which are generally employed in olfactory training among patients with olfactory loss [221], as shown in Table. 5.1, are investigated in this work.

5.2   Materials preparation and methods

5.2.1   Graphene dispersion preparation

The product information of materials involved in this work, such as graphite powder, APTS, are described in Table. 2.1. In this work, the optimized recipe for graphene dispersion preparation was as below: 5 mL APTS aqueous solution (1 mg/mL) was mixed with 5 mL graphite powder aqueous solution (30 mg/mL), the mixture was then sonicated for 2 hours by horn-type sonicator (50% amplitude) in an ice bath. Afterwards, the obtained solution was left to stand overnight. To further remove un-exfoliated graphite particles, the suspensions were centrifuged at 4000 rpm for 2 min, and the top 50% supernatant was pipetted out to another centrifugation tube. The rest was discarded. Following feeding deionized (DI) water to the original volume, the supernatant dispersion was then re-dispersed by a mild sonication setup for 10 min in an ice bath. Thereafter, the above centrifugation and re-dispersing procedure were performed twice more. Finally, the aqueous dispersion of graphene functionalized by APTS was achieved.

5.2.2   Sensor device fabrication

The sensor device was fabricated by dielectrophoretic (DEP) alignment of graphene flakes on gold IDE fabricated on silicon wafers. Electrode fabrication was done utilizing a standard microfabrication process comprising photolithography, gold thermal evaporation and lift-off, as introduced in our previous work [112]. IDE structure on the device features gap size of 3 μm and finger width of 4 μm, respectively. Alternating current DEP with a signal generator was applied to deposit graphene on the device, which bridged neighboring electrodes precisely and achieved a homogeneous graphene network on the device. DEP parameters, including frequency of the applied signal (f), peak-to-peak voltage (Vpp), and processing time (t), play a major role in the alignment of graphene flakes. Our optimized parameters were as below: Vpp = 10 V, f = 200 kHz, t = 30 s. In a typical DEP procedure, a droplet of 10 μL dispersion was pipetted onto the IDE, which was fixed on a probe station, then alternating current with specific frequency was applied on the sensor device for 30 s, followed by

DI water rinsing and N_2 flow drying. Sensor device fabrication was completed, and stored under inert atmosphere (N_2) until use.

5.2.3　Odor vapor preparation

Four basic odors, eucalyptol, 2-nonanone, eugenol, 2-phenylethanol, were investigated in this work. The product information could be found in Table. 2.1 and the physical information is shown in Table. 5.1. A bubbler evaporation system was developed to generate odor vapor as well as deliver odor vapor to the gas chamber [222]. The flow rate of dry nitrogen was tuned by mass flow controller. The source of both carrier gas and dilution gas was nitrogen, whose flow rate was precisely controlled by mass flow controller (MFC). Odor concentration could be finely tuned by combining the flow rate of both carrier and dilution gas.

5.2.4　Odor sensing measurement

Sensing performance of e-olfaction towards both individual odor and odor mixture were evaluated, respectively. The gas chamber was a homemade gas sensing set-up after minor modification, as shown in Fig. 5.1 and applied to measure the electrical property of the sensor upon exposure to individual odor vapor or odor mixture [112]. Upon odor vapor adsorbed by functionalized graphene on the sensor, the electrical conductivity of the sensor shifted due to the occurrence of charge carrier transfer between odor molecules and functionalized graphene. A constant voltage (0.1V) was applied to the sensor and the sensor current was recorded by a source meter. Following that, the path of carrier gas was switched off while the flow rate of dilution gas was increased to desorb and flush odor molecules from the graphene and released sensor recovery. To make the results reproducible, 24 repetition tests were carried out for each odor test on the same condition. Before the initial cycle test, a stabilization process to remove the adsorbed water or other contaminants was performed, in which pure nitrogen flow was active until the resistance of the sensor device approached a plateau state. In this work, a set of visual basic (VB) scripts was developed to automatically manage the whole measurement procedure, including, start time and end time of the odor exposure step as well as odor flushing step, the flow rate of the carrier gas, and dilution gas in a different phase, as well as acquire current information, etc.
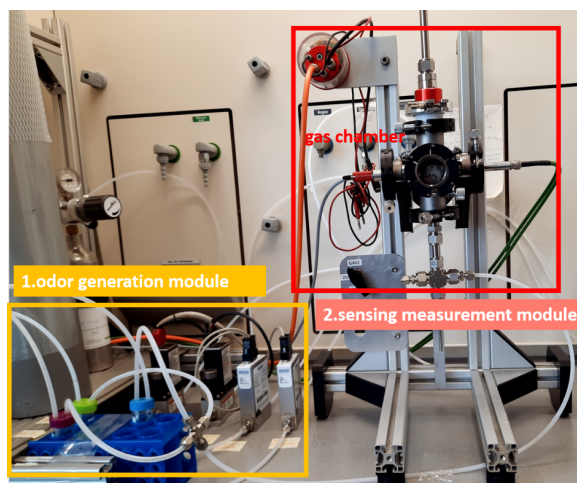
Figure 5.1 Custom-made odor sensing measurement set-up. Odor sensing system consists of two modules, (left) odor vapor generation module, (right) odor sensing measurement module.

5.2.5 Evaluation method of odor discrimination performance

Odor discrimination aims to classify odor scatters with similar features into the same class while odor scatters with distinctive properties into different groups. This goal could be achieved *via* unsupervised machine learning. In this session, 4 odors, as well as odor reference (pure N_2), were discriminated. Before feeding into clustering algorithms, feature data of all odors had transformation preprocessing using StandardScaler, MinMaxScaler, and L2 normalization algorithms. The transformed features were further applied principal component analysis (PCA) for dimensionality reduction and analyzed with diverse clustering algorithms.

5.2.6 Evaluation method of odor identification performance

Odor identification is to predict the label information for the new odor from known labels after algorithm training. This could be achieved *via* supervised machine learning. In this session, 4 odors, as well as odor reference (pure N_2), were identified with labels. In contrast to unsupervised machine learning, odor labels target had to be predicted as well [223]. All the features together with additional target (odor labels) information were split up into two sets, 75% data was used to train classifier algorithms while the rest 25% data was used to test classifier algorithms. Before

the training data were fed into classifier algorithm, for example, linear discriminant analysis (LDA) algorithm, the features of the training dataset were transformed with StandardScaler algorithm. Afterward, the transformation parameters generated from training data were applied upon the test data set to generate transformed test data set. The prediction accuracy achieved by the LDA algorithm could be obtained. Meanwhile, the performance of LDA classifier algorithms was achieved using K-Fold Cross-Validation (K = 10) approach. The above data processing of both unsupervised and supervised machine learning was conducted *via* Python script.

5.2.7   Modelling

Molecular dynamic simulation work was performed with GROMACS 5.1.2 package [224]. All molecules were modeled utilizing the GROMOS 54a7 force field [119], in which forcefield parameters were generated using online server Automated Topology Builder (ATB) and Repository Version 3.0 platform (https://atb.uq.edu.au/) [225]. There were two parts in the simulation work, including stabilization of APTS functionalized graphene in water aqueous dispersion, as well as odor molecules interaction with APTS, functionalized graphene. In the first session, the system involved a graphene flake, 4 APTS molecules, 12 sodium ions as well as water molecules in a simulation box. Following reaching equilibrium of the system, APTS molecules non-covalently adsorbed on graphene surface tightly due to π-π stacking interaction [125]. Functionalized graphene with APTS were then transferred to another simulation box. In the second simulation session, apart from APTS functionalized graphene, odor molecules were also added into the box (individual odor or binary odor mixture) as well as nitrogen molecules. The total amount of odor molecules was 20, in other words, in the binary odor mixture case, 10 molecules for each odor inside the box. The modeling parameters refer to the modeling section in chapter 3.

To investigate the binding energy and charge transfer amount between odor molecules and APTS molecules, stationary calculations for all configurations were performed using the Density-Functional based Tight-Binding (DFTB) approach. In all calculations, the self-consistent charge extension (SCC) method was employed [226], implemented in the DFTB+ code with third order corrections (DFTB3) [227], and utilizing the 3ob-3-1 Slater-Koster parametrization. The partial charges were determined by means of Mulliken population analysis [228].The binding energy be-
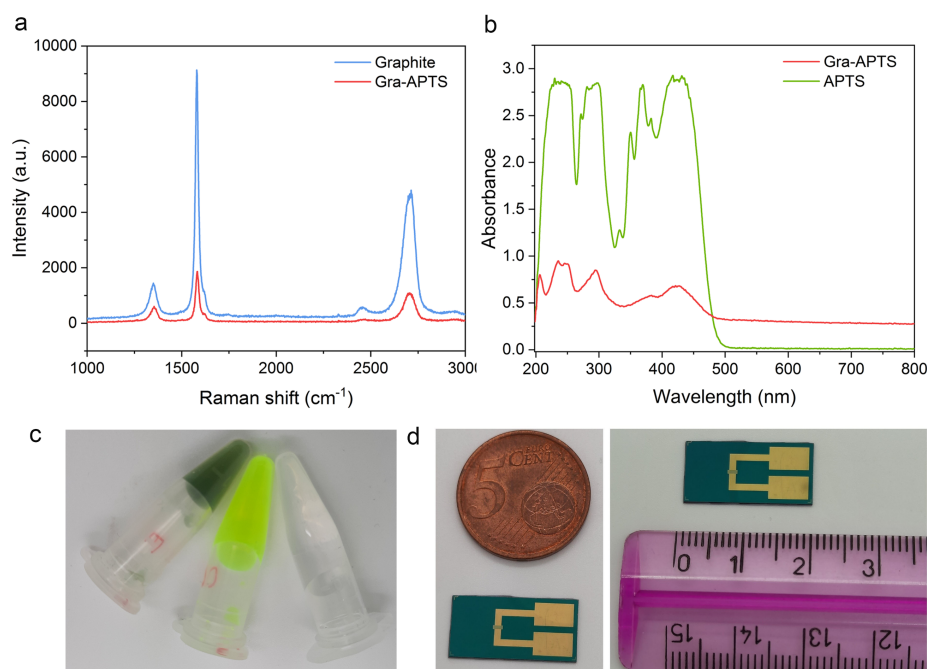
Figure 5.2 Characterization of prepared graphene dispersion. (a) Raman spectrum of prepared graphene. (Blue) Graphite. (Red) APTS functionalized graphene dispersion. (b) UV-vis absorption spectra of prepared graphene. (Green) APTS aqueous solution. (Red) APTS functionalized graphene dispersion. (c) Digital photograph of prepared samples. (Left) APTS functionalized graphene dispersion, (middle) APTS aqueous solution, (right) DI water (d) Sensor sample of e-olfaction system. (Left) Sensor sample comparison with 5-Euro cent. (Right) Sensor sample size measurement.

tween different molecular structures were obtained *via* the total energy difference between bonded and isolated states. This part calculation of DFTB was performed by my colleague Dr. Arezoo Dianat.

5.3   Graphene materials characterization

Fig. 5.2 (a) shows the Raman spectra of both graphite and prepared graphene. Both Raman spectra display three dominant peaks at wavenumber of around 1350, 1580, 2700 cm^{-1}, corresponding to the D, G and 2D graphitic bands. The D band represents either edges or defects in the lattice and the G band represents sp^2-hybridized carbon bonds in graphene and graphite [166]. The D band is quite weak in graphite (I_D/I_G = 0.16). When the size of graphene decreases in the course of exfoliation, the
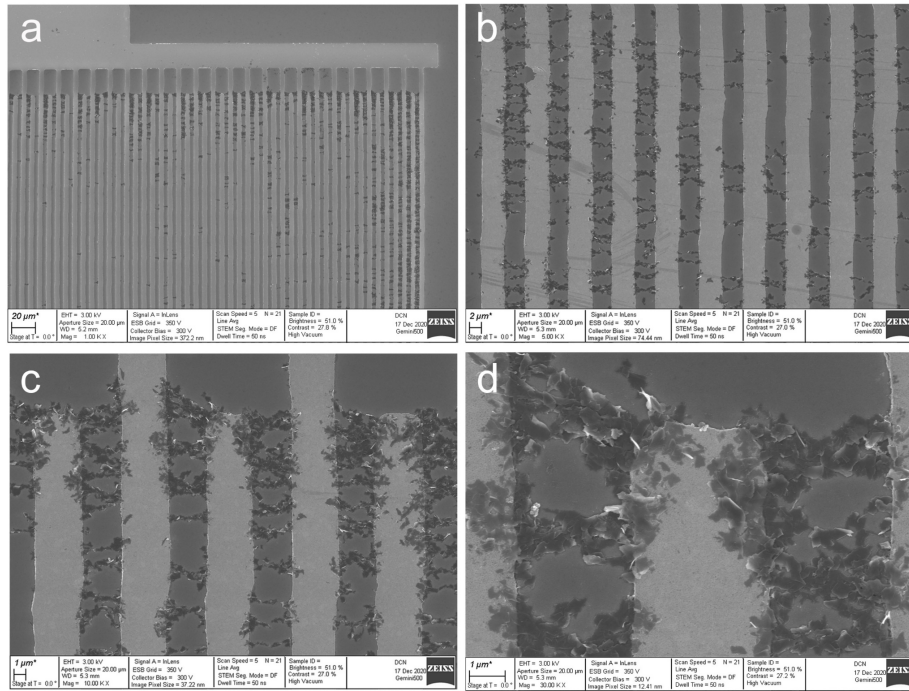
Figure 5.3 SEM characterization of deposited graphene on IDE surface. (a) Magnification: 1 000×. (b) Magnification: 5 000×. (c) Magnification: 10 000×. (d) Magnification: 30 000×.

amount of graphene edge exposed per flake increases, which gives a rise to the D band intensity (I_D/I_G = 0.32). This value is much lower than that of chemically reduced graphene oxide (I_D/I_G > 1.0) [167]. The 2D band determines the number of graphene layer. The feature of 2D band and the ratio of the 2D band to the G band intensity (I_{2D}/I_G = 0.57) imply the existence of multi-layer graphene in our sample [170]. Moreover, a downward shift to a lower wavelength (about 17 cm^{-1} lower than that of the graphite) is observed on the 2D band of graphene sample, which corroborates the multi-layer nature of Pyrene-derivative-functionalized graphene in the sample [229, 230].These Raman spectra results suggest that the achieved graphene flakes are multi-layer graphene with few defects.

The UV-vis absorption spectra of both APTS aqueous solution and prepared graphene aqueous dispersion are shown in Fig. 5.2 (b). There are three strong absorption bands observed at around 235, 295, 424 nm in the UV-vis spectra of APTS, which are typical absorption bands of APTS in water [231]. Generally, graphene is characterized by one absorption band at 228 nm due to the electronic π-$\pi*$ transitions of the
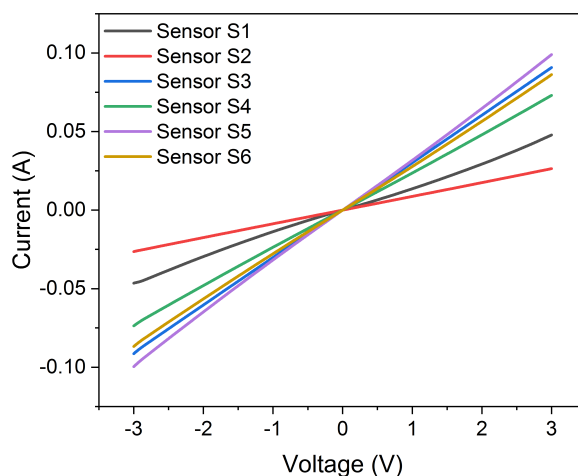
Figure 5.4 Electrical characterization of e-olfaction sensor. Sensor S1 to sensor S6.

C-C bond [232], as well as another absorption band at 268 nm due to the electronic π-$\pi*$ transitions of the C=C bond in the sp^2 lattice [157]. However, as seen in shown in Fig. 5.2 (b), the presence of APTS on the graphene flake nearly overlap those of graphene between 250 and 450 N_2, which could validate the occurrence of APTS in graphene aqueous dispersion [233]. The UV absorption spectra result demonstrate the efficient coupling between graphene and APTS molecules. The digital image of the prepared dispersion as well as the sensor device are illustrated in Fig. 5.2 (c) and (d), respectively.

Morphology of graphene flakes are shown in Fig. 5.3. Employing DEP electrical field, graphene flakes grow initially across the edge of electrodes, then converge, and finally make adjacent electrodes connected electrically. These graphene functions as the conducting path as well as sensing elements for the sensor device. The amount and morphology of deposited graphene could be tuned *via* the DEP parameters (Vpp, f, t). The average size of achieved graphene flake is around several hundred nanometers, similar to our previous synthesis [111]. As shown in Fig. 5.4, the current versus voltage (I-V) curve of developed sensors demonstrate good linearity from -3 V to 3 V, indicating an excellent ohmic contact between the APTS functionalized graphene flakes and the electrodes.

5.4   Work principle of graphene-based e-olfaction platform

Graphene dispersion was prepared by exfoliation of graphite assisted with APTS in aqueous solution, as shown in Fig. 5.5 (a). While the usual approach for graphene sensor surface functionalization with pyrene derivatives rely on its modification after the deposition step [234], here the exfoliation and functionalization take place at the same time [235], saving material processing time. Owing to the sulfonic groups grafted on a pyrene base, APTS molecules exhibit hydrophilic behavior and prefer to stick to graphene surface *via* π-π stacking interactions. In our previous study, it was revealed that specific functionalized material on graphene through non-covalently bonding played vital roles in graphene sensing application, which were stabilizers for the graphene dispersion, p-type dopant for graphene sensing materials, and active adsorption sites for analyte gas [111]. Following removing excess un-exfoliated graphite particles from the dispersion, high quality of functionalized few-layer-graphene dispersion was achieved. A droplet of graphene dispersion was pipetted onto a pre-fabricated sensor device by the dielectrophoresis (DEP) approach. Applying alternating current (AC) field, graphene flakes were aligned precisely across the gaps between adjacent electrodes and acted as sensing element materials. Upon odor vapors approaching to graphene on the sensor surface, charge carriers transfer occurred between odor molecules and functionalized graphene, resulting in a shift of sensor's conductance.

Odor sensing system was composed of two modules, odor vapor generation module and electrical measurement module, as shown in Fig. 5.5 (b). In odor vapor generation module, path (A and C) traversing odorant solvent functioned as odor supplier, path (B) traversing a reference bottle functioned as odor diluter. The source of both carrier gas and dilution gas was high purity dry nitrogen, whose flow rate was precisely controlled by a mass flow controller (MFC). Odor concentration could be finely tuned by combining the flow rate of both carrier gas and dilution gas. In electrical measurement module, electrical conductance evolution of the sensor was monitored and saved.

Raw data acquired from the odor sensing system was sensor current evolution as a function of the operation. Following features extraction, part of feature data,
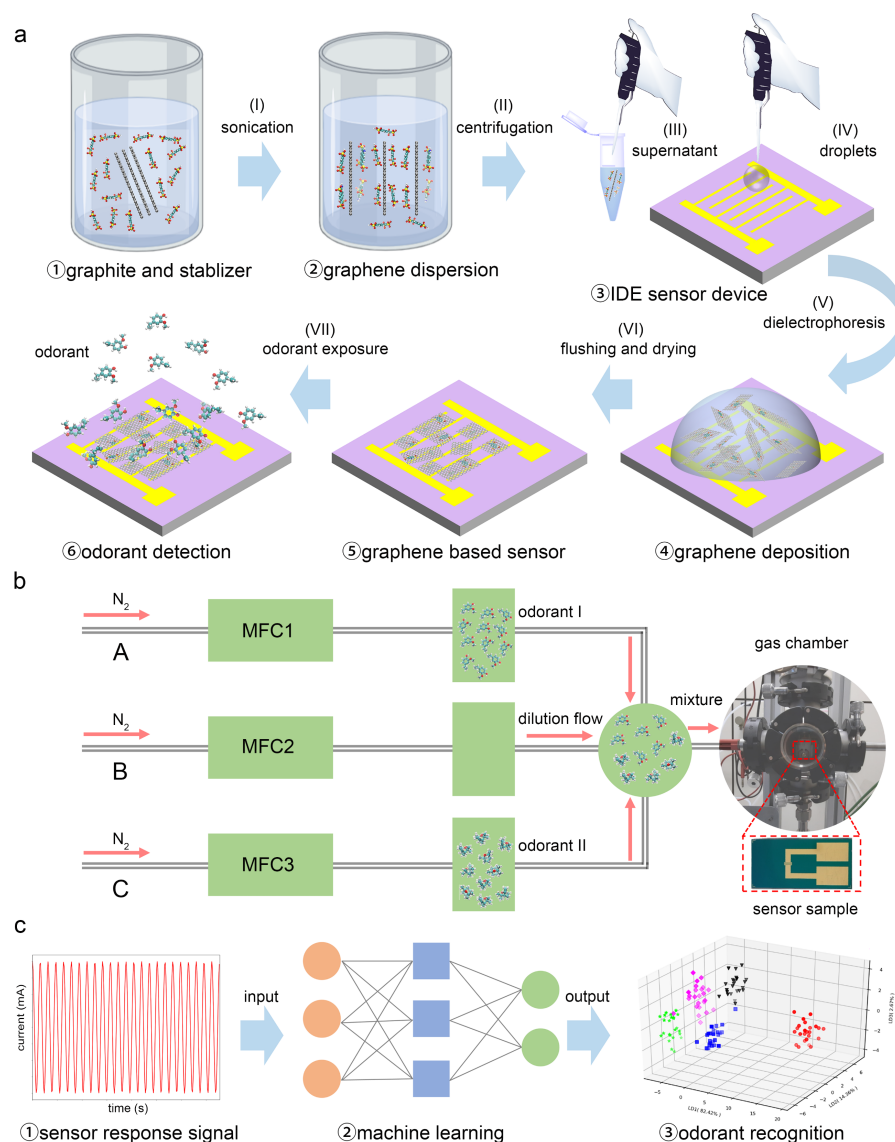
Figure 5.5 Scheme of sensor fabrication, sensing characterization platform and results analysis. (a) Procedure of sensor fabrication includes graphene preparation, sensor fabrication and odor exposure. (b) Odor sensing system comprises odor vapor generation module and electrical measurement module. In individual odor sensing experiments, carrier gas path (A or C) and dilution gas path B remain active. In odors mixture sensing experiments, carrier gas paths (A and C) and dilution gas path B remain active. All sensing experimental work operate at room temperature (20 ^oC). (c) Odor sensing signal processing and odor recognition by machine learning algorithms.

as well as odor label data, were fed into machine learning algorithms in an attempt to train classifier algorithms, while the rest were remained for odor identity prediction, as illustrated in Fig. 5.5 (c). In all situations, each sensing test (containing odor

exposure phase and odor flushing phase) was performed 24 times on the same condition, which was achieved automatically by visual basic (VB) script.

5.5   Signal processing and features extraction method

In the pattern-recognition system of developed e-olfaction, rather than utilizing single thermodynamical feature (such as steady-state response S) as a unique feature, multiple kinetically transient-state features were applied. Raw data dumped from the electrical measurement module was sensor current as a function of working time, as shown in Fig. 5.6 (a). Since a constant voltage (0.1 V) was applied to the sensor device, the sensor resistance evolution profile was readily derived according to Ohm's Law. To extract features from each repetition measurement profile, the sensor resistance profile was split into 24 individual profiles, as shown in Fig. 5.6 (b). Herein, for each measurement, the odor exposure phase lasted 900 s (15 mins) and the odor flushing phase lasted 600 s (10 mins). Sensing response (or fractional change of sensor conductance) was then derived, as shown in Figure 5. 6 (c), which could provide excellent pattern-recognition performance as well as compensate for temperature cross-sensitivity and nonlinearities in the concentration dependence [207]. Following that, sensing response for 24 repetition measurements was performed with L2 Normalization, in which the sensing response of each odor was divided by its norm and as a result, forced to lie on a hyper-sphere of unit radius. The L2 Normalization aimed to compensate for sample-to-sample variations in concentration [219], as shown in Fig. 5.6 (d).

To extract exponential fitting parameters, the sensing response profile was then split into odor exposure curve and odor flushing curve, respectively, as displayed in Fig. 5.6 (e) (f). The first derivative of sensing response and second derivative of sensing response was implemented as well. As shown in Fig. 5.6 (g), the maximum value (k_{max}) in odor exposure phase and the minimum value (k_{min}) in odor flushing phase were obtained. In the second derivative curve, the minimum value (amin) in odor exposure phase was saved, as illustrated in Fig. 5.6 (h). Besides, the area under odor exposure phase curve and odor flushing phase curve (from ta to tb) was calculated and the maximum response (S) value relative to the baseline was saved. In total, 11 transient-state features, containing exponential fitting parameters ($a_1, b_1, c_1, a_2, b_2, c_2$) as well as kinetical parameters ($S, k_{max}, k_{min}, a_{min}, Area$),
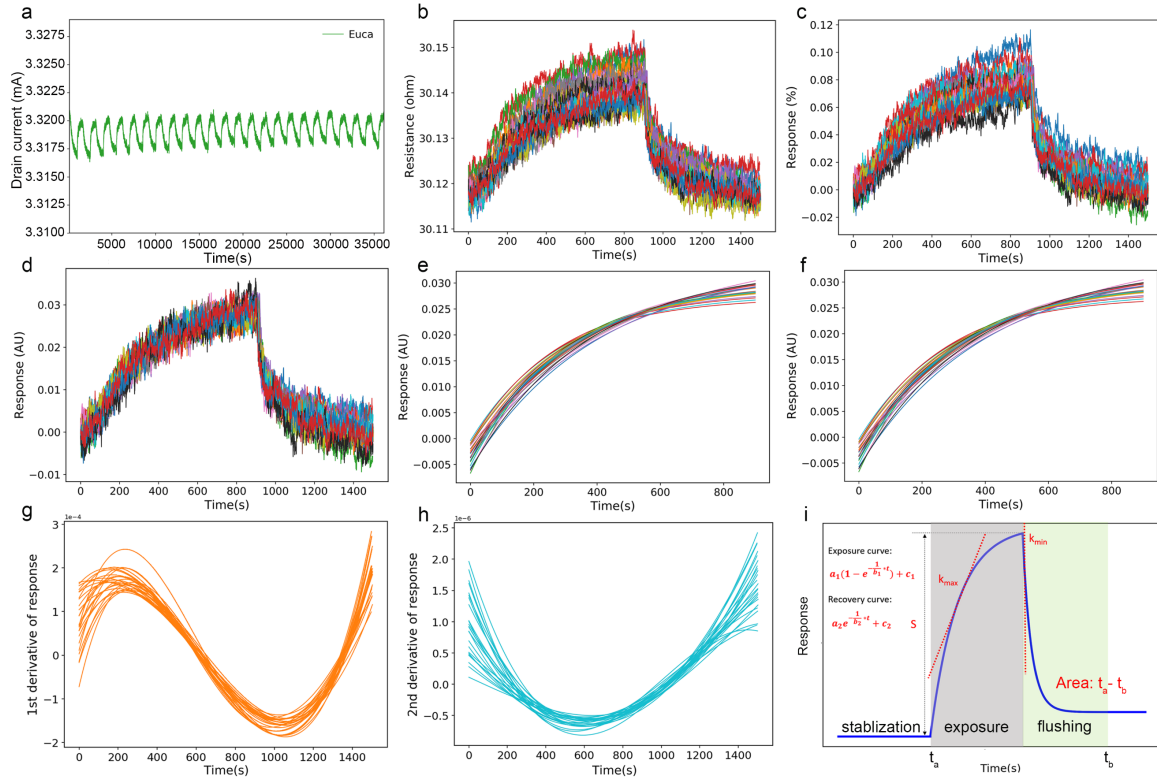
Figure 5.6 Odor sensing signal processing and feature extraction. (a) Raw digital signal of odor sensing (odor Euca as an example) consisting of 24 repetitions (a full test contains odor exposure phase and odor flushing phase). (b) Sensor resistance as a function of time after 24 repetitions split-up. (c) Sensing response as a function of time. (d) Sensing response as a function of time after data normalization. (e) Sensing response in odor exposure phase and exponential fitting. (f) Sensing response in odor flushing phase and exponential fitting. (g) First derivative of sensing response as a function of time. (h) Second derivative of sensing response as a function of time. (i) Scheme of typical sensing response and extracted features, including exponential fitting parameters ($a_1, b_1, c_1, a_2, b_2, c_2$) as well as transient parameters ($S, k_{max}, k_{min}, a_{min}, Area$).

were saved for each odor measurement. Therefore, each odor could be represented with a feature vector (24 repetitions $\times$ 11 features). The signal processing and feature extraction procedures were implemented by Python script.

5.6 Odor detection threshold results

Clinically, human olfactory function is evaluated by the combined test of odor threshold, odor discrimination, and odor identification (odor TDI test) [221]. In a similar

Table 5.2 Gas flow rate and corresponding odor concentration in individual odor exposure experiment. V_d: dilution nitrogen flow rate, unit, $sccm$. V_c :carrier nitrogen flow rate, unit, $sccm$. Note: for the demonstration of odor detection threshold, the experimental data of 2Phe under Scheme 20P, 40P, 60P, 80P, 100P were applied. For the demonstration of odor discrimination and odor identification, the experimental data of all odor under Scheme "80P" were applied.

	Individual odor exposure phase				
V_d	100	100	100	100	100
V_c	4	8	12	16	20
Scheme label	20P	40P	60P	80P	100P
	Odor concentration (ppm)				
Euca	96.154	185.186	267.858	344.828	416.667
2Nona	80.972	155.946	225.564	290.381	350.878
Euge	1.118	2.154	3.116	4.011	4.846
2Phe	4.393	8.460	12.237	15.753	19.035
(pure N_2)	/	/	/	/	/
	Individual odor flushing phase				
V_d	2000	2000	2000	2000	2000
V_c	0	0	0	0	0

fashion, the odor TDI test was applied to evaluate the performance of developed e-olfaction. In this session, odor 2Phe was employed to investigate the detection threshold of the developed e-olfaction device, whose sensing performance towards 2Phe odor at different concentrations (19.0 ppm, 15.8 ppm, 12.2 ppm, 8.5 ppm, and 4.4 ppm) was characterized, in which the flow rate information is illustrated in Table. 5.2.

Meanwhile, e-olfaction response towards reference gas (pure N_2) on the same condition was characterized as well. After signal processing and features extraction, feature vectors of 2Phe at different concentrations as well as reference gas were achieved. Principal component analysis (PCA) was employed to reduce features dimensionality and the first two principal components (PC1 vs PC2) were demonstrated as shown in Fig. 5.7. There is a significant gap existing between odor 2Phe
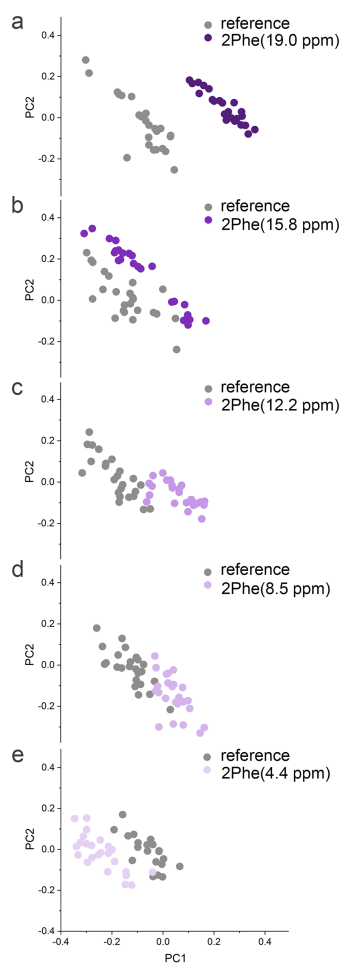
Figure 5.7 Odor detection threshold results. Odor 2Phe at decreasing concentrations are discriminated from pure N_2 (reference). (a) 19.0 ppm. (b) 15.8 ppm. (c)12.2 ppm. (d) 8.5 ppm. (e) 4.4 ppm.

cluster and reference cluster at 2Phe concentration of 19.0 ppm. With 2Phe concentration decreasing, the gap size between odor 2Phe cluster and reference cluster decreases due to the low volume of 2Phe molecules in odor 2Phe cluster, as shown in Fig. 5.7 (b) - (e). Due to the MFC flow rate range restriction in our setup, 4.4 ppm is the theoretical limit of 2Phe concentration that could be achieved. These results indicate that the developed e-olfaction could discriminate 2Phe well from the reference gas (background) and its odor detection threshold towards odor 2Phe could be down to 4.4 ppm.
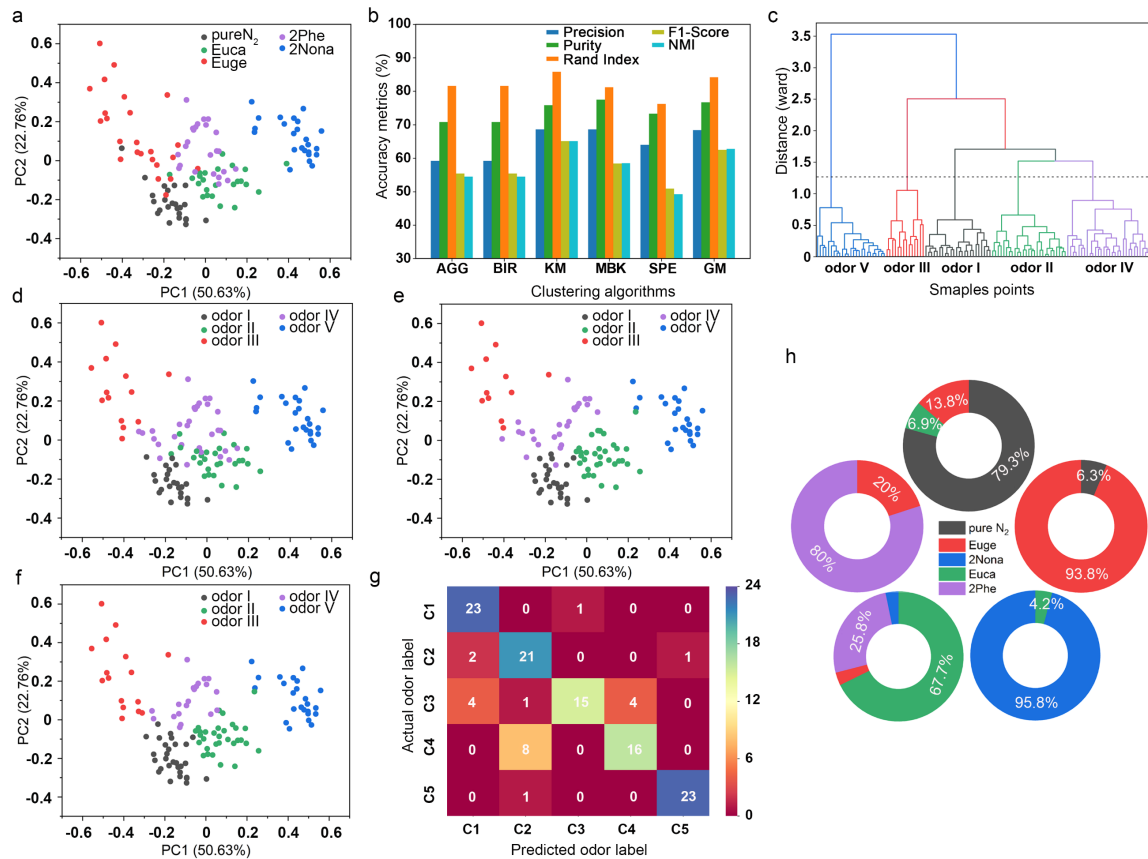
Figure 5.8 Odor discrimination performance results. (a) Odor first principal component (PC1) vs second principal component (PC2) in e-olfaction space implementing on PCA (ground truth label attached). Color code: Euca (green), Euge (red), 2Phe (purple), 2Nona (blue), and reference (gray). (b) Accuracy metrics of odor clustering implementing on various clustering algorithms. (c) Odor clusters dendrogram implementing on Agglomerative algorithms. (d) Odor PC1 vs PC2 in e-olfaction space implementing on Agglomerative algorithms (predicted label attached). (e) Odor PC1 vs PC2 in e-olfaction space implementing on Mini-Batch K-Means clustering algorithms (predicted label attached). (f) Odor PC1 vs PC2 in e-olfaction space implementing on K-Means clustering algorithms (predicted label attached). (g) Odor confusion matrix implementing on K-Means clustering algorithms. (h) Precision of odor discrimination implementing on K-Means clustering algorithms.

5.7　Odor discrimination performance results

Discrimination performance of developed e-olfaction device towards odors was evaluated, involving four odor molecules. In this part, the flow rate of both carrier gas and dilution gas remained the same for each odor sensing measurement (Table. 5.1). Following feature extraction and feature dimensionality reduction of each odor, the first two principal components of odor were plotted (PC1 vs PC2) in e-olfaction fea-

ture space. As seen in Fig. 5.8 (a), the first principal component explains 50.63% of the variance, and the second principal component explains 22.76% of the variance. Together, the first two principal components explain 73.39% of the variance. The actual label of the odor was appended and displayed in different colors, Euca (green), Euge (red), 2Phe (purple), 2Nona (blue), and reference N_2 (gray). 2Nona cluster demonstrates excellent separation from the other odor clusters, whereas 2Phe cluster, Euge cluster, and Euca cluster exhibit some overlapping.

In the absence of odor labels, odor clustering analysis based on unsupervised machine learning algorithms was investigated as well. Clustering analysis attempts to group similar samples based on a similarity measure, among which distance functions, such as Euclidean distance, are most commonly utilized. Clusters are organized in such a fashion that any two samples within the same cluster exhibit minimum distance and any two samples across different clusters exhibit maximum distance [236]. Herein, six unsupervised machine learning clustering algorithms were employed, including Agglomerative hierarchical, Birch, K-means, Mini-Batch K-Means, Spectral, and Gaussian Mixture. In light of the known number of odor species, cluster number was accordingly assigned to 5 in the analysis. To cross-validate the performance of clustering algorithms on odor discrimination, accuracy metrics were compared, for example, precision, purity, Rand Index, F1-Score, and Normalized Mutual Information (NMI). As shown in Fig. 5.8 (b), the result suggests that the K-means clustering algorithm achieves an outstanding score in terms of the above metrics.

To elucidate odor clustering results implementing on Agglomerative clustering algorithm, predicted odor clusters were illustrated in e-olfaction space. In Fig. 5.8 (d), a sample of Euca locates closer to 2Nona cluster than Euca cluster and is then merged into 2Nona cluster. Since Euge cluster is diffusive and overlaps a lot with 2Phe cluster, Euca cluster, and reference cluster, these Euge samples are therefore merged into the corresponding clusters, respectively. Likewise, samples of 2Phe drop into Euca cluster and are then combined into Euca cluster. These observations are further corroborated by the odor dendrogram shown in Fig. 5.8 (c). In this plot, 2Nona cluster exhibits the largest distance from the other odor clusters while Euge cluster approaches close to the reference cluster, Euca cluster, and 2Phe cluster. Euca cluster is positioned close to 2Phe cluster. It is also observed that Euge cluster exhibits the smallest size while 2Phe cluster exhibits the largest size.

Similarly, clustering results implementing on Mini-Batch K-Means clustering algorithm and K-means clustering algorithm were demonstrated in e-olfaction feature space, as shown in Fig. 5.8 (e)-(f). Comparing to the actual odor clusters displayed in Fig. 5.8 (a), it is found that K-means clustering algorithm exhibit better performance than Mini-Batch K-Means clustering algorithm. Odor confusion matrix implementing on K-Means clustering algorithms is shown in Fig. 5.8 (g), by which the precision (true positive divided to the all the predicted positive) metric for each odor is calculated and presented in Fig. 5.8 (h). These results reveal that odor 2Nona exhibits the highest discriminative precision at 95.8% as well as odor Euca exhibits the lowest discriminative precision at 67.7%. Incorporating K-Means clustering algorithms into the developed e-olfaction, the average discriminative precision for the odors could reach 83.3%.

5.8   Odor identification performance results

In odor discrimination session, the odor was categorized by odor feature similarity measure without odor label. The odor discrimination approach played an essential role in odor clustering analysis in the absence of odor label. In this session, in the presentence of odor labels, odor identification performance of developed e-olfaction was investigated, which was a supervised machine learning approach. Supervised machine learning utilized labeled datasets to train algorithms to classify datasets or predict outcomes for unforeseen datasets accurately [223]. Previous feature data of 5 odors (Euca, 2Nona, Euge, 2Phe, reference) as well as their odor label were processed by Linear Discriminant Analysis (LDA), which was a linear transformation technique for dimensionality reduction and well-known classifier. In contrast to PCA, LDA attempts to find a feature subspace that optimized class separability. Odor classification results by LDA are illustrated in Fig. 5.9 (a) and (b). The first three linear discriminants account for 99.45% of the total variance (LD1, LD2, LD3 explains 82.42%, 14.36%, 2.67% of the variance, respectively). These results suggest that the four odor clusters are separated very well without any overlapping. In addition to the LDA classifier, a variety of other classifiers were examined and their performances were compared in terms of 10-fold cross-validation accuracy. The results suggest that apart from AdaBoost classifier (ABC), most classifiers demonstrate excellent prediction performance with an average prediction accuracy
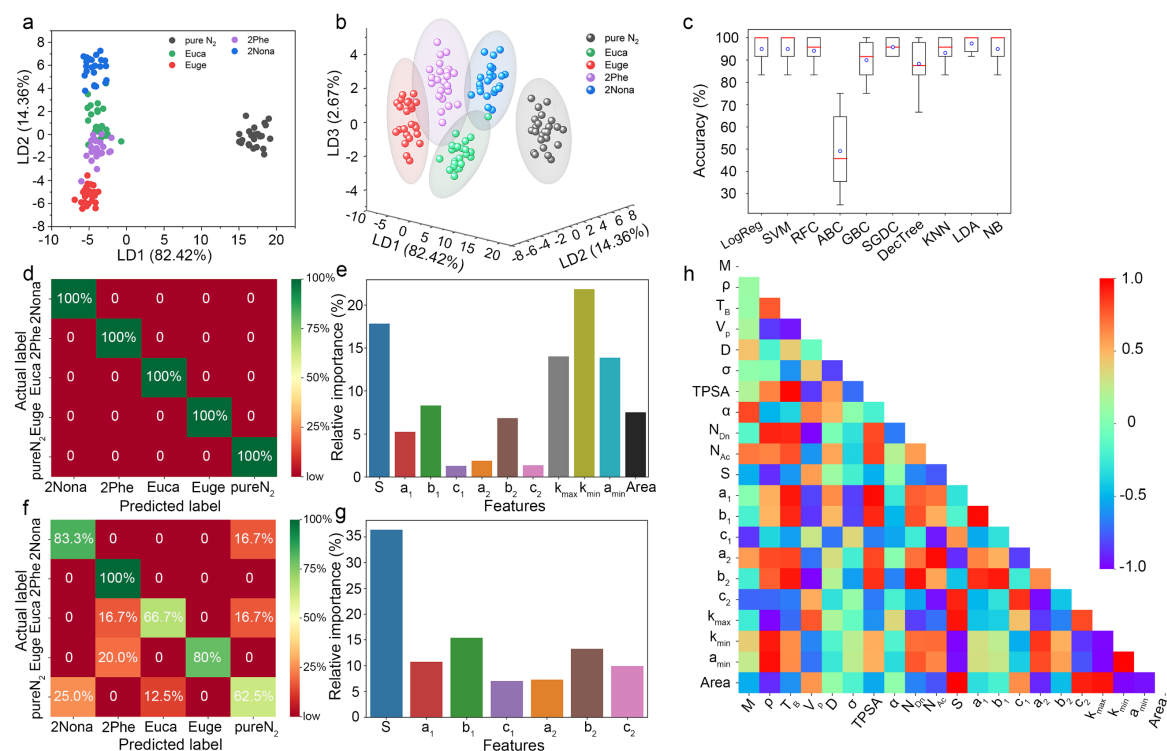
Figure 5.9 Odor identification performance and feature importance results. (a) Odor classification results by Linear Discriminant Analysis (LDA) classifier in 2D space (LD1 vs LD2) (b) Odor classification results by LDA classifier in 3D space (LD1 vs LD2 vs LD3) (c) Average prediction performance using 10-fold cross-validation on various algorithms. (d) LDA confusion matrix for the testing set using hold-out cross-validation (training set size = 75%, testing set size = 25%) based on 11 feature parameters. (e) Relative importance of 11 features on odor identification. (f) LDA confusion matrix for the testing set using hold-out cross-validation (training set size = 75%, testing set size = 25%) based on 7 feature parameters. (g) Relative importance of 7 features on odor identification. (h) Correlation between odor physicochemical parameters and odor feature parameters by e-olfaction. Note: M: molecular Weight, ρ: density, T_B: Boiling point, V_p: vapor pressure, D: dipole moment, σ: surface tension, TPSA: topological polar surface area, α: polarizability, N_{Dn}: hydrogen bond donor number, N_{Ac}: hydrogen bond acceptor number

of 80% or above. Among all the classifiers, LDA demonstrates the highest prediction accuracy of 97.5% shown in Fig. 5.9 (c).

To assess the contribution of odor feature to odor identification, the prediction performance of two groups involving in different feature parameters were examined, respectively, in which one group containing 11 feature parameters ($a_1, b_1, c_1, a_2, b_2, c_2, S, k_{max}, k_{min}, a_{min}, Area$) and the other group containing 7 feature parameters

$(a_1, b_1, c_1, a_2, b_2, c_2, S)$. LDA confusion matrix utilizing hold-out cross-validation (training dataset size = 75%, testing dataset size = 25%) for both groups were analyzed. As shown in Fig. 5.9 (d) and (f), the group containing 11 feature parameters achieve higher prediction accuracy (100%) than the group containing 7 feature parameters (76.7%), which represent that the 4 additional feature parameters ($k_{max}, k_{min}, a_{min}, Area$) play a crucial role in odor recognition. This conclusion is corroborated by the feature importance scores. In Fig. 5.9 (e), it is demonstrated that these 4 feature parameters make up 57.9% of total feature importance and single feature kmin contributes to 21.4% of total feature importance. The first 7 most important features are $k_{min}, S, a_{min}, k_{max}, Area, b_1, b_2$.

Furthermore, the correlation between the odor feature and odor physicochemical properties was explored. In particular, the correlation of the 7 most important features ($k_{min}, S, a_{min}, k_{max}, Area, b_1, b_2$) with odor physicochemical properties was analyzed. Herein, two parameters are considered to hold a strong correlation if the absolute value of their correlation coefficient is higher than 75% and moderate correlation if the absolute value of their correlation coefficient is between 55% and 75%. As the correlation map shows in Fig. 5.9 (h), odor sensing maximum response S holds a strong negative correlation with odor density and hydrogen bond acceptor amount of odor molecule. Odor feature b_1 shows a strong positive correlation with odor boiling point, topological polar surface area (TPSA), and hydrogen bond donor amount of odor molecule, as well as a strong negative correlation with odor vapor pressure and odor surface tension. Odor feature b_2 has a strong positive correlation with odor density, boiling point, TPSA, and hydrogen bond donor amount of odor molecule as well as a strong negative correlation with odor vapor pressure.

Odor feature kmax reveals a strong positive correlation with odor vapor pressure as well as a strong negative correlation with odor density, hydrogen bond donor amount of odor molecule. Odor feature kmin exhibits an intimate positive correlation with odor density and moderate positive correlation with hydrogen bond donor/acceptor amount of odor molecule. Odor feature amin demonstrates a strong positive correlation with odor density and a moderate positive correlation with hydrogen bond donor/acceptor amount of odor molecule. Odor feature Area shows a strong negative correlation with odor density and moderate negative correlation with hydrogen bond donor/acceptor amount of odor molecule. To sum up, odor density and odor hydrogen bond donor count impose an essential influence on e-

Table 5.3 Correlation between odor feature and odor physicochemical properties. Note: strong positive correlation (++), moderate positive correlation (+); strong negative correlation (–), moderate negative correlation (-).

	ρ	T_B	V_p	σ	$TPSA$	N_{Dn}	N_{Ac}
S	–						–
b_1		++	–	–	++	++	
b_2	++	++	–		++	++	
k_{max}	–		++			–	-
k_{min}	++					+	+
A_{min}	++					+	+
$area$	–					-	-

olfaction features. Besides, odor vapor pressure, odor boiling point, and TPSA exert additional influence on feature b1 and feature b2, as shown in Table. 5.3.

5.9   Electronic perception response to binary odor mixture

The sensing response of developed e-olfaction towards binary odor mixture was investigated as well, which was analogous to olfactory perception towards odor mixture in humans. Binary odor mixture with different flow rate combinations were prepared and the odor sensing response was measured in the same way as in individual odor sensing experiments. In all cases, the total flow rate of carrier gas remained constant during the odor exposure phase. Following the same protocols for data processing and feature extraction as previously described, feature data of odor mixture were then analyzed by PCA. As it is illustrated in Fig. 5.10 (a), the first 2 principal components account for more than 70% of the total variance, and the first 6 principal components account for almost 90% of the total variance. The first 2 principal components for the Euca-2Nona odor mixture and Euge-2Phe odor mixture are represented in Fig. 5.10 (b) and (c), respectively. As shown in Fig. 5.10 (b), pure 2Nona cluster is separated very well from pure Euca cluster without any overlapping. With the increasing flow rate of Euca (or decreasing flow rate of 2Nona),
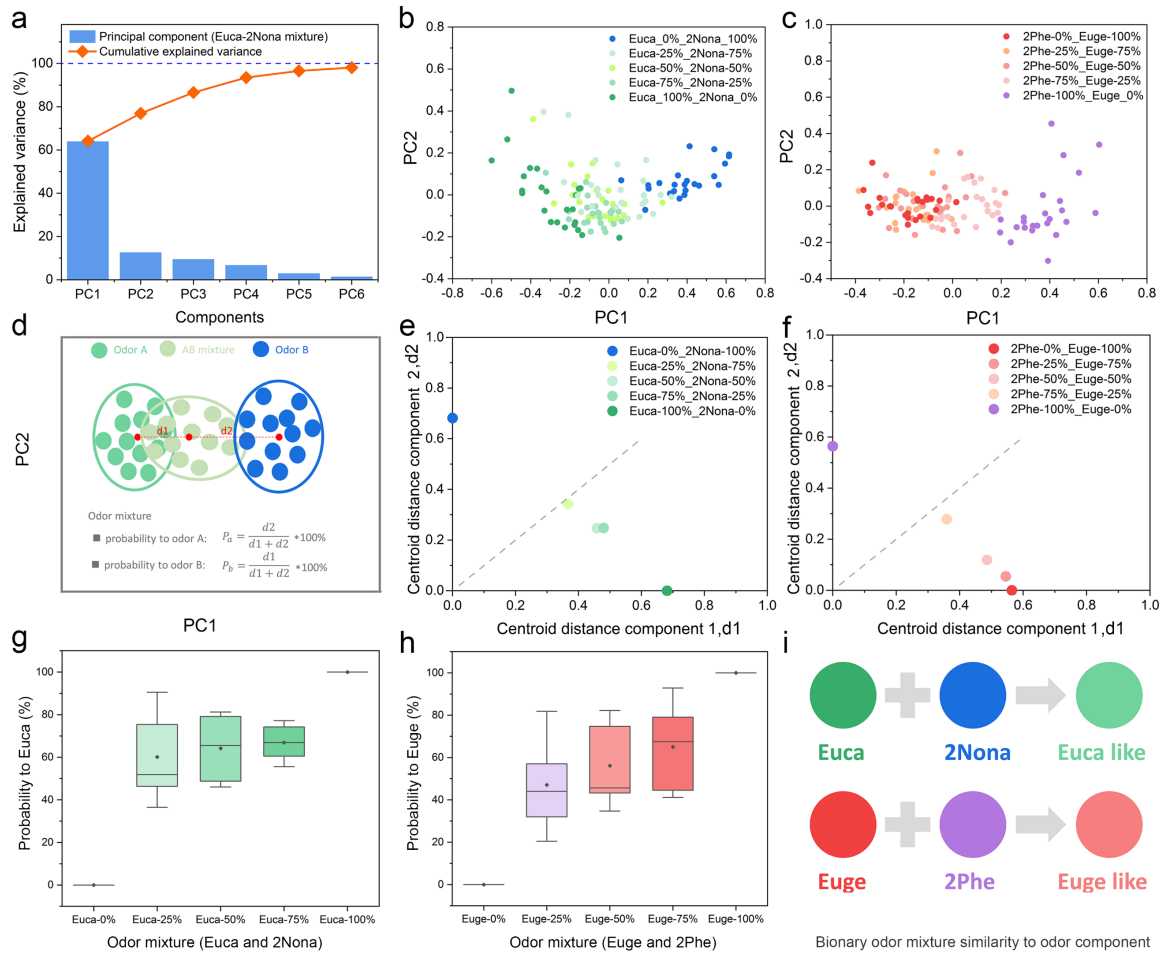
Figure 5.10 Binary odor mixture similarity to odor component results. (a) Explained variance of first 6 principal components of odor mixture features and their cumulative explained variance, odor mixture (Euca and 2Nona) as an example. (b) PCA analytical result of odor mixture (Euca and 2Nona). (c) PCA analytical result of odor mixture (Euge and 2Phe). (d) Schematic diagram of centroid distance component and similarity of odor mixture to odor component. d_1, centroid distance component 1, centroids distance of odor mixture cluster and odor component 1 cluster. d_2, centroid distance component 2, centroids distance of odor mixture cluster and odor component 2 cluster. (e) Centroid distance component (CDC) analytical result of odor mixture (Euca and 2Nona). (f) CDC analytical result of odor mixture (Euge and 2Phe). (g) Probability of odor mixture (Euca and 2Nona) to odor component Euca as a function of odor Euca ratio. (h) Probability of odor mixture (Euge and 2Phe) to odor component Euge as a function of Euge ratio. (i) Scheme of binary odor mixture similarity to odor component, odor mixture of Euca and 2Nona generats Euca similar feature, odor mixture of Euge and 2Phe generats Euge similar feature.

the odor mixture cluster tends to move toward the pure Euca cluster and vice versa. The same behavior is observed for the 2Phe and Euge mixtures, as illustrated in Fig. 5.10 (c).

Furthermore, quantitative analysis of odor mixture feature was carried out as well. The centroid points (virtual point) of individual odor clusters and odor mixture clusters were obtained at first, and distances between the centroid point of odor mixture cluster and centroid point of pure odor cluster were measured in PCA space. Consequently, each odor mixture has two distance parameters, d_1 and d_2, and they could be represented in a 2D coordination system (d_1 vs d_2), as illustrated in Fig. 5.10 (d)-(f). A statistical result based on the introduced concept "probability" is shown in Fig. 5.10 (g) and (h). These results suggest that the feature of odor mixture Euca-2Nona behave closer to odor Euca and feature of odor mixture Euge-2Phe behave more similar to odor Euge, which is well summarized in Fig. 5.10 (i).

In previous human psychophysical studies, it was reported that an odor mixture could give rise to one of the three outcomes:an elemental perception, a configural perception, an overshadowing effect [237, 238]. An elemental perception implies that both components of odor mixture are perceived in the odor mixture, whereas a configural perception infers a new odor is perceived [239]. Overshadowing refers to that there is recognition of only one odor component in a binary mixture [240]. Hence, upon processing an odor mixture, the developed e-olfaction generates features closer to one odor component in binary odor mixture, which behaves similarly to human perception of "overshadowing effect" towards binary odor mixture.

5.10   Odor perception prediction analysis

In audition and vision, the frequency of sound and wavelength of light are highly predictive of tone and color, respectively [242]. The mapping of stimulus characteristic onto human perception have been well defined, but not in olfaction. In 1968, Dravnieks envisioned that e-nose system enabled inspect samples of odorous air and report the intensity and quality of an odor without the intervention of a human nose [243]. In the past decades, a variety of e-nose systems served to detect and discriminate odors, nonetheless, few efforts have been made to go beyond that, for instance, to predict the perceptual pleasantness of odors [244].

Interestingly, it has been reported that the primary axis of human perception is odor pleasantness, and the primary axis of physicochemical properties correlate with the primary axis of olfactory perception, which allows us to predict the per-
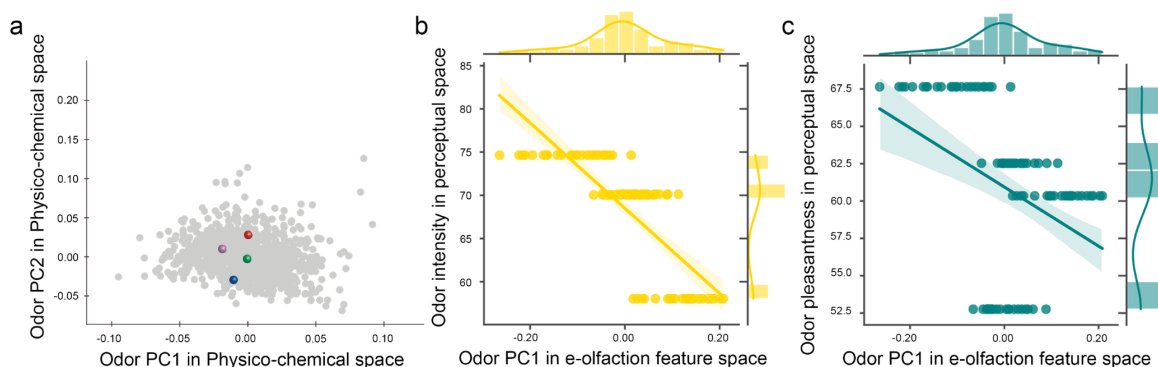
Figure 5.11 Relationship between odor perceptual pleasantness and odor PC1 in e-olfaction feature space. (a) Odor first principal component (PC1) vs second principal component (PC2) in physico-chemical space. Euca (green), 2Nona (blue), Euge (red), 2Phe (purple). (b) Correlation between odor perceptual intensity in perceptual space and odor PC1 in e-olfaction feature space. (c) Correlation between odor perceptual pleasantness and odor PC1 in e-olfaction feature space.This figure was produced and provided by my colleague Antonie Louise Bierling [241].

ceptual pleasantness of novel molecules based on their physicochemical properties alone [241, 245]. Inspired by this research work, it is reasonable to propose a hypothesis that there might be a correlation between the primary axis of olfactory perception and the primary axis of e-olfaction features. The basis is that the physicochemical features of molecules determine the odor sensing response profile generated on the developed e-olfaction system, which has been concluded from Fig. 5.9 (h). The odor sensing response profile further determines the e-olfaction features of odor. In another word, the e-olfaction features of odor could be regarded as a transformation of physicochemical properties of odor molecules. In this procedure, the e-olfaction functions as a signal transformer or signal interpreter, which is responsible for converting odor physicochemical features into odor features (such as the 11 features from e-olfaction in this work), just similar to the Fourier transform method in mathematics. The correlation between odor perceptual pleasantness/intensity in perceptual space and odor first principal (PC1) in e-olfaction feature space is demonstrated in Fig. 5.11 (a)-(c). As it implies, there might be a possibility to build a linear model to link odor perceptual pleasantness/intensity in perceptual space and odor first principal (PC1) in e-olfaction feature space. This linear model then would allow us to predict the perceptual pleasantness/intensity of novel odor molecules using the developed e-olfaction system. Nevertheless, in the current work, as it is shown in Fig. 5.11 (a)-(c), it is difficult to bring about such an accurate prediction model since only 4 odor molecules are examined. More odor molecules will be in-

Table 5.4 Simulation details in molecular dynamic simulations. A: simulation of graphene stabilization.B: simulation of dor mixture adsorption on graphene.

	Simulation I	Simulation II					
Amount		Euca-2Nona	Euca-Euge	Euca-2Phe	Euge-2Phe	Euge-2Nona	2Nona-2Phe
Graphene	1	1	1	1	1	1	1
APTS	4	4	4	4	4	4	4
water	23576	/	/	/	/	/	/
N_2	/	500	500	500	500	500	500
Euca	/	10	10	10	/	/	/
2Nona	/	10	/	/	/	10	10
Euge	/	/	10	/	10	10	/
2Phe	/	/	/	10	10	/	10
				Conditions			
Ensemble	NPT	NVT	NVT	NVT	NVT	NVT	NVT
Time(ns)	50	20	20	20	20	20	20
Size(nm)							
Graphene	4×4	4×4	4×4	4×4	4×4	4×4	4×4
Box	9×9	9×9	9×9	9×9	9×9	9×9	9×9

vestigated to derive a reliable linear model for odor perception prediction in our following project work.

5.11   Odor molecules interaction with functionalized graphene

To provide insights on the underlying mechanism of "overshadowing effect" generated on developed e-olfaction in odor mixture circumstance, the interaction between odor molecules and functionalized graphene were carried out *via* classical molecular dynamics simulation and density functional theory (DFT) calculation. Pure odor models, such as Euca, 2Nona, Euge, 2Phe, as well as odor mixture models, such as Euca-2Nona, Euge-2Phe, Euca-Euge, Euca-2Phe, Euge-2Nona, 2Nona-2Phe, were created and simulated. All models contained the same amount of odor molecules. The model configuration and simulation conditions refer to Table. 5.4.
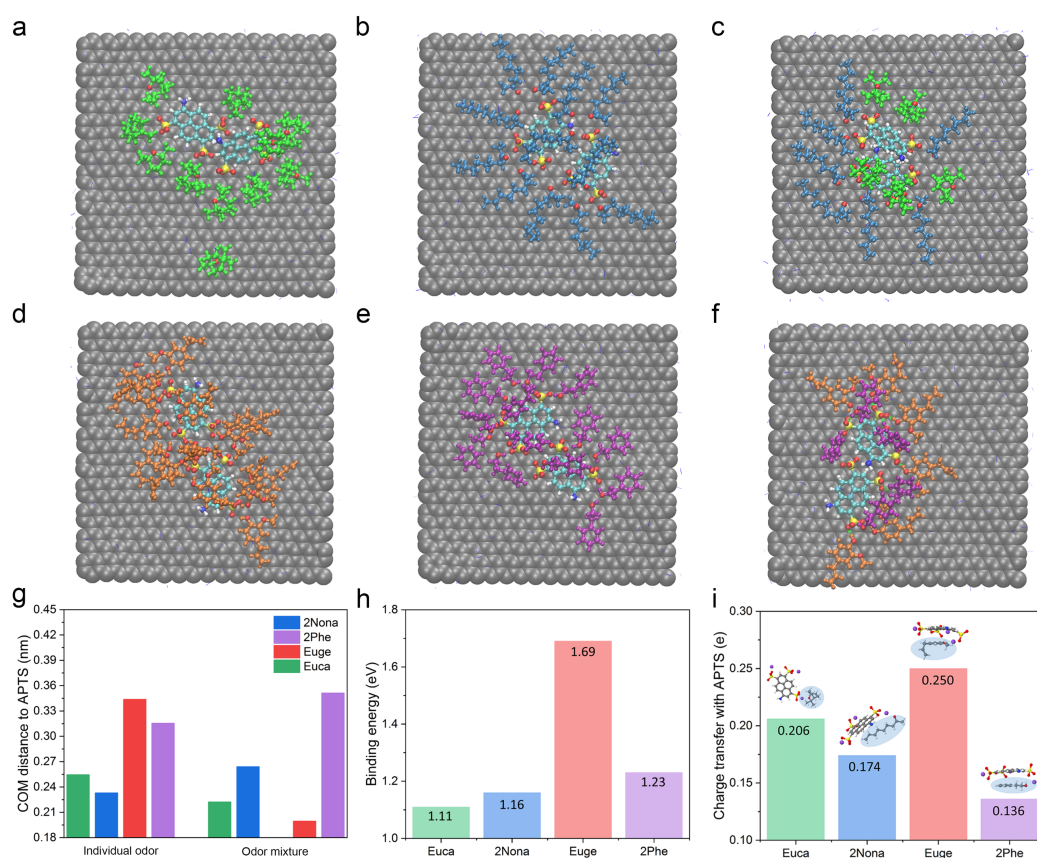
Figure 5.12 Odor molecules interaction with functionalized graphene. Simulation of odor molecules interaction with APTS molecules on graphene *via* molecular dynamic simulation. (a) Snapshot of odor molecules interaction with APTS on graphene in pure Euca odor. (b) Snapshot of odor molecules interaction with APTS on graphene in pure 2Nona odor. (c) Snapshot of odor molecules interaction with APTS on graphene in Euca-2Nona odor mixture. (d) Snapshot of odor molecules interaction with APTS on graphene in pure Euge odor. (e) Snapshot of odor molecules interaction with APTS on graphene in pure 2Phe odor. (f) Snapshot of odor molecules interaction with APTS on graphene in Euge-2Phe odor mixture. (g) Center of mass (COM) distance between odor molecules and APTS molecules. (h) Binding energy and (i) Charge transfer amount between odor molecules and APTS on graphene calculated by DFT (considering π-π stacking configuration for Euge and 2Phe molecules). Snapshot color code: graphene (gray), Euca (lime), 2Nona (blue), Euge (orange), 2Phe (purple), carbon (cyan), nitrogen (blue), sulfur (yellow), oxygen (red).

Morphology of odor molecules on graphene surface is demonstrated in Fig. 5.12 (a)-(f). The center-of-mass (COM) distance between odor molecules and APTS is measured and shown in Fig. 5.12 (g). Binding energy and charge transfer amount between odor molecules and APTS molecules are calculated by DFT and illustrated in Fig. 5.12 (h) and (i), respectively. In the individual odor case shown in Fig. 5.12 (a)-(b), odor molecules of both Euca and 2Nona favor to surround APTS. The heads of
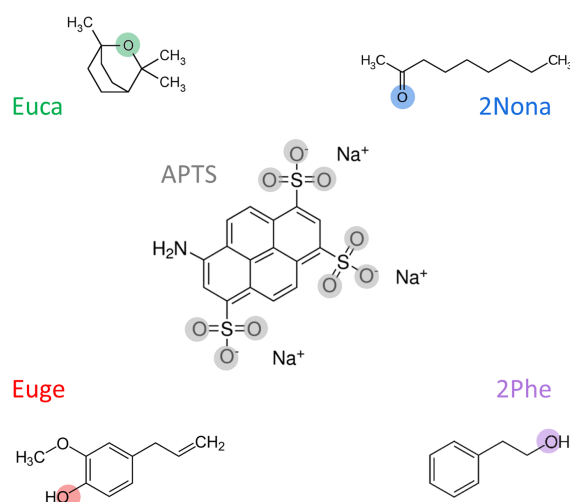
Figure 5.13 Odor molecules structure and head group definition in the molecular dynamic simulation analysis. Head of Euca marked (green), head of 2Nona (blue), head of Euge (red), head of 2Phe (purple), and head of APTS (gray).

odor molecules, which contain oxygen functional group, prefer to point into APTS, which is mainly governed by traditional dipole-dipole interaction [246]. In the odor mixture model shown in Fig. 5.12 (c), it is observed that Euca molecules approached APTS much closer than 2Nona, which was supported by the COM distance to APTS shown in Fig. 5.12 (g). Comparing the odor mixture model with the pure odor model, the COM distance to APTS of odor Euca decreases while the COM distance to APTS of 2Nona increases, which indicates competitive adsorption of Euca and 2Nona on APTS. The binding energy of Euca is a bit weaker than 2Nona, whereas Euca molecule possesses a smaller and more compact size than 2Nona, which might be more beneficial for Euca to approach APTS closely.

Odor Euge and 2Phe exhibit very similar structures, which consist of a benzene ring and oxygen-containing functional groups. In the pure odor case shown in Fig. 5.12 (d)-(e), similar to Euca and 2Nona, Euge and 2Phe molecules are found to surround APTS, too. The odor molecules' heads are found to point into the APTS head, which is mainly affected by hydrogen bonding interaction between the head of odor molecules and the head of APTS, as defined in Fig. 5.13 [247]. Hydrogen bonding interaction is believed to be stronger than conventional dipole-dipole interaction. Apart from hydrogen bonding interaction, π-π stacking interaction exists between Euge or 2Phe and APTS as well, which doesn't exist in Euca or 2Nona model. For this reason, some Euge and 2Phe molecules are observed to stack onto APTS in Fig. 5.12 (f). In the odor

mixture model, the COM distance to APTS is demonstrated and compared with the pure odor model shown in Fig. 5.12 (g). In the odor mixture model, the COM distance to APTS of Euge decreases a lot whilst the COM distance to APTS of 2Phe increases, which could be interpreted into competitive adsorption of Euge and 2Phe on APTS. This competitive adsorption is originated from different binding energy to APTS, as depicted in Fig. 5.12 (h). The binding energy of Euge is far stronger than 2Phe, leading to intimate binding between Euge and APTS. Consequently, Euge occupies more space near APTS than 2Phe. The simulation results on the other pairs of odor molecules are illustrated in Appendix A.

Odor molecules interact with APTS involving in two events: odor molecules adsorption on APTS as well as charge transfer between odor molecules and APTS, which both synergistically yield characteristic sensing response [248]. The charge transfer amount between odor molecules and APTS is displayed in Fig. 5.12 (i). Under the same circumstances, odor Euca transfers 18.4% more charge to APTS than 2Nona while Euge transfers 83.8% more charge to APTS than 2Phe. With both odor adsorption and charge transfer taken into account, the stronger odor molecules embrace more chance to approach closely to functionalized graphene and dominate the signal characteristic in the odor mixture, which subsequently covers the signal of the other odor. To sum up, owing to the difference in binding energy and capability of charge transfer, the developed e-olfaction generated a "shadowing effect" towards processing binary odor mixture, which explains and supports the observed experimental results.

5.12   Summary

In the present study, the odor identification performance of developed biomimetic electronic olfaction is successfully demonstrated. The developed e-olfaction system comprises a single channel nanosensor rather than a sensor array in conventional e-nose system and operates at room temperature, which shows great potential to develop into a miniaturized, portable, and implantable device. Instead of traditional thermodynamical feature, kinetically transient-state features were extracted from odor sensing response profile, which made the best use of characteristic response profile of odor sensing. Noncovalently functionalized graphene was applied as sensing element materials and imposed the devices merits of selective adsorption and

ultrahigh sensitivity. Similar to human olfaction, the developed e-olfaction exhibited excellent performance in olfactory assessment, including odor detection threshold, odor discrimination and odor identification. Four odors were employed to implement the olfactory evaluation test, including Euca, 2Nona, Euge, 2Phe, which are typically employed in olfactory training for patients suffering from olfactory disorder. The developed e-olfaction demonstrated ultralow odor threshold towards odor 2Phe (4.4 ppm in the current lab condition) as well as excellent discrimination performance (83.3%). Most importantly, incorporating with machine learning classifier algorithm (LDA), the developed e-olfaction achieved ultrahigh odor identification accuracy (97.5%). Simultaneously, the e-olfaction manifested efficient processing capability towards binary odor mixture. The e-olfaction feature of binary odor mixture was shown to behave close to one odor component while the feature of the other odor was partially covered, which was analogous to the "overshadowing effect" in human perception upon processing binary odor mixture. Classic molecular simulation as well as density function theory calculation was implemented to shed light upon the underlying mechanism. The results suggest that, owning to the distinct capability of odor in terms of binding energy and charge transfer, competitive adsorption upon sensing elemental materials occurs between two odor components in odor mixture.

Chapter 6

Gases discrimination between PH$_3$ and NH$_3$

In the previous chapter, we have demonstrated the feasibility to discriminate different odors using graphene-based gas sensor in combination with machine learning algorithms. In this chapter, we would like to extend this strategy into more real practical application, such as industrial gases discrimination. We have phosphine (PH$_3$) and ammonia (NH$_3$) gases as an example and verify the potential to discriminate these gases. Moreover, the adsorption behavior of analyte gases on graphene surface will be investigated *via* molecular dynamics simulation. This work has been accepted and published online by Advanced Intelligent Systems since 19th, March, 2022 (DOI:10.1002/aisy.202200016).

6.1 Motivation

Ammonia (NH$_3$) and phosphine (PH$_3$) are both common inorganic compounds widely used in many industrial processes, while exposure to even low concentrations of them adversely affects human health, as introduced in chapter 1. Consequently, the development of highly sensitive, reliable, and efficient gas sensors to monitor NH$_3$ and PH$_3$ gas concentrations in an industrial environment is of the utmost importance. Over the past decades, a variety of gas sensors have been developed for both NH$_3$ and PH$_3$ detection, respectively [249, 250]. In spite of remarkable progress of the sensors, there are still some limitations. On one hand, for most of commercial gas sensors, a high operating temperature is required [218]. On the other hand, the
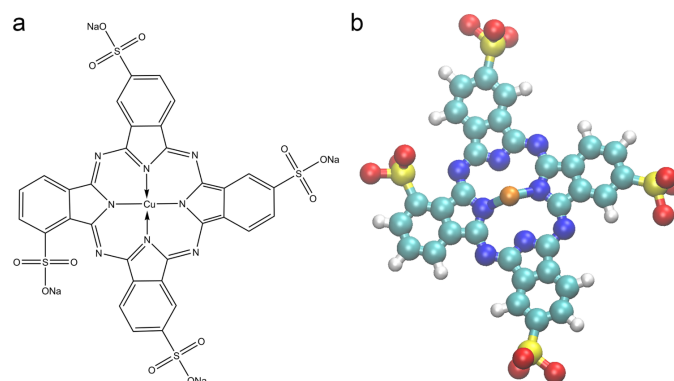
Figure 6.1 Schematic of CuPc molecule. (a) Chemical structure of CuPc, molecular formula, C$_{32}$H$_{12}$CuN$_8$O$_{12}$S$_4$Na$_4$. (b) CuPc molecule ball-and-stick model.

gas sensor is usually dedicated to one gas detection task under a pre-specified condition. For instance, in order to monitor the NH$_3$ gas in an industrial environment, a specific gas sensor dedicated to NH$_3$ detection has to be used; to monitor the PH$_3$ gas in the same work place, another specific gas sensor dedicated to PH$_3$ detection is required. To the best of our knowledge, very few gas sensors with the capability to discriminate or identify multiple industrial gases in the same environment have been demonstrated.

In this work, an ultrasensitive, highly discriminative, graphene nanosensor for the detection and identification of ammonia and phosphine at room temperature is demonstrated. Graphene, exfoliated and functionalized by a copper phthalocyanine derivate (CuPc), was employed as sensing material in chemiresistive formats. Multiple features were extracted from the characteristic sensing response-profile for each analyte gas and then applied to represent the gas. In combination with efficient machine learning techniques, our graphene nanosensor demonstrates excellent gas identification performance when exposed to ultralow gas-concentrations (from 100 ppb to 1 ppm). Molecular dynamics simulations were carried out to investigate the sensing mechanism in terms of the interaction between the functionalized graphene and the analyte gases.

Table 6.1 Simulation details in molecular dynamic simulations.

	Simulation I c	Simulation II: analyte gas adsorption	
Molecules	graphene stabilization	case: 100-NH$_3$	case: 100-PH$_3$
Graphene	1	1	1
CuPc	4	4	4
water	23523	/	/
N$_2$	/	400	400
NH$_3$	/	100	/
PH$_3$	/	/	100
Conditions			
Ensemble	NPT	NVT	NVT
Time(ns)	100	5	5
Size(nm^2)			
Graphene	4×4	4×4	4×4
Box	9×9	9×9	9×9

6.2   Graphene dispersion preparation

The specific product information of chemicals involved in this work, such as graphite powder, CuPc, are listed in Table. 2.1 in chapter 2. The chemical structure of CuPc is illustrated in Fig. 6.1. The protocol of graphene preparation refers to the graphene preparation section in chapter 2.

6.3   Modelling

In this work, molecular dynamic simulation tool was employed to investigate the adsorption behavior of analyte gases on graphene surface. The simulation was implemented on GROMACS 5.1.2 platform with GROMOS 54a7 force field [115]. The forcefield parameters of all molecules (except Cu atom) were generated on the Automated Topology Builder (ATB) and Repository Version 3.0 platform [225]. The force-

field parameters of centrally coordinated Cu atom in CuPc molecule was referred to previous work [251]. The simulation work consisted of two steps, the first step was the stabilization of CuPc functionalized graphene in water aqueous condition while the second step was to examine the interaction between analyte gas molecules and functionalized graphene by CuPc molecules. In the first part, the simulation box contained a graphene flake (4 nm × 4 nm, 680 atoms), 4 CuPc molecules and water molecules. Reaching the equilibrium state, CuPc molecules were attached on graphene surface *via* π-π stacking [125]. In the second part, the graphene flake functionalized by CuPc molecules from the previous box were introduced into a new simulation box. In addition, analyte gas (NH$_3$ or PH$_3$) molecules and nitrogen gas were present in the simulation system. The modelling parameters refer to chapter 3. Model configuration details are shown in Table. 6.1.

6.4 Discrimination performance results

The schematic illustration of the graphene nanosensor development-workflow is shown in Fig. 6.2. Following that, graphene flakes are deposited on interdigital electrodes (IDE) by dielectrophoretic alignment under an alternating current (AC). Upon exposure to analyte gas in the gas sensing measurement system (as shown in Fig. 6.3), the resistance of the sensor device shifts owing to the exchange of charge carriers between the analyte gas and the sensing material. This shifting is dependent on the course of the analyte gas exposure and analyte gas flushing and is reflected by the measured current evolution. Features are extracted from the characteristic sensing response profile, which are then employed to represent the analyte gas. Finally, these feature data are processed by machine learning classifier algorithms and the identification performance of each analyte gas are demonstrated.

In order to assess the quality of the prepared graphene and to validate the coupling of CuPc to the graphene surface, both Raman spectrum characterization and UV-vis absorption characterization were carried out, as shown in Fig. 6.4 (a) and (b). Fig. 6.4 (a) presents the Raman spectra of both graphite and the prepared graphene (Gra-CuPc). In the Raman spectra of graphite, three dominant peaks are found at wavenumbers of around 1340 cm^{-1}, 1570 cm^{-1}, 2680 cm^{-1}, corresponding to the D, G and 2D graphitic bands. The D band represents either defects or edges in the
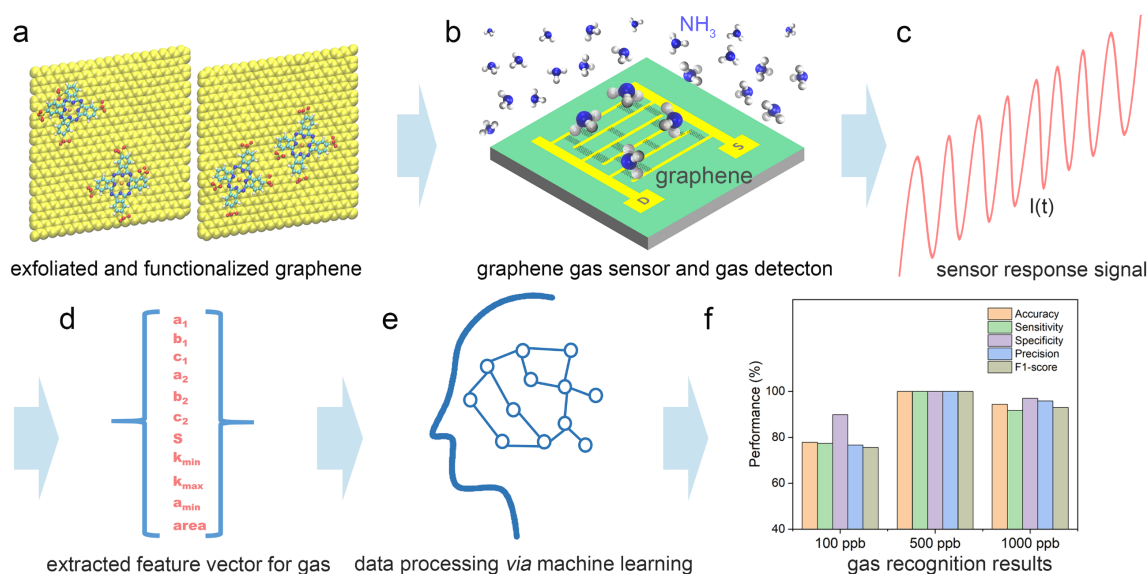
Figure 6.2 Schematic of graphene nanosensor development workflow. (a) Schematics of graphene exfoliated and modified by CuPc. (b) Graphene working as sensing elements in gas sensor and interacting with analyte molecules (e.g., NH$_3$). (c) Time-dependent current profile of graphene nanosensor upon exposure to analyte gas. (d) Feature vectors representing analyte gas extracted from sensing response profile. (e) Feature data processing *via* supervised machine learning classifier algorithms. (f) Sensor performance evaluation and classification results displaying.

lattice, and the G band represents sp^2-hybridized carbon bonds in graphene and graphite, while the 2D band indicates the layer number of graphene [166]. In the Raman spectra of Gra-CuPc, the D, G, 2D bands are located at wavenumbers 1340 cm^{-1}, 1585 cm^{-1}, 2700 cm^{-1}, which exhibits redshifts by 15 cm^{-1} and 20 cm^{-1} in G and 2D bands in comparison with graphite spectra. This significant redshift of the G band and 2D band for Gra-CuPc are the evidence of the strong coupling as well as charge transfer between the CuPc and graphene [252, 253].

In addition to the observation of the characteristic bands of graphite, an extra band at wavenumber of 1534 cm^{-1} is observed, which is attributed to isoindole ring stretching, pyrrole stretching as well as displacement of the C-N-C bridge bond related to the central copper ion of CuPc molecule [254]. This observation further confirms the successful functionalization of CuPc on graphene. The observation of D band in the Raman spectra of Gra-CuPc implies the presence of edge defects in the graphene flakes caused by probe-type ultra-sonication exfoliation [136].The basal planes of the graphene flakes are not heavily damaged as supported by the small intensity ratio of the D to G peaks (I_D/I_G = 0.50), which is much lower than that of
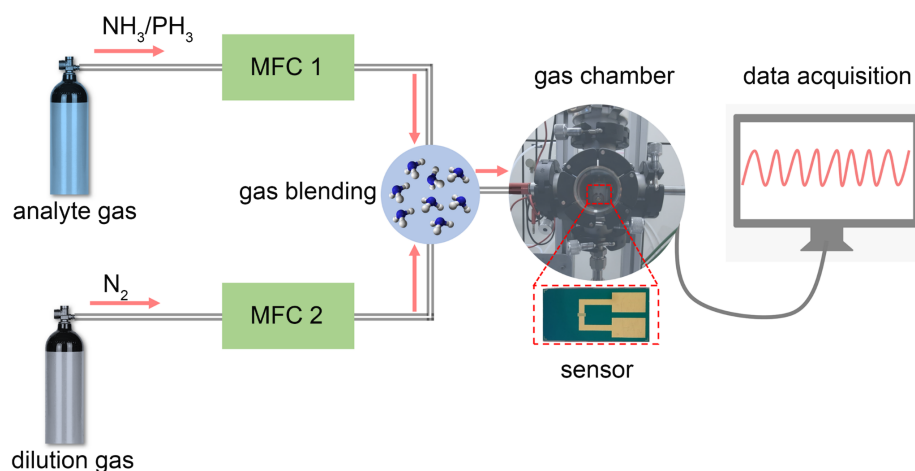
Figure 6.3 Schematic of gas sensing platform. Gas sensing platform consists of four parts, gas delivering system, gas exposure chamber, signal acquisition system and signal display system.

chemically modified graphene oxide (I_D/I_G > 1.0). The intensity ratio of the 2D band to the G band (I_{2D}/I_G = 0.52) suggests the existence of multi-layer graphene in our prepared Gra-CuPc samples [170].

Fig. 6.4 (b) presents the UV-vis spectra of both CuPc and the prepared Gra-CuPc dispersion. In the UV-vis spectra of CuPc, the typical Q band of phthalocyanine derivatives in the wavelength region between 500 nm and 750 nm are noticed, which consists of two bands, the prominent peak at 629 nm and the satellite shoulder at 663 nm, corresponding to the presence of a dimer and a monomer of CuPc, respectively [255, 256]. Very little absorption is noticed at higher wavelengths (> 750 nm). As shown in the inset in Fig. 6.4 (b), CuPc aqueous (right tube) solution exhibits a dark blue color while Graphene-CuPc displays a gray color. In the UV-vis spectra of Gra-CuPc, the presence of such bands is still apparent even after implementing high-speed centrifugation that is intended to remove excess CuPc molecules, confirming the existence of CuPc molecules in the Gra-CuPc dispersion. Nevertheless, significant absorption is seen for wavelengths above 750 nm, agreeing well with the presence of graphene flakes in Gra-CuPc dispersion [257]. Fig. 6.4 (c) and (d) show the morphology images of Gra-CuPc flakes deposited on our sensor devices. Graphene flakes are found mostly aggregated on the gaps while few flakes are left on the gold electrodes even after DI water flushing. The graphene flake size is several hundred nanometers, which is far smaller than the gap width (around 4 μm) and several graphene flakes are observed to stack on each other to connect the adjacent elec-
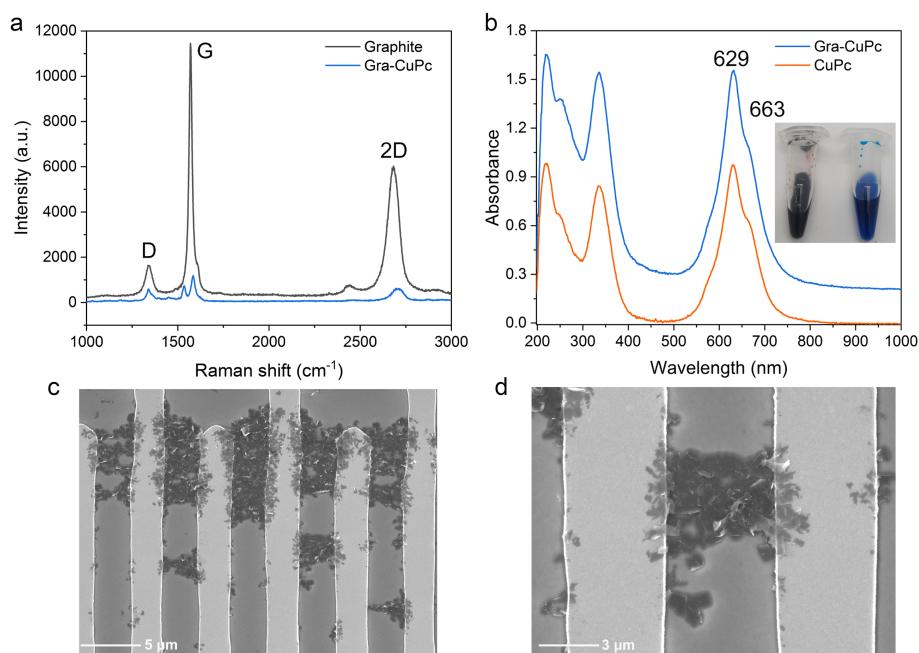
Figure 6.4 Characterization results of graphene functionalized by CuPc (Gra-CuPc). (a) Raman spectrum characterization of Gra-CuPc. (b) UV-vis absorption spectra characterization of pure CuPc aqueous solution and Gra-CuPc dispersion. Inset figure, Gra-CuPc dispersion sample (left tube) and pure CuPc dispersion sample (right tube). (c) and (d) Scanning Electron Microscope (SEM) characterization of Gra-CuPc flakes deposited on gas sensor.

trodes electrically. Tuning the DEP parameters, the morphology of graphene flakes deposition can be further optimized [258].

Following the sensing measurement, the time-dependent currents upon exposure to NH_3 and PH_3 at different concentrations were converted into time-dependent response signals. The response profiles for each analyte gas and for each concentration consists of 24 reproduced tests, as shown in Fig. 6.5 (a). Each individual test contains two phases, the analyte gas exposure phase (15 mins) and analyte gas flushing phase (10 mins). In order to standardize the sampling process and the cleaning process and to avoid any intervention by the operator, the whole sensing measurement was automated by a set of VB script. As it is depicted in Fig. 6.5 (a), upon exposure to the 100 ppb analyte gas, the average response magnitude of NH_3 is 92% higher than that of PH_3 while the response magnitude of PH_3 is close to that of reference gas (pure N_2). This suggests that, at the 100 ppb concentration, the interaction between NH_3 and functionalized graphene is stronger than the interaction between PH_3 and functionalized graphene, while the interaction between PH_3
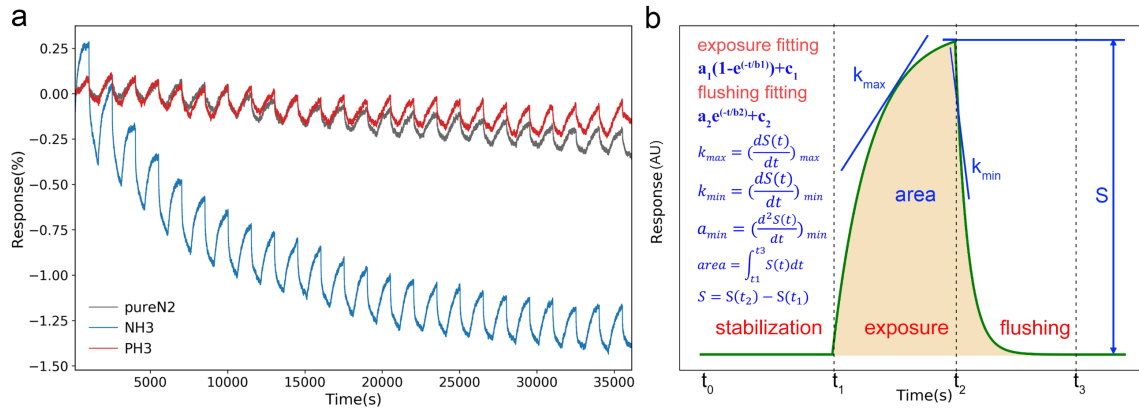
Figure 6.5 Sensing signals and extracted features. (a) Typical response profile of graphene gas sensor towards 100 ppb analyte gas (NH$_3$, PH$_3$, and reference gas N$_2$) under cycling exposure testing. A complete test is composed of 24 repetitions test. (b) Schematic of sensing response profile S(t) for single cycle test, consisting of analyte exposure phase ($t_1 - t_2$, 15 min in this work) and analyte flushing phase ($t_2 - t_3$, 10 min in this work). Before initial cycle, a stabilization process ($t_0 - t_1$) is performed under pure N$_2$ flow to reach a baseline. The feature vector representing each analyte gas consists of 11 parameters, including, $a_1, b_1, c_1, a_2, b_2, c_2, S, k_{max}, k_{min}, a_{min}, area$.

and functionalized graphene is quite weak. It is also noticed that there is a larger drift in the NH$_3$ response profile than in the PH$_3$ response. This behavior is most prominent at the initial repetitions of the sensing measurements, which may be explained by the fact that, for the NH$_3$ analyte gas, there are still some NH$_3$ residues on the functionalized graphene surface even after the last flushing [176]. For the PH$_3$ analyte gas, the analyte flushing time is suitable for a full recovery due to low amount of PH$_3$ adsorbed on the sensor surface and the weak bonding between PH$_3$ and functionalized graphene, as discovered similarly in previous work [111].

To obtain feature data for each gas, the response profiles were further processed, as demonstrated in Fig. 6.5 (b). In order to efficiently discriminate the analyte gases, multiple features were extracted from the response profile for each analyte gas instead of using only the response magnitude. A total number of 11 transient parameters were obtained from each individual response profile. Both response profiles in analyte gas exposure phase ($t_1 - t_2$) and analyte gas flushing phase ($t_2 - t_3$) are fitted by an exponential function, by which 3 coefficients (a_1, b_1, c_1) for analyte gas exposure fitting curve and 3 coefficients (a_2, b_2, c_2) for analyte gas flushing were found, respectively. Furthermore, calculations of the first derivative and the second derivative of the response profile as a function of time were conducted,
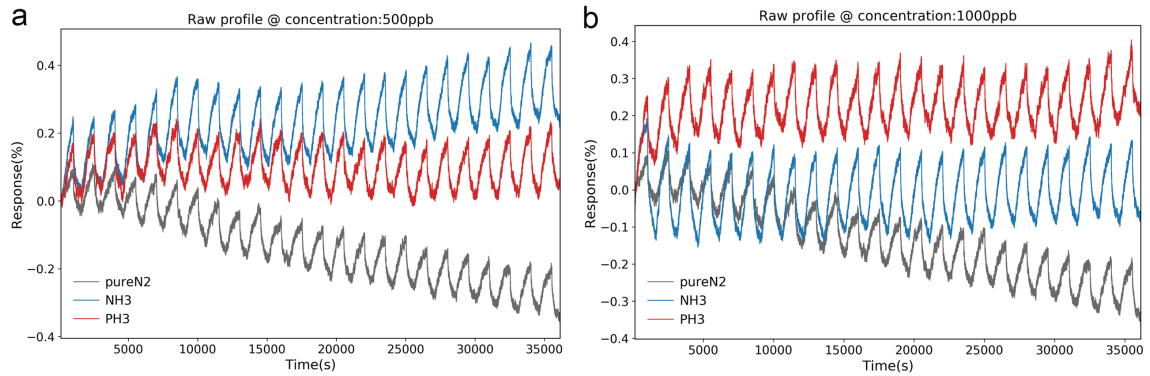
Figure 6.6 Response profile of graphene gas sensor towards (a) 500 ppb (b) 1000 ppb analyte gas (NH_3, PH_3, and reference gas N_2) under cycling exposure testing.

by which both the maximum value (k_{max}) and the minimum value (k_{min}) of the first derivative of the response profile were acquired, as well as the minimum value (a_{min}) of the second derivative of the response profile was determined, respectively. Besides, the transient response S in the whole exposure phase ($t_1 - t_2$) was calculated, as well as the area under the whole response profile ($t_1 - t_3$) was integrated. Therefore, each analyte gas is represented by a feature vector, which consists of 24 arrays of 11 features. All these parameters were acquired using a Python script. Sensing response towards higher analyte concentrations are displayed in Fig. 6.6.

In this work, feature vectors of both NH_3 and PH_3 at different concentrations (100 ppb, 500 ppb, and 1000 ppb) were characterized by the developed gas sensor. Feature vectors of pure N_2 were determined as a reference, too. All these data were then analyzed employing unsupervised machine learning (Principal Component Analysis, PCA) as well as supervised machine learning (e.g., Linear discriminant analysis, LDA), as shown in Fig. 6.7. Specifically, PCA is a non-parametric statistical technique primarily utilized for dimensionality reduction or compression of a high-dimensional dataset onto a lower-dimensional feature subspace with the aim of maintaining most of the relevant information [259]. The PCA score plots of all data are presented in Fig. 6.7 (a) and (b). The first principal component explains 49.1% of the variance, while the second and third principal components explain 24.7% and 11.0% respectively. Together, the first three principal components explain 84.8% of the variance. As it can be seen in the 2D plot, NH_3 clusters are located on the left side, PH_3 clusters are located on the middle, and reference gas cluster is located on the right side. Obviously, PH_3 clusters are close to reference gas cluster, especially at
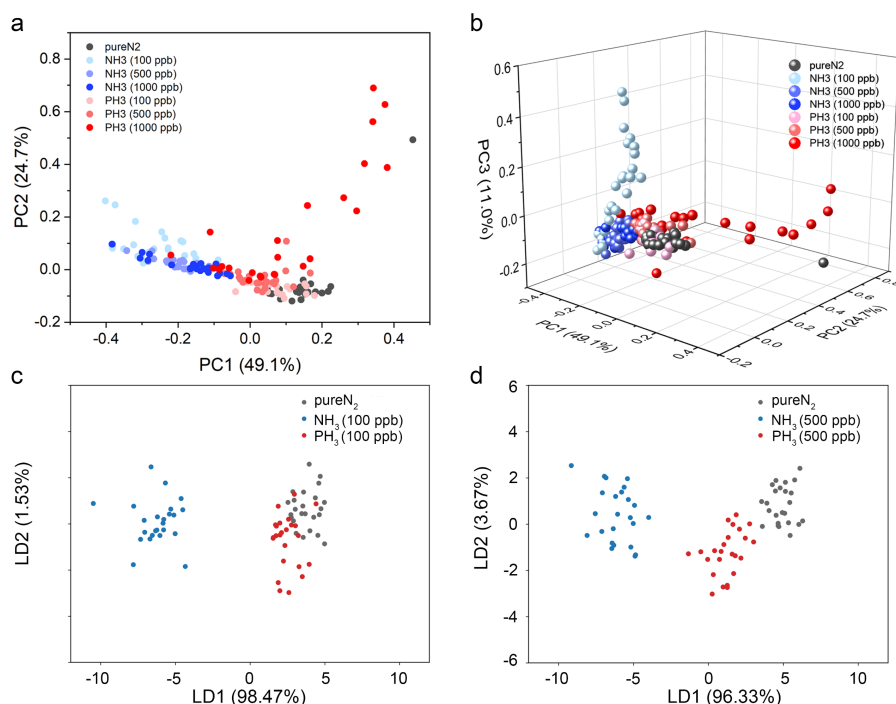
Figure 6.7 PCA score plot for both NH_3 and PH_3 analyte gas at different concentration. (a) 2D space plot. (b) 3D space plot. (c) Linear discriminant analysis (LDA) score plot for both NH_3 and PH_3 analyte gas at 100 ppb concentration. (d) LDA score plot for both NH_3 and PH_3 analyte gas at 500 ppb concentration.

100 ppb, while NH_3 clusters are far away from the reference gas cluster, suggesting that NH_3 induces a more discriminative signal than PH_3 upon interacting with functionalized graphene on the sensor. At low concentration (100 ppb), the PH_3 cluster exhibits some overlapping with reference gas cluster, indicating that the effective response between PH_3 and functionalized graphene is extremely weak at low concentration. With increasing PH_3 concentration, the distance between PH_3 cluster and reference cluster increases as well, suggesting an enhanced signal response at higher concentration. Utilizing supervised machining learning techniques, the classification results of both NH_3 and PH_3 from the reference gas (pure N_2) were achieved, for instance, using the LDA classifier, as depicted in Fig. 6.7 (c) and (d). In contrast to the PCA algorithm, the LDA algorithm attempts to find a feature subspace that optimizes class separability [260]. As it is observed, at 100 ppb concentration, NH_3 forms an isolated cluster while PH_3 cluster exhibits some overlapping with reference gas cluster. At 500 ppb concentration, the three clusters separate from each other well, which suggests a perfect classification among these three analyte gases.
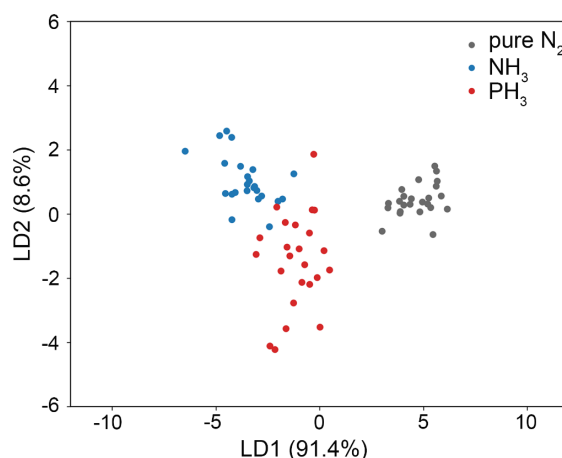
Figure 6.8 LDA score plot for both NH_3 and PH_3 analyte gas at 1000 ppb concentration.

The LDA classification results are consistent with the PCA results. LDA classification results on 1000 ppb refers to Fig. 6.8.

To evaluate the classification performance of the developed gas sensor, several critical metrics for each analyte gas were evaluated. A hold-out cross-validation approach was employed to calculate the confusion matrix, by which 70% of the feature data was utilized to train the LDA classifier algorithm and 30% of the feature data was then applied to validate the trained classifier. The confusion matrix results for 100 ppb analyte gas are shown in Fig. 6.9 (a). NH_3 has a good classification result while PH_3 achieves moderate classification results due to its signal overlapping with reference gas. With the confusion matrix results, the performance metrics, including accuracy, sensitivity, specificity, precision and F1-score were determined for each analyte gas, as shown in Fig. 6.9 (b).

In terms of these above metrics, the developed gas sensor exhibits an excellent classification performance for NH_3 (accuracy- 100.0%, sensitivity-100.0%, specificity-100.0%) while the performance is moderate for PH_3 (accuracy- 77.8%, sensitivity-75%, specificity-78.6%) due to some confusion with reference gas. Furthermore, the sensor's overall classification accuracy with respect to different classifier algorithms were compared as well, in which the k-fold cross-validation (k=10) approach was employed [261]. As presented in Fig. 6.9 (c), the overall classification accuracies achieved by most classifier algorithms are above 80%. Likewise, the sensor's performance towards 500 ppb and 1000 ppb are demonstrated in Fig. 6.9 (d)-(f) and Fig. 6.9 (g)-(i), respectively. The sensor presents an excellent classification perfor-
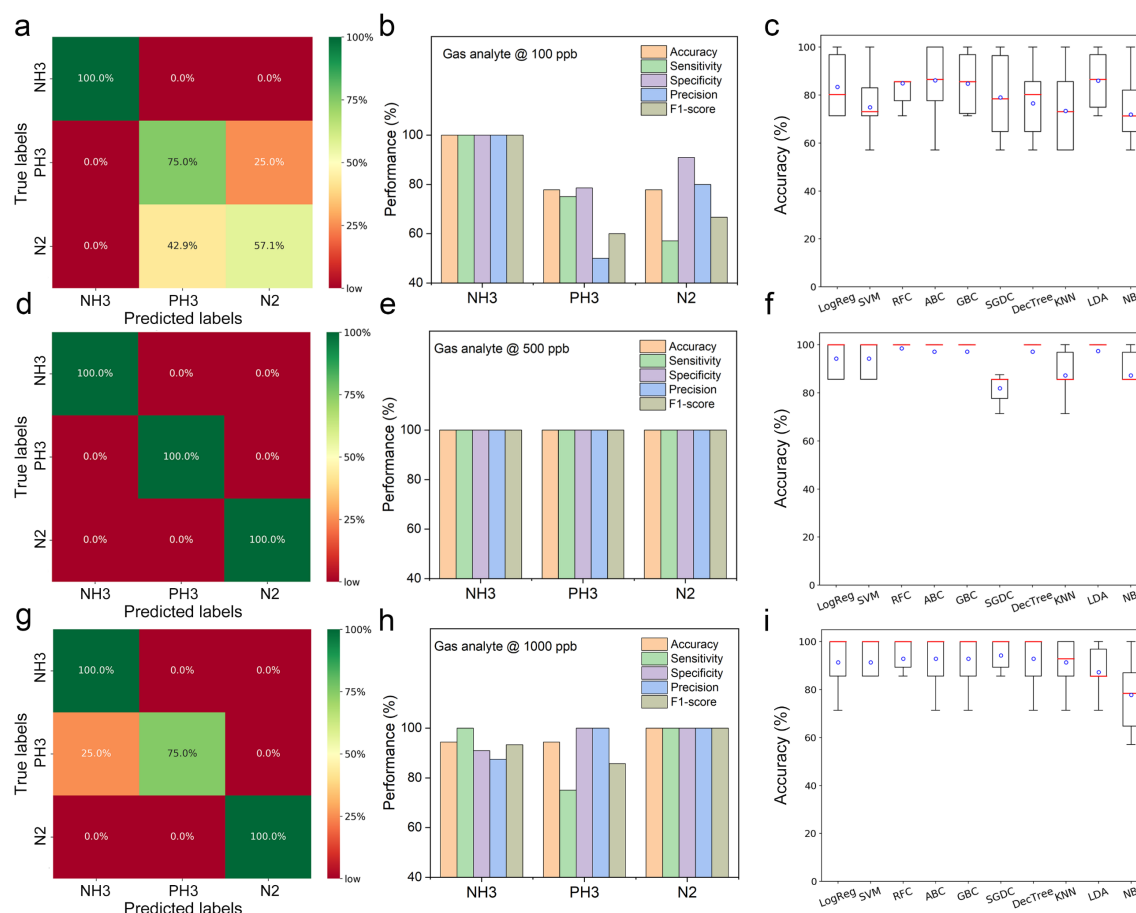
Figure 6.9 Discrimination results at different concentrations. (a) Confusion matrix of analyte gas classification using LDA classifier algorithm at 100 ppb concentration. (b) Sensor performance metrics towards NH$_3$, PH$_3$ and N$_2$ at 100 ppb concentration using hold-out cross-validation method. (c) Sensor classification accuracy relationship with classifier algorithms at 100 ppb concentration using k-fold cross-validation method. (d) Confusion matrix of analyte gas classification using LDA classifier algorithm at 500 ppb concentration. (e) Sensor performance metrics towards NH$_3$, PH$_3$ and N$_2$ at 500 ppb concentration using hold-out cross-validation method. (f) Sensor classification accuracy relationship with classifier algorithms at 500 ppb concentration using k-fold cross-validation method. (g) Confusion matrix of analyte gas classification using LDA classifier algorithm at 1000 ppb concentration. (h) Sensor performance metrics towards NH$_3$, PH$_3$ and N$_2$ at 1000 ppb concentration using hold-out cross-validation method. (i) Sensor classification accuracy relationship with classifier algorithms at 1000 ppb concentration using k-fold cross-validation method.

mance for 500 ppb analyte gas. For 1000 ppb, a good classification performance is achieved for both NH$_3$ (accuracy- 94.4%, sensitivity-100%, specificity-90.9%) and PH$_3$ (accuracy- 94.4%, sensitivity-75%, specificity-100.0%). For 500 ppb and 1000 ppb analyte gas, the overall classification accuracy achieved by most classifier algorithms
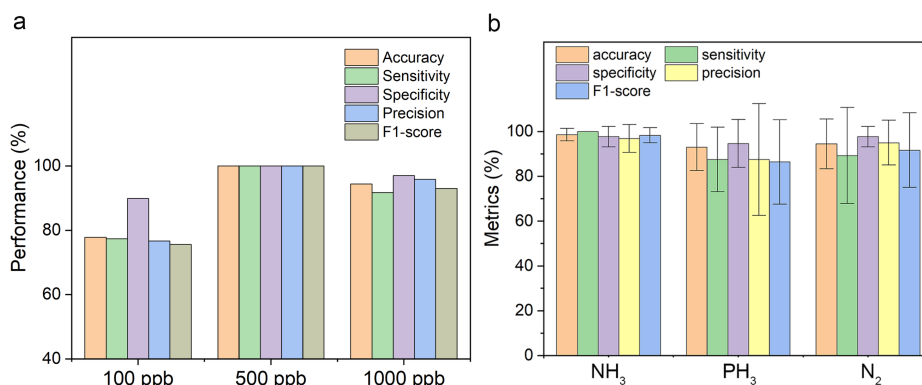
Figure 6.10 Overall sensing performance results. (a) Overall performance of developed gas sensor towards NH_3, PH_3 and N_2 at different concentration. (b)Performance of developed gas sensor towards individual gas.

remains higher than 80%, as illustrated in Fig. 6.9 (f) and (i). The overall sensor performance is summarized in Fig. 6.10, which demonstrates the excellent classification performance of developed gas sensor towards both NH_3 and PH_3.

6.5   Potential mechanism to the discriminated features

As previously displayed in the PCA score plot, the NH_3 cluster is located far away from the reference gas cluster while the PH_3 cluster is located close to the reference gas cluster. To provide some insight into the fundamental sensing mechanism, a molecular dynamics simulation was carried out to investigate the interaction between analyte molecules and functionalized graphene. Two cases, the NH_3 case and the PH_3 case, were created and modeled on the same condition. The distribution of the molecules at the initial state and after reaching equilibrium for both gases is presented in Fig. 6.11 (a)-(b) and (c)-(d), respectively. In the initial state, analyte molecules are randomly distributed in the simulation box. Reaching the equilibrium state, all NH_3 molecules are adsorbed by the CuPc molecules, which are attached to the graphene flake via π-π stacking interactions [125, 147]. In the PH_3 case, only a part of the PH_3 molecule population is adsorbed, of which some PH_3 molecules are attached to graphene surface and others to CuPc.

Meanwhile, the analyte molecules' adsorption amount as a function of simulation time is presented in Fig. 6.11 (e). The amount of NH_3 molecules adsorbed on
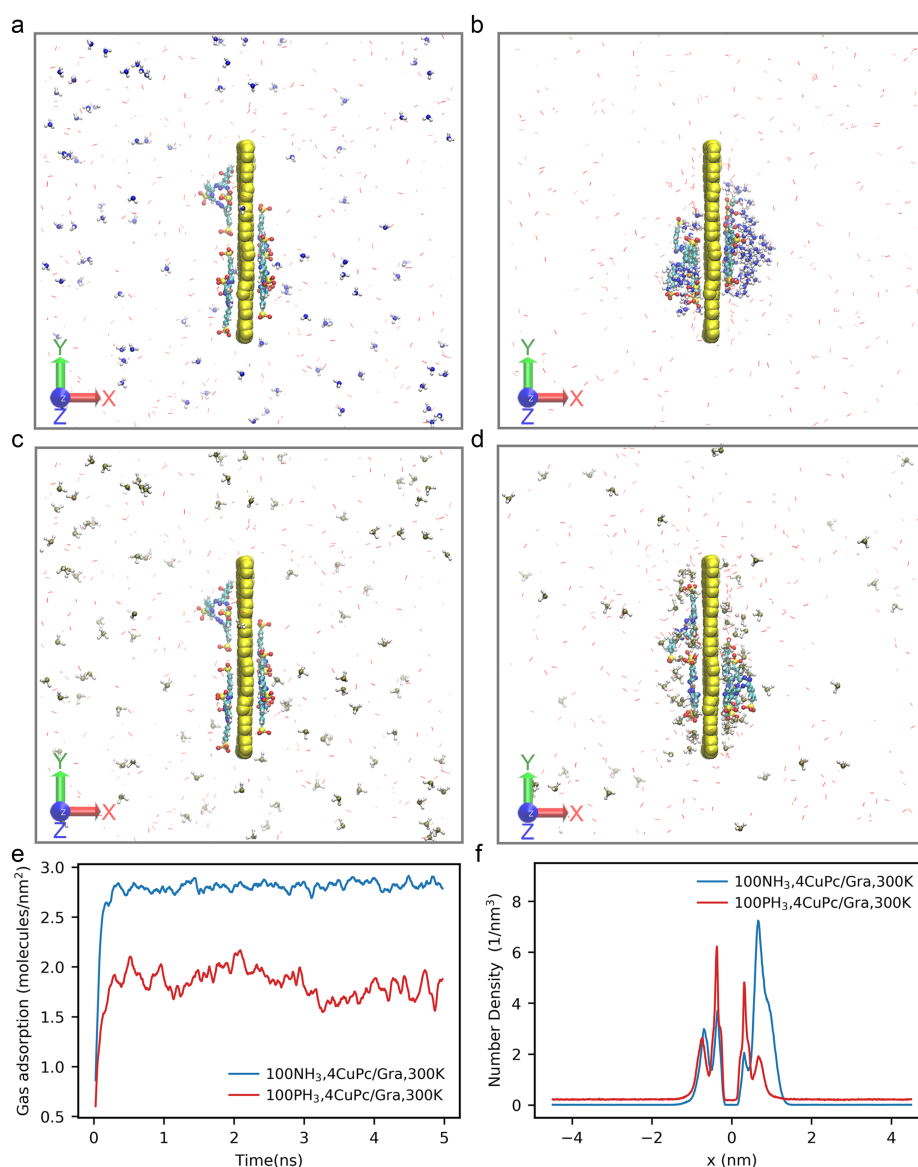
Figure 6.11 Morphology of analyte gas molecules interacting with functionalized graphene *via* molecular dynamics simulation. (a) Initial configuration in NH_3 case model. (b) Equilibrium configuration in NH_3 case model. (c) Initial configuration in PH_3 case model. (b) Equilibrium configuration in PH_3 case model. Color code: graphene flake (dark yellow), copper (orange), nitrogen (blue), hydrogen (white), phosphorus (tan), sulfur (light yellow), oxygen (red), carbon (cyan), carrier gas (red line). (e) Analyte gas molecules adsorption amount as a function of simulation time in both NH_3 case model and PH_3 case model. (f) Analyte gas molecules number density along x axis in both NH_3 model and PH_3 model.

the graphene surface is approximately 61% higher than that of PH_3 under the same condition. The distributions of both analyte molecules along the x axis in the simulation box are plotted in Fig. 6.11 (f). The graphene flake is fixed at position x = 0. In the

NH_3 case (blue line), 4 peaks can be observed at x = -0.70 nm, -0.36 nm, 0.31 nm, and 0.66 nm. Two inner peaks (x = -0.36 nm, 0.31 nm) are supposed to be the results of NH_3 molecule adsorption on the graphene surface while the two outer peaks result from NH_3 molecules adsorption on CuPc molecules. The intensity of the outer peaks is higher than the intensity of the inner peaks, which agrees well with the distribution observation of more NH_3 molecules being attached on CuPc molecules. Likely, in the PH_3 case (red line), there are 4 peaks present at x = -0.74 nm, -0.37 nm, 0.31 nm, 0.67 nm. Two inner peaks are caused by the adsorption of PH_3 molecules on the graphene surface while two outer peaks are induced by the adsorption of PH_3 molecules on the CuPc molecules. The intensity of the inner peaks is about 140% higher than the intensity of the outer peaks in the PH_3 case, which confirms the observation of more PH_3 molecules being attached on the graphene surface. Nevertheless, the intensity of the outer peaks of NH_3 is much higher than the intensity of outer peaks of PH_3, which explains that the adsorption amount of NH_3 molecules by CuPc molecules is larger than the adsorption amount of PH_3 molecules by graphene. Beyond the active range (-1.5 nm < x < 1.5 nm), the number density of NH_3 molecules vanishes while the number density of PH_3 molecules remains at a low level, which validates the observation that, NH_3 molecules are concentrated on CuPc molecules while around 40% of PH_3 molecules remain distributed randomly in the simulation box. The simulation results imply that the interaction between CuPc molecules and NH_3 molecules benefit the adsorption of NH_3 on functionalized graphene, which can be attributed to strong hydrogen bonding interaction between NH_3 and the sulfonic group (SO^{3-}) in CuPc molecules [262, 263]. In contrast to NH_3 molecules, the interaction between CuPc molecules and PH_3 molecules is weaker and contributes less to PH_3 adsorption since weak normal intermolecular forces (for instance, dipole-dipole interaction, van der Waals forces) dominate [264].

6.6 Summary

In this chapter, an ultrasensitive, highly discriminative platform for the detection and identification of NH_3 and PH_3 at room temperature using graphene nanosensors has been demonstrated. Graphene is exfoliated and successfully functionalized by copper phthalocyanine derivate (CuPc). In combination with efficient machine learning techniques, the developed graphene nanosensor demonstrates an excellent gas identification performance even at ultralow concentration, 100 ppb

NH$_3$ (accuracy-100.0%, sensitivity-100.0%, specificity-100.0%), 100 ppb PH$_3$ (accuracy-77.8%, sensitivity-75.0%, and specificity-78.6%). Molecular dynamics simulation results reveal that the CuPc attached on the graphene surface facilitates the adsorption of NH$_3$ on graphene owing to hydrogen bonding interactions. This smart sensor prototype paves a path to design highly discriminative, highly sensitive, miniaturized, non-dedicated gas sensors towards a wide spectrum of industrial gases.

Chapter 7

Conclusions and outlook

7.1 Conclusions

The previous chapters have presented the-state-of-the-art work on the development of pristine graphene-based gas sensors and their application towards inorganic gases detection (NH_3, PH_3) and volatile organic compounds (VOCs) sensing at room temperature. With the integration of machine learning techniques, the selectively of the sensors has been significantly enhanced and the application of such smart platform could be extended to more than individual gas detection field. The excellent discrimination performance and identification performance has been demonstrated towards various gases, such as, odors, PH_3, NH_3, etc.

In chapter 3, the stabilization mechanism of functionalized graphene in dispersants aqueous dispersion has been elucidated using all-atom MD simulations. The morphology of FMNS molecules on graphene flakes has been investigated. It was found that the tail group of the FMNS molecules prefers to stick to the graphene flake while the head group prefers to extend toward the solvent, consistent with their hydrophobic and hydrophilic nature, respectively. The calculation of the PMF of a pair of graphene flakes covered with adsorbed FMNS molecules has been carried out to evaluate influence of FMNS on the dispersion and stabilization of graphene flakes. To achieve approximately the same PMF energy barrier of 10 $kJ/(mol{\cdot}nm^2)$), the surface coverage of graphene flakes by FMNS molecules is 44% lower than by SC molecules, and 71% lower than by SDBS molecules, respectively, which illustrates the superior dispersion and stabilizing performance for exfoliated graphene flake

dispersion. At a high surface coverage, graphene flakes repel each other which leads to the stabilization of graphene dispersions, and at lower coverage graphene flakes can agglomerate easily. The formation of FMNS clusters can suppress the adsorption of FMNS molecules on the graphene surface in the case of high concentration of FMNS and reduce the surface coverage of graphene flake. From the simulations results, it is found that the optimal mass ratio between FMNS and monolayer graphene is 1.06 which yields the highest surface coverage of the graphene flakes by FMNS (0.34 $molecules/nm^2$). These simulation results provide a basis for the understanding of graphene exfoliation assisted by FMNS-like dispersant and paves a path to design highly efficient and biocompatible dispersants for liquid phase exfoliation of defect-free, few layers graphene.

In chapter 4, pristine graphene non-covalently functionalized by a biocompatible stabilizer, i.e., FMNS, was produced for the application in a highly efficient NH_3 gas sensor. The stabilized graphene dispersion was prepared through exfoliation from readily available graphite particles assisted with the FMNS dispersant. The morphology of graphene flakes deposited onto the IDE structure of the gas sensor was found to exhibit an influence on the sensing characteristics. Moreover, the NH_3 adsorption behavior on the FMNS-functionalized graphene flakes was elucidated via all-atom molecular dynamics simulations. The roles of FMNS from graphene preparation to NH_3 sensing were discussed: FMNS acts as a stabilizer for the graphene dispersion, as a p-type dopant for graphene-based sensing element, and provides active adsorption sites for NH_3 gas sensing. This work provides an efficient path to design highly efficient graphene-based NH_3 gas sensors employing FMNS-like molecules, which is fabricated with a facile and environmentally friendly process, biocompatible materials, low-cost equipment, and scale-up capability.

In chapter 5, a biomimetic electronic olfaction using graphene single channel nanosensor have been proposed and its performance is evaluated by incorporating with machine learning algorithm. With previously "learned experience", the e-olfaction demonstrates outstanding odor identification performance, maximizing results from single sensors. Without previously "learned experience", the e-olfaction possibly predicts the odor perceptual pleasantness of odor molecules by establishing a prediction model, although a larger number of odorants need to be analyzed for more significant statistics. It is expected that the integration of arrays containing a variety of graphene functionalization together with the machine learning ap-

proach in each of them would multiply the possibilities and further increase the discrimination power for a much larger amount of target odor molecules and their complex mixtures. The developed e-olfaction mechanism might allow for nasal implant application to warn presence of odor for the people who exhibit olfactory disorder. Its compact size meets the miniaturization trend for implantable electronic sensing devices and could be integrated into mobile device for odor identification. The developed e-olfaction could be applied for the detection of volatile organic compound (VOC) in widely fields, e.g., environmental monitoring, public security, smart farming, disease diagnosis, etc.

In chapter 6, an ultrasensitive, highly discriminative, graphene nano-sensing approach for the detection and identification of NH_3 and PH_3 at room temperature is demonstrated. The exfoliation method provides a simple technique to functionalize graphene at the same step, using the resulting high quality multi-layer flakes as sensing material in miniaturized chemiresistive type sandwiched between gold microelectrodes. In combination with efficient machine learning techniques, the analysis of 11 features from the sensing response profile provides excellent and highly sensitive gas identification performance for NH_3 and PH_3 at ppb levels, with nearly 100% accuracy, sensitivity and specificity for both gases at 500 ppb and maintaining the same level of performance for NH_3 at 100 ppb. Molecular dynamics simulation results indicate that the CuPc molecules attached on graphene surface act as effective sites for NH_3 molecule adsorption via hydrogen-bonding while the attraction between CuPc molecules and PH_3 is quite weak. It is believed that the developed nanosensor prototype provides a solution to design highly discriminative and sensitive, miniaturized, non-dedicated gas sensor which can be applied towards a wide spectrum of industrial gases.

7.2   Outlook

In this work, some preliminary works on odor/gas discrimination using graphene-based gas sensors (e-olfaction) have been conducted. However, there are still a lot of challenges/issues/problems remaining to be investigated/clarified/addressed in this domain before this technology is ready to be transferred to practical application. These include, but are not limited to the below aspects:

- The test time (sampling time), which consists of sensing response time (15 mins) and recovery time (10 mins), could be further optimized. Of course, the test time is dependent on the specific application. For example, for the instant odor detection/the point-of-care testing of disease diagnosis, the sampling time should be further shortened. In order to achieve this purpose, sensing materials could be optimized to increase the response speed of developed sensors, such as introducing functionalization/modifications (such as noble metal nanoparticles, Au, Pt, etc.) to graphene materials, or optimizing the material deposition process to obtain a thinner sensing film, or replacing the current sensing material with some other advanced materials (for instance, carbon nanotubes, metal–organic frameworks, Mxenes, etc.)

- To enhance the detection capability of e-olfaction towards a wide range of odors, instead of adopting single species of sensing material, gas sensor with multiple channels using multiple specifically functionalized materials might be superior.

- To enhance the data processing efficiency of e-olfaction on portable device, cloud computing of sensing data processing and analyzing could be considered.

In addition, a new domain combining the e-olfaction feature of odors and the human olfaction perception of odors could be established to decode the "secret" of odor, which might be beneficial for odor digitalization. For example, much efforts could be contributed to investigate the relationship between the odor features produced in e-olfaction space and odor features in psychological space. Assuming these three features are correlated, it would be helpful to predict the olfactory perception of odors using the e-olfaction device directly. In this case, large amount of odor could be measured by the developed e-olfaction device as well as precepted by well-organized olfaction perceptional test in large amount of population. With machine learning technique, the correlation model between the e-olfaction features and the perceptional features of the odors might be created.

Appendix A

The Appendix is supplementary information for Chapter 5.

Odor concentration could be determined via the below equation [265, 266]:

$$C(ppm) = 10^6 \times \frac{P_{odor}}{P_0} \times \frac{v_c}{v_c + v_d} \tag{7.1}$$

Where, P_{odor} is saturated vapor pressure of odorant solvent at room temperature, P_0 is the input nitrogen gas pressure (760 $mmHg$), V_c and V_d are the flow rate ($sccm$) of both carrier gas and dilution gas, respectively. Atmospheric pressure is applied in our experiments and the working temperature is room temperature. Odor information refers to Table. A.1

Table A.1 Odor physicochemical property parameters [221, 267]. M: molecular weight (unit: g/mol); ρ: density (unit: g/cm^3); T_B: Boiling point (unit: °C); V_p: Vapor pressure(unit: Pa); D: Dipole moment(unit: Debye); σ: Surface tension (unit: dyn/cm); $TPSA$: Topological Polar Surface Area (unit: Å^2); α: Polarizability (unit: Å^3); N_{Dn}: Hydrogen bond donor number(unit: 1); N_{Ac}: Hydrogen bond acceptor number(unit: 1).

odor	M	ρ	T_B	V_p	D	σ	$TPSA$	α	N_{Dn}	N_{Ac}
Euca	154	0.92	172	253.31	1.58	61.5	9.2	18.5	0	1
2Nona	142	0.82	195	213.31	2.88	26.5	17.1	18.4	0	1
Euge	164	1.06	254	2.94	2.81	30.9	29.5	17.9	1	2
2Phe	122	1.02	225	11.57	1.60	40.4	20.20	13.87	1	1

Table A.2 Gas flow rate in odor mixture exposure experiment. V_d:dilution nitrogen flow rate ($sccm$), V_c:carrier nitrogen gas flow rate ($sccm$).

Gas flow rate at exposure phase for odor mixture task					
Vd	100	100	100	100	100
Vc	20	20	20	20	20
Combination of odor mixture (constant total odor carrier gas flow rate, 20 $sccm$)					
Odor mixture	100%–0%	75%–25%	50%–50%	25%–75%	0%–100%
Euca-2Nona	20–0	15–5	10–10	5–15	0–20
Euge-2Phe	20–0	15–5	10–10	5–15	0–20
Euca-Euge	20–0	15–5	10–10	5–15	0–20
Euca-2Phe	20–0	15–5	10–10	5–15	0–20
Euge-2Nona	20–0	15–5	10–10	5–15	0–20
2Phe-2Nona	20–0	15–5	10–10	5–15	0–20
Gas flow rate at flushing phase for odor mixture task					
Vd	2000	2000	2000	2000	2000
Vc	0	0	0	0	0
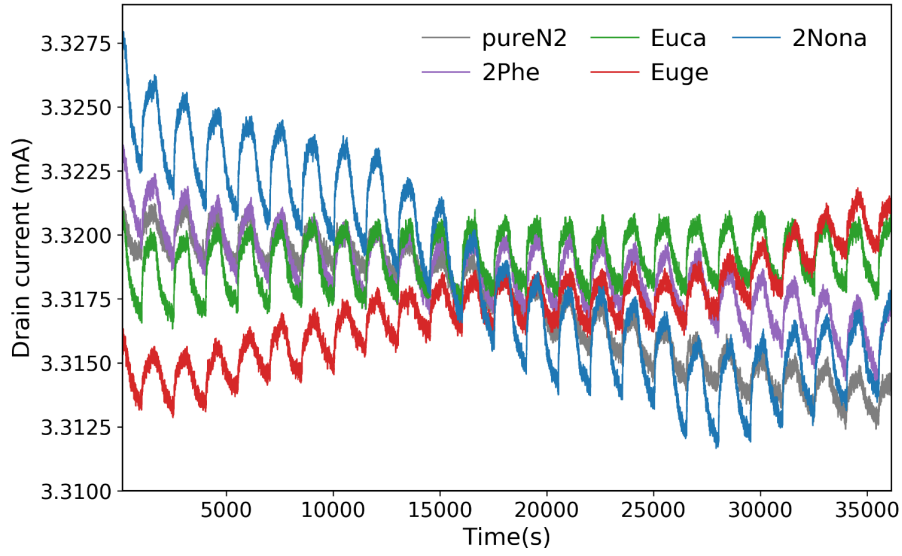
Figure A.1 Raw sensing signal of e-olfaction towards to different odors.

Odor fingerprint pattern consisting of 7 most important features is represented in the radar chart shown in Fig. A.2 (a)-(e). From these graphics, Euca possesses strong peaks in odor feature $S, area, a_{min}, k_{min}$, and k_{max}. 2Phe exhibits a strong peak in odor feature b_1, b_2, a_{min}, and moderate peak in odor feature $S, area, k_{min}$, and k_{max}. Euge demonstrates a strong signal in odor feature b_1, b_2, a_{min}, and k_{min}. 2Nona shows the ultrahigh signal in odor feature $k_{max}, S, area, b_1$ and moderate signal in odor feature b_2. Odor reference reveals a strong peak in odor feature a_{min}, k_{min}, S. Each odor is represented by a unique and characteristic pattern, which could be utilized as the odor fingerprint or odor identity. Interestingly, it is observed that a large overlapping area exists between any two odors among Euca, Euge, and 2Phe, as shown in Fig. A.2 (f)-(h). These results further corroborate the previous result that odor clusters overlapping exists within Euca, Euge, and 2Phe, displayed in Fig. A.2 (a).

Similar to the results of odor mixture Euca-2Nona and odor mixture Euge-2Phe shown in the main text, the other groups of odor mixture are displayed in Fig. A.3-Fig. A.6. From these results, it is indicated that the nature of odor mixture 2Phe-2Nona behaves much more similar to 2Phe, whereas the odor mixture Euca-2Phe overlaps with both odor components. The nature of odor mixture Euge-2Nona exhibits much closer to Euge and odor mixture Euge-Euca behave in the same manner.
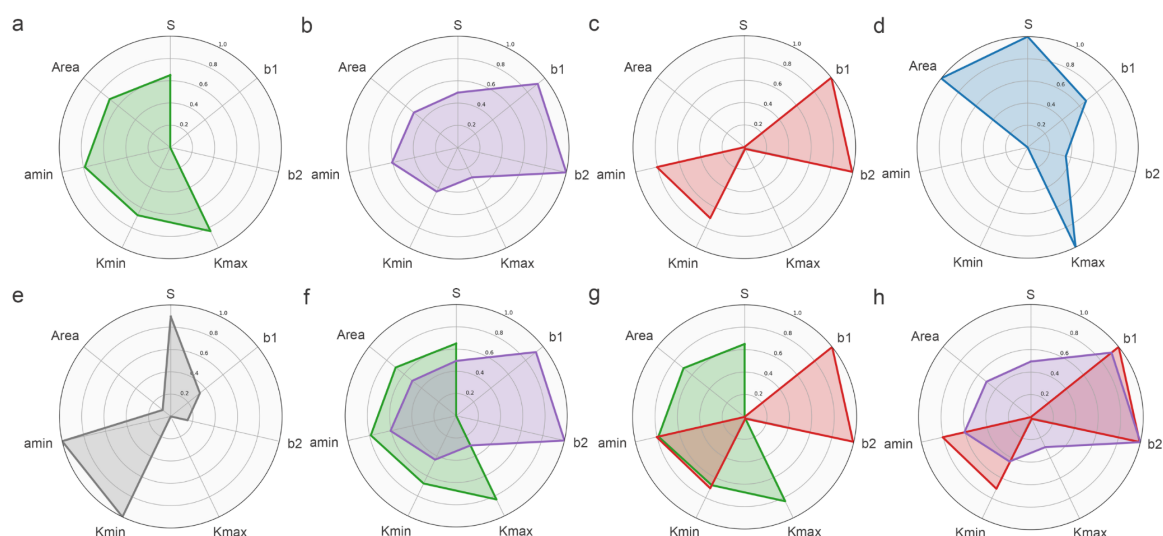
Figure A.2 Odor fingerprints. Odor fingerprint is analyzed based on 7 features with high importance loading. (a) Euca. (b) 2Phe. (c) Euge. (d) 2Nona. (e) Odor reference (pure N2). (f) Euca and 2Phe. (g) Euca and Euge. (h) Euge and 2Phe.

The statistical results for binary odor mixture similarity to odor component is shown on Fig. A.7.
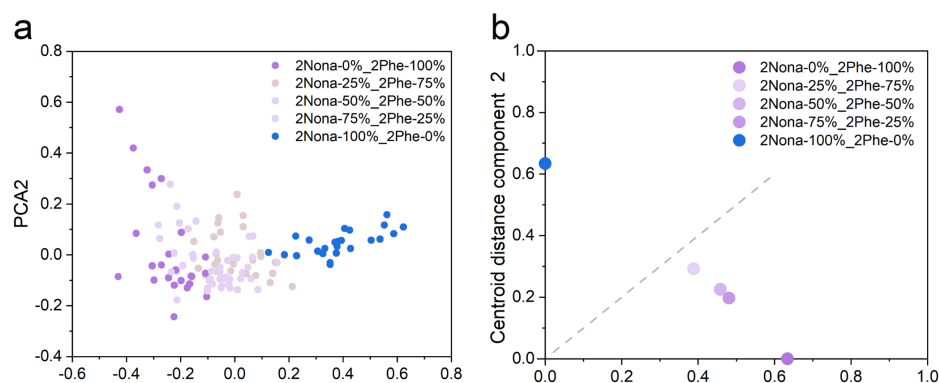
Figure A.3 Binary odor mixture (2Nona and 2Phe) similarity to odor component. (a) PCA analytical result of odor mixture (2Nona and 2Phe). (b) Centroid distance component (CDC) analytical result of odor mixture (2Nona and 2Phe).
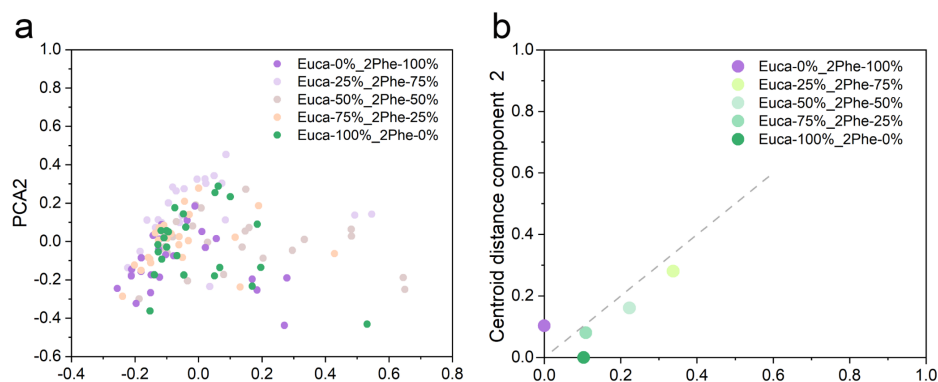
Figure A.4 Binary odor mixture (Euca and 2Phe) similarity to odor component. (a) PCA analytical result of odor mixture (Euca and 2Phe). (b) Centroid distance component (CDC) analytical result of odor mixture (Euca and 2Phe).
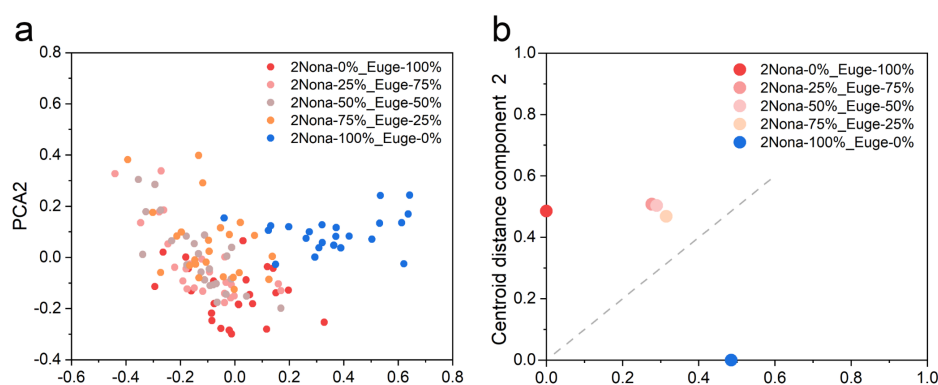
Figure A.5 Binary odor mixture (2Nona and Euge) similarity to odor component. (a) PCA analytical result of odor mixture (2Nona and Euge). (b) Centroid distance component (CDC) analytical result of odor mixture (2Nona and Euge).
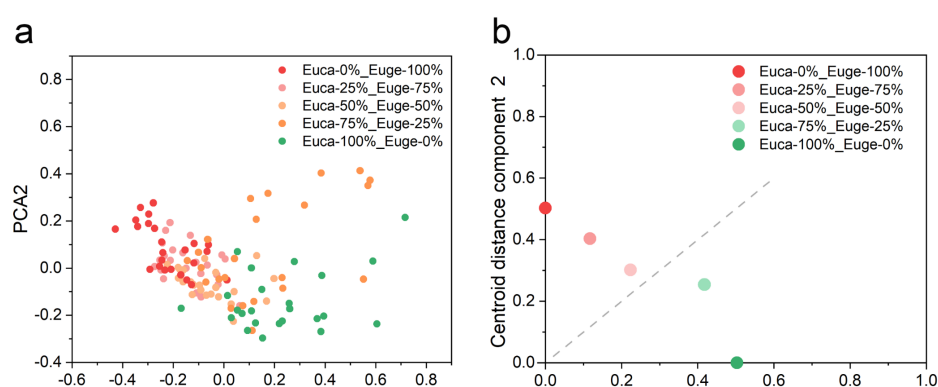
Figure A.6 Binary odor mixture (Euca and Euge) similarity to odor component. (a) PCA analytical result of odor mixture (Euca and Euge). (b) Centroid distance component (CDC) analytical result of odor mixture (Euca and Euge).
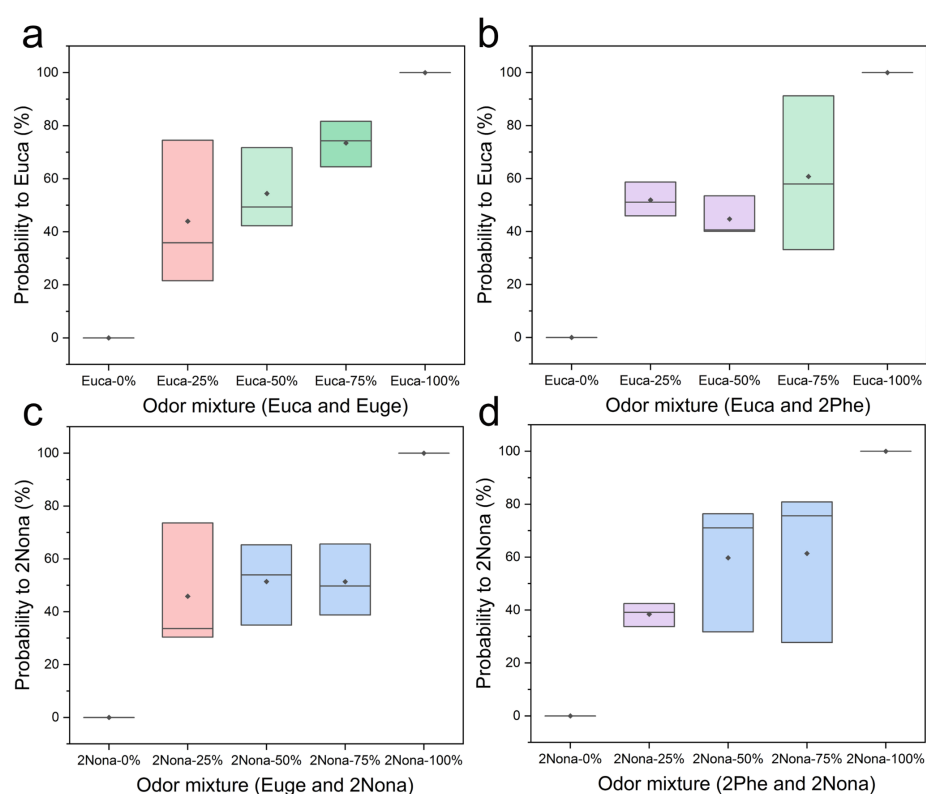
Figure A.7 Statistical results for binary odor mixture similarity to odor component. (a) Probability of odor mixture (Euca and Euge) to odor component Euca as a function of odor Euca ratio. (b) Probability of odor mixture (Euca and 2Phe) to odor component Euca as a function of odor Euca ratio. (c) Probability of odor mixture (Euge and 2Nona) to odor component 2Nona as a function of odor 2Nona ratio. (d) Probability of odor mixture (2Phe and 2Nona) to odor component 2Nona as a function of odor 2Nona ratio.

For the other combination groups of odor mixture, molecular dynamic simulation were conducted as well, as shown in Fig. A.8–Fig. A.11. The center of mass (COM) distance between odor molecules and APTS molecules were calculated as well, as shown in Fig. A.12. From the simulation results, it is shown that in odor mixture 2Nona-2Phe, 2Phe molecules approach closer to APTS than 2Nona. In odor mixture Euca-2Phe, Euca molecules approach closer to APTS than 2Phe. In odor mixture Euge-2Nona or Euge-Euca, Euge molecules approach closer to APTS than the other component. This means Euge molecules possess much higher chance to be adsorbed by APTS molecules, which consists well with the binding energy results calculated by DFT shown in Fig 5.12(h).
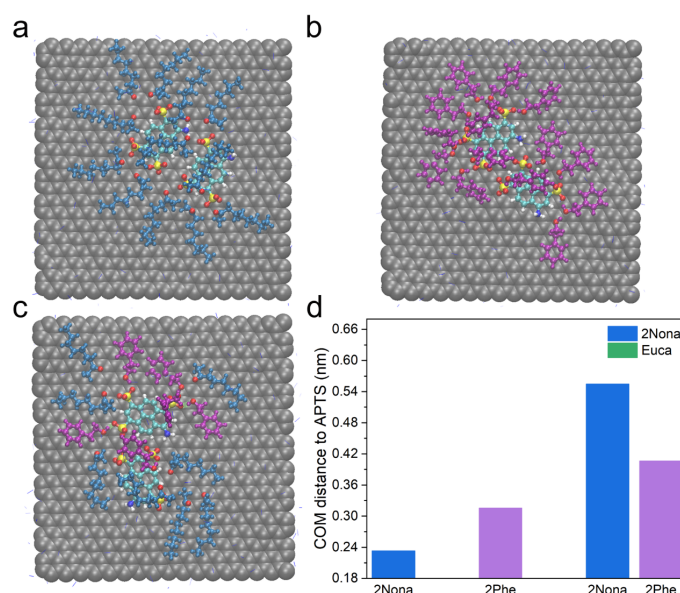
Figure A.8 Simulation results of odor molecules (2Nona, Euca) interaction with APTS molecules on graphene. (a) Snapshot of 2Nona molecules interaction with APTS on graphene. (b) Snapshot of 2Phe molecules interaction with APTS on graphene. (c) Snapshot of odor molecules interaction with APTS on graphene in 2Nona-2Phe odor mixture. (d) Center of mass (COM) distance between odor molecules and APTS molecules.
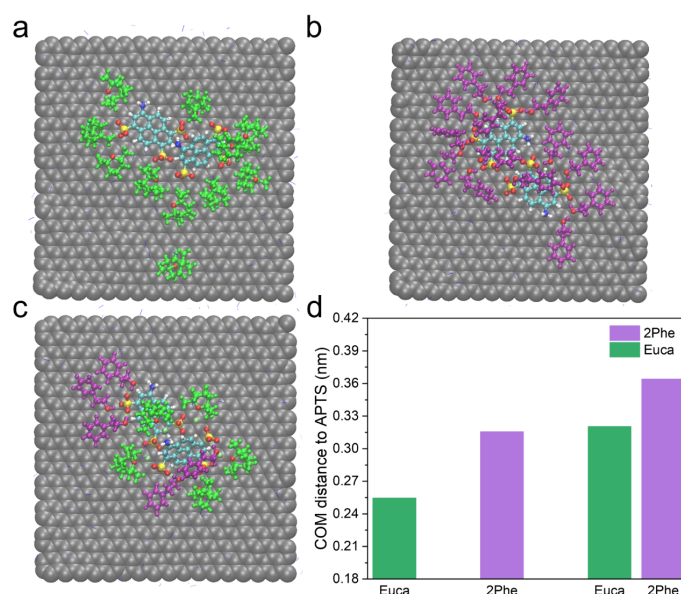
Figure A.9 Simulation results of odor molecules (Euca, 2Phe) interaction with APTS molecules on graphene. (a) Snapshot of Euca molecules interaction with APTS on graphene. (b) Snapshot of 2Phe molecules interaction with APTS on graphene. (c) Snapshot of odor molecules interaction with APTS on graphene in Euca-2Phe odor mixture. (d) Center of mass (COM) distance between odor molecules and APTS molecules.
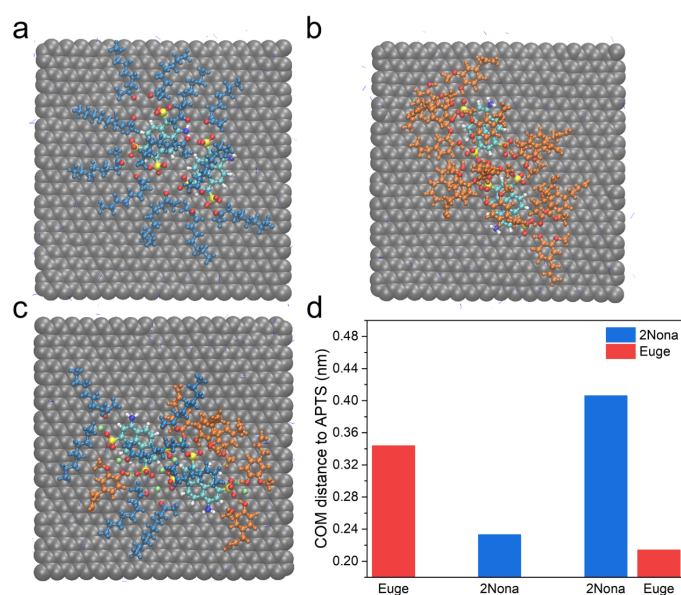
Figure A.10 Simulation of odor molecules (2Nona, Euge) interaction with APTS molecules on graphene. (a) Snapshot of 2Nona molecules interaction with APTS on graphene. (b) Snapshot of Euge molecules interaction with APTS on graphene. (c) Snapshot of odor molecules interaction with APTS on graphene in 2Nona-Euge odor mixture. (d) Center of mass (COM) distance between odor molecules and APTS molecules.
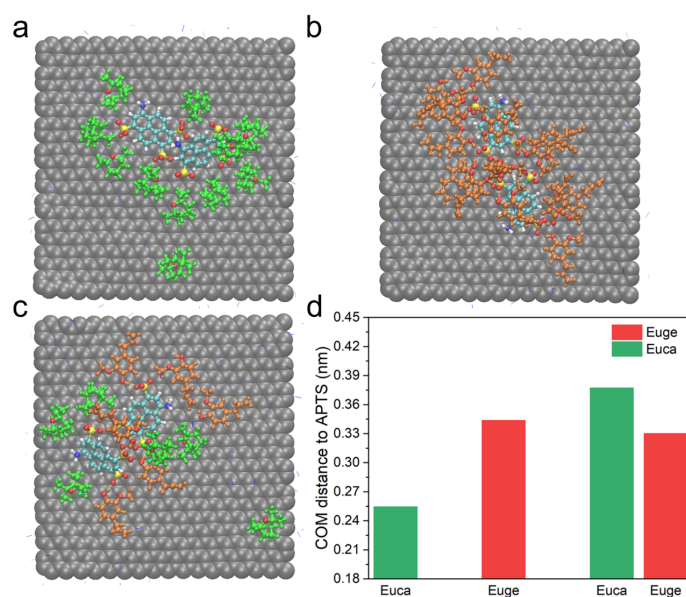
Figure A.11 Simulation of odor molecules (Euge, Euca) interaction with APTS molecules on graphene. (a) Snapshot of Euca molecules interaction with APTS on graphene. (b) Snapshot of Euge molecules interaction with APTS on graphene. (c) Snapshot of odor molecules interaction with APTS on graphene in Euca-Euge odor mixture. (d) Center of mass (COM) distance between odor molecules and APTS molecules.
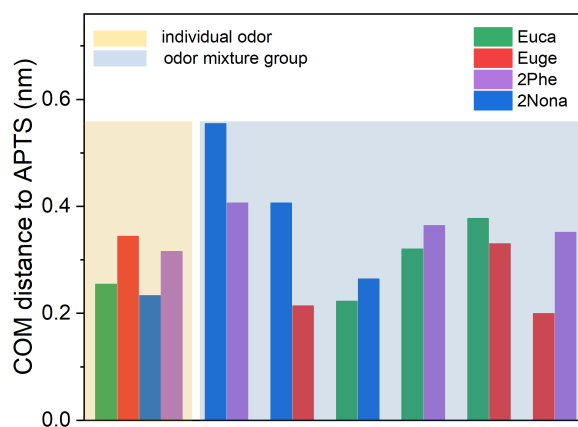
Figure A.12 Center of mass (COM) distance between odor molecules and APTS molecules. (Left) Pure odor model. (Right) Odor mixture model.
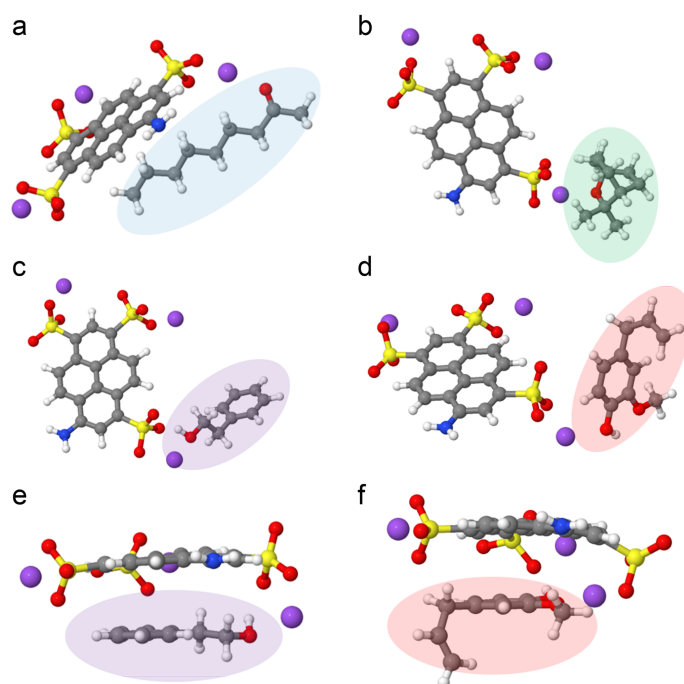
Figure A.13 Configurations of odor molecules interacting with APTS molecules via DFT calculation. (a) Odor 2Nona with APTS. (b) Odor Euca with APTS. (c) Odor 2Phe with APTS (without π-π interactions). (d) Odor Euge with APTS (without π-π interactions). (e) Odor 2Phe with APTS (with π-π interactions). (f) Odor Euge with APTS (with π-π interactions).
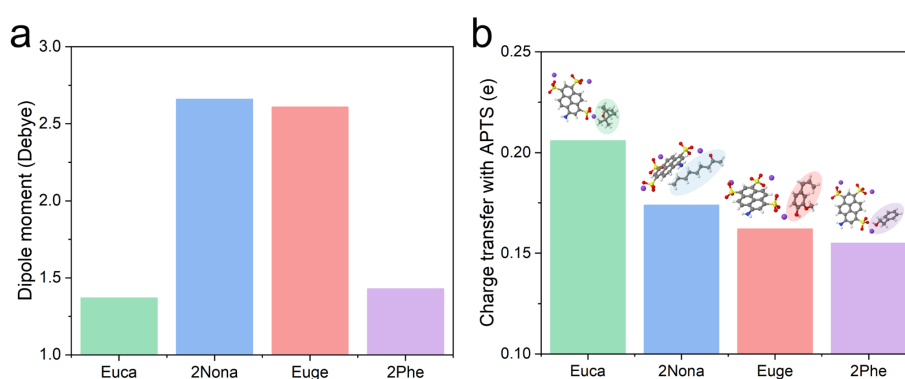
Figure A.14 Odor molecules interaction with APTS molecules via DFT calculation. (a) Odor dipole moment interacting with APTS molecules. (b) Charge transfer between odor molecules and APTS molecules (considering non-stacking configuration for Euge and 2Phe molecules).

Bibliography

[1] M. F. Bashir, B. J. Ma, Bilal, B. Komal, M. A. Bashir, T. H. Farooq, N. Iqbal, and M. Bashir. Correlation between environmental pollution indicators and covid-19 pandemic: A brief study in californian context. *Environ Res*, 187:109652, 2020. doi:10.1016/j.envres.2020.109652.

[2] C. D. Koolen and G. Rothenberg. Air pollution in Europe. *ChemSusChem*, 12 (1):164–172, 2019. doi:10.1002/cssc.201802292.

[3] Huaifang Zhang, Yao Wang, Binbin Zhang, Yawei Yan, Jie Xia, Xuejiang Liu, Xiaoyu Qiu, and Yawen Tang. Construction of ultrasensitive ammonia sensor using ultrafine ir decorated hollow graphene nanospheres. *Electrochimica Acta*, 304:109–117, 2019. doi:10.1016/j.electacta.2018.11.215.

[4] Zuquan Wu, Xiangdong Chen, Shibu Zhu, Zuowan Zhou, Yao Yao, Wei Quan, and Bin Liu. Enhanced sensitivity of ammonia sensor using graphene/polyaniline nanocomposite. *Sensors and Actuators B: Chemical*, 178:485–493, 2013. doi:10.1016/j.snb.2013.01.014.

[5] Björn Timmer, Wouter Olthuis, and Albert van den Berg. Ammonia sensors and their applications—a review. *Sensors and Actuators B: Chemical*, 107(2): 666–677, 2005. doi:10.1016/j.snb.2004.11.054.

[6] Y. Wang, K. K. Lew, T. T. Ho, L. Pan, S. W. Novak, E. C. Dickey, J. M. Redwing, and T. S. Mayer. Use of phosphine as an n-type dopant source for vapor-liquid-solid growth of silicon nanowires. *Nano Lett*, 5(11):2139–43, 2005. doi:10.1021/nl051442h.

[7] Waqas Wakil, Nickolas G. Kavallieratos, Muhammad Usman, Sehrish Gulzar, and Hamadttu A. F. El-Shafie. Detection of phosphine resistance in field populations of four key stored-grain insect pests in pakistan. *Insects*, 12(4):288, 2021. doi:10.3390/insects12040288.

[8] R. Bhuvaneswari, V. Nagarajan, and R. Chandiramouli. Arsenene nanoribbons for sensing NH3 and PH3 gas molecules – a first-principles perspective. *Applied Surface Science*, 469:173–180, 2019. doi:10.1016/j.apsusc.2018.11.003.

[9] Hamid Rajabi, Mojgan Hadi Mosleh, Parthasarathi Mandal, Amanda Lea-Langton, and Majid Sedighi. Emissions of volatile organic compounds from crude oil processing – global emission inventory and environmental release. *Science of The Total Environment*, 727:138654, 2020. doi:10.1016/j.scitotenv.2020.138654.

[10] L. Spinelle, M. Gerboles, G. Kok, S. Persijn, and T. Sauerwald. Review of portable and low-cost sensors for the ambient air monitoring of benzene and other volatile organic compounds. *Sensors (Basel)*, 17(7):30, 2017. doi:10.3390/s17071520.

[11] Y. Huang, S. S. Ho, Y. Lu, R. Niu, L. Xu, J. Cao, and S. Lee. Removal of indoor volatile organic compounds via photocatalytic oxidation: A short review and prospect. *Molecules*, 21(1):56, 2016. doi:10.3390/molecules21010056.

[12] Charles J. Weschler. Changes in indoor pollutants since the 1950s. *Atmospheric Environment*, 43(1):153–169, 2009. doi:10.1016/j.atmosenv.2008.09.044.

[13] M. V. Nikolic, V. Milovanovic, Z. Z. Vasiljevic, and Z. Stamenkovic. Semiconductor gas sensors: Materials, technology, design, and application. *Sensors (Basel)*, 20(22), 2020. doi:10.3390/s20226694.

[14] Noboru Yamazoe. Toward innovations of gas sensor technology. *Sensors and Actuators B: Chemical*, 108(1-2):2–14, 2005. doi:10.1016/j.snb.2004.12.075.

[15] S. M. Minhajul Alam, Arnob Barua, Ahamed Raihan, M. J. Alam, Rocky Chakma, S. S. Mahtab, and Chitra Biswas. Design and implementation of a smart helmet system for underground miner's safety. In V. Bindhu, João Manuel R. S. Tavares, Alexandros-Apostolos A. Boulogeorgos, and Chandrasekar Vuppalapati, editors, *International Conference on Communication, Computing and Electronics Systems*, pages 301–311. Springer Singapore. doi:10.1007/978-981-33-4909-4_22.

[16] M. S. Farooq, S. Riaz, A. Abid, K. Abid, and M. A. Naeem. A survey on the role of iot in agriculture for the implementation of smart farming. *IEEE Access*, 7: 156237–156271, 2019. doi:10.1109/ACCESS.2019.2949703.

[17] G. Hunter, J. Xu, L. Dungan, B. Ward, S. Rowe, J. Williams, D. B. Makel, Chung-Chiun Liu, and C. Chang. Smart sensor systems for aerospace applications: From sensor development to application testing. *ECS Transactions*, 16(11):333–344, 2019. doi:10.1149/1.2981136.

[18] R. F. Kennedy and S. Nahavandi. A low-cost intelligent gas sensing device for military applications. In *2008 Congress on Image and Signal Processing*, volume 4, pages 3–8. doi:10.1109/CISP.2008.749.

[19] Jun Chen, Juanhong Gu, Rong Zhang, Yuezhong Mao, and Shiyi Tian. Freshness evaluation of three kinds of meats based on the electronic nose. *Sensors*, 19(3):605, 2019. doi:10.3390/s19030605.

[20] Sarah Khanniche, Didier Mathieu, Franck Pereira, Céline Frenois, Delphine Colin, Christelle Barthet, and Lionel Hairault. Quantitative evaluation of the responses of a gravimetric gas sensor based on mesoporous functionalized silica: Application to 2,4-DNT and TNT detection. *Sensors and Actuators B: Chemical*, 248:470–480, 2017. doi:10.1016/j.snb.2017.03.137.

[21] G. Peng, U. Tisch, O. Adams, M. Hakim, N. Shehada, Y. Y. Broza, S. Billan, R. Abdah-Bortnyak, A. Kuten, and H. Haick. Diagnosing lung cancer in exhaled breath using gold nanoparticles. *Nat Nanotechnol*, 4(10):669–73, 2009. doi:10.1038/nnano.2009.235.

[22] Benjie Shan, Yoav Y. Broza, Wenjuan Li, Yong Wang, Sihan Wu, Zhengzheng Liu, Jiong Wang, Shuyu Gui, Lin Wang, Zhihong Zhang, Wei Liu, Shoubing Zhou, Wei Jin, Qianyu Zhang, Dandan Hu, Lin Lin, Qiujun Zhang, Wenyu Li, Jinquan Wang, Hu Liu, Yueyin Pan, and Hossam Haick. Multiplexed nanomaterial-based sensor array for detection of COVID-19 in exhaled breath. *ACS Nano*, 14(9):12125–12132, 2020. doi:10.1021/acsnano.0c05657.

[23] Marco Righettoni, Antonio Tricoli, and Sotiris E. Pratsinis. Si:WO3 sensors for highly selective detection of acetone for easy diagnosis of diabetes by breath analysis. *Analytical Chemistry*, 82(9):3581–3587, 2010. doi:10.1021/ac902695n.

[24] H. C. Lau, J. B. Yu, H. W. Lee, J. S. Huh, and J. O. Lim. Investigation of exhaled breath samples from patients with alzheimer's disease using gas chromatography-mass spectrometry and an exhaled breath sensor system. *Sensors (Basel)*, 17(8), 2017. doi:10.3390/s17081783.

[25] J. P. M. Finberg, M. Schwartz, R. Jeries, S. Badarny, M. K. Nakhleh, E. Abu Daoud, Y. Ayubkhanov, M. Aboud-Hawa, Y. Y. Broza, and H. Haick. Sensor array for detection of early stage parkinson's disease before medication. *ACS Chem Neurosci*, 9(11):2548–2553, 2018. doi:10.1021/acschemneuro.8b00245.

[26] Andrey Somov, Alexander Baranov, Alexey Savkin, Denis Spirjakin, Andrey Spirjakin, and Roberto Passerone. Development of wireless sensor network for combustible gas monitoring. *Sensors and Actuators A: Physical*, 171(2):398–405, 2011. doi:10.1016/j.sna.2011.07.016.

[27] N. Jaber, S. Ilyas, O. Shekhah, M. Eddaoudi, and M. I. Younis. Multimode excitation of a metal organics frameworks coated microbeam for smart gas sensing and actuation. *Sensors and Actuators A: Physical*, 283:254–262, 2018. doi:10.1016/j.sna.2018.10.004.

[28] N. Yamazoe and K. Shimanoe. *Fundamentals of semiconductor gas sensors*, pages 3–34. 2013. doi:10.1533/9780857098665.1.3.

[29] Tomoki Maekawa, Jun Tamaki, Norio Miura, Noboru Yamazoe, and Shigenori Matsushima. Development of SnO2-based ethanol gas sensor. *Sensors and Actuators B: Chemical*, 9(1):63–69, 1992. doi:10.1016/0925-4005(92)80195-4.

[30] J. Dai, O. Ogbeide, N. Macadam, Q. Sun, W. Yu, Y. Li, B. L. Su, T. Hasan, X. Huang, and W. Huang. Printed gas sensors. *Chem Soc Rev*, 49(6):1756–1789, 2020. doi:10.1039/c9cs00459a.

[31] Roberto Paolesse, Sara Nardis, Donato Monti, Manuela Stefanelli, and Corrado Di Natale. Porphyrinoids for chemical sensor applications. *Chemical Reviews*, 117(4):2517–2583, 2017. doi:10.1021/acs.chemrev.6b00361.

[32] A. Hulanicki, S. Glab, and F. Ingman. Chemical sensors: definitions and classification. *Pure and Applied Chemistry*, 63(9):1247–1250, 1991. doi:10.1351/pac199163091247.

[33] Carsten Schwandt, R. Vasant Kumar, and Matthew P. Hills. Solid state electrochemical gas sensor for the quantitative determination of carbon dioxide. *Sensors and Actuators B: Chemical*, 265:27–34, 2018. doi:10.1016/j.snb.2018.03.012.

[34] Vladimir V. Plashnitsa, Perumal Elumalai, Yuki Fujio, and Norio Miura. Zirconia-based electrochemical gas sensors using nano-structured sensing materials aiming at detection of automotive exhausts. *Electrochimica Acta*, 54(25):6099–6106, 2009. doi:10.1016/j.electacta.2008.12.040.

[35] Jinjun Shi, Yongfa Zhu, Xinrong Zhang, Willy R. G. Baeyens, and Ana M. Recent developments in nanomaterial optical sensors. *TrAC Trends in Analytical Chemistry*, 23(5):351–360, 2004. doi:10.1016/S0165-9936(04)00519-9.

[36] Jane Hodgkinson and Ralph P. Tatam. Optical gas sensing: a review. *Measurement Science and Technology*, 24(1), 2013. doi:10.1088/0957-0233/24/1/012004.

[37] Xiaochao Tan, Heng Zhang, Junyu Li, Haowei Wan, Qiushi Guo, Houbin Zhu, Huan Liu, and Fei Yi. Non-dispersive infrared multi-gas sensing via nanoantenna integrated narrowband detectors. *Nature Communications*, 11(1):5245, 2020. doi:10.1038/s41467-020-19085-1.

[38] Andrey Makeenkov, Igor Lapitskiy, Andrey Somov, and Alexander Baranov. Flammable gases and vapors of flammable liquids: Monitoring with infrared sensor node. *Sensors and Actuators B: Chemical*, 209:1102–1107, 2015. doi:10.1016/j.snb.2014.11.112.

[39] Alexandru Oprea and Udo Weimar. Gas sensors based on mass-sensitive transducers part 1: transducers and receptors—basic understanding. *Analytical and Bioanalytical Chemistry*, 411(9):1761–1787, 2019. doi:10.1007/s00216-019-01630-7.

[40] Wiesław P. Jakubik. Surface acoustic wave-based gas sensors. *Thin Solid Films*, 520(3):986–993, 2011. doi:10.1016/j.tsf.2011.04.174.

[41] Nguyen Van Quy, Vu Anh Minh, Nguyen Van Luan, Vu Ngoc Hung, and Nguyen Van Hieu. Gas sensing properties at room temperature of a quartz crystal microbalance coated with ZnO nanorods. *Sensors and Actuators B: Chemical*, 153(1):188–193, 2011. doi:10.1016/j.snb.2010.10.030.

[42] J. Lerchner, D. Caspary, and G. Wolf. Calorimetric detection of volatile organic compounds. *Sensors and Actuators B: Chemical*, 70(1):57–66, 2000. doi:10.1016/S0925-4005(00)00554-2.

[43] Patrick Kirchner, Jan Oberländer, Peter Friedrich, Jörg Berger, Henri-Pierre Suso, Andriy Kupyna, Michael Keusgen, and Michael J. Schöning. Optimisation and fabrication of a calorimetric gas sensor built up on a polyimide substrate for H2O2 monitoring. *physica status solidi (a)*, 208(6):1235–1240, 2011. doi:10.1002/pssa.201001132.

[44] Ghenadii Korotcenkov. Handbook of gas sensor materials. *Conventional approaches*, 1, 2013. doi:10.1007/978-1-4614-7165-3.

[45] Pratik V Shinde and Chandra Sekhar Rout. Magnetic gas sensing: working principles and recent developments. *Nanoscale Advances*, 3(6):1551–1568, 2021. doi:10.1039/d0na00826e.

[46] Eduard Llobet. Gas sensors using carbon nanomaterials: A review. *Sensors and Actuators B: Chemical*, 179:32–45, 2013. doi:10.1016/j.snb.2012.11.014.

[47] S. M. Majhi, A. Mirzaei, H. W. Kim, S. S. Kim, and T. W. Kim. Recent advances in energy-saving chemiresistive gas sensors: A review. *Nano Energy*, 79:105369, 2021. doi:10.1016/j.nanoen.2020.105369.

[48] Bapathi Kumaar Swamy Reddy and Pramod H Borse. Recent material advances and their mechanistic approaches for room temperature chemiresistive gas sensors. *Journal of The Electrochemical Society*, 168(5):057521, 2021. doi:10.3389/fsens.2021.657931.

[49] Pooja Saxena and Prashant Shukla. *A Review on Gas Sensor Technology and Its Applications*, book section Chapter 18, pages 165–175. Smart Innovation, Systems and Technologies. 2022. doi:10.1007/978-981-16-2857-3_18.

[50] Noriya Izu, Woosuck Shin, and Norimitsu Murayama. Numerical analysis of response time for resistive oxygen gas sensors. *Sensors and Actuators B: Chemical*, 87(1):99–104, 2002. doi:10.1016/S0925-4005(02)00225-3.

[51] D. M. Wilson, S. Hoyt, J. Janata, K. Booksh, and L. Obando. Chemical sensors for portable, handheld field instruments. *IEEE Sensors Journal*, 1(4):256–274, 2001. doi:10.1109/7361.983465.

[52] H. C. Wang, Y. Li, and M. J. Yang. Fast response thin film sno2 gas sensors operating at room temperature. *Sensors and Actuators B: Chemical*, 119(2):380–383, 2006. doi:10.1016/j.snb.2005.12.037.

[53] Javier Burgués, Juan Manuel Jiménez-Soto, and Santiago Marco. Estimation of the limit of detection in semiconductor gas sensors through linearized calibration models. *Analytica Chimica Acta*, 1013:13–25, 2018. doi:10.1016/j.aca.2018.01.062.

[54] Tetsuro Seiyama, Akio Kato, Kiyoshi Fujiishi, and Masanori Nagatani. A new detector for gaseous components using semiconductive thin films. *Analytical Chemistry*, 34(11):1502–1503, 1962. doi:10.1021/ac60191a001.

[55] P. J. Shaver. Activated tungsten oxide gas detectors. *Applied Physics Letters*, 11 (8):255–257, 1967. doi:10.1063/1.1755123.

[56] Naoyoshi Taguchi. Gas-detecting device, 1971.

[57] Hyo-Joong Kim and Jong-Heun Lee. Highly sensitive and selective gas sensors using p-type oxide semiconductors: Overview. *Sensors and Actuators B: Chemical*, 192:607–627, 2014. doi:10.1016/j.snb.2013.11.005.

[58] Hisahito Ogawa, Masahiro Nishikawa, and Atsushi Abe. Hall measurement studies and an electrical conduction model of tin oxide ultrafine particle films. *Journal of Applied Physics*, 53(6):4448–4455, 1982. doi:10.1063/1.331230.

[59] M. Suchea, S. Christoulakis, K. Moschovis, N. Katsarakis, and G. Kiriakidis. Zno transparent thin films for gas sensor applications. *Thin Solid Films*, 515(2):551–554, 2006. doi:10.1016/j.tsf.2005.12.295.

[60] Evelyn Alves Nunes Simonetti, Thais Cardoso de Oliveira, Ádamo Enrico do Carmo Machado, Amanda Alvarenga Coutinho Silva, Alan Silva dos Santos, and Luciana de Simone Cividanes. TiO2 as a gas sensor: The novel carbon structures and noble metals as new elements for enhancing sensitivity – a review. *Ceramics International*, 47(13):17844–17876, 2021. doi:10.1016/j.ceramint.2021.03.189.

[61] P. P. Gonzalez-Borrero, F. Sato, A. N. Medina, M. L. Baesso, A. C. Bento, G. Baldissera, C. Persson, G. A. Niklasson, C. G. Granqvist, and A. Ferreira da Silva. Optical band-gap determination of nanostructured WO3 film. *Applied Physics Letters*, 96(6), 2010. doi:10.1063/1.3313945.

[62] Yong Kwon Jeong and Gyeong Man Choi. Nonstoichiometry and electrical conduction of CuO. *Journal of Physics and Chemistry of Solids*, 57(1):81–84, 1996. doi:10.1016/0022-3697(95)00130-1.

[63] Nasser Mohammed Hosny. Synthesis, characterization and optical band gap of NiO nanoparticles derived from anthranilic acid precursors via a thermal decomposition route. *Polyhedron*, 30(3):470–476, 2011. doi:10.1016/j.poly.2010.11.020.

[64] Samira Dabaghmanesh, Rolando Saniz, Erik Neyts, and Bart Partoens. Sulfur-alloyed cr2o3: a new p-type transparent conducting oxide host. *RSC Advances*, 7(8):4453–4459, 2017. doi:10.1039/C6RA27852C.

[65] Bilge Saruhan, Roussin Lontio Fomekong, and Svitlana Nahirniak. Review: Influences of semiconductor metal oxide properties on gas sensing characteristics. *Frontiers in Sensors*, 2, 2021. doi:10.3389/fsens.2021.657931.

[66] Nicolae Barsan and Udo Weimar. Conduction model of metal oxide gas sensors. *Journal of Electroceramics*, 7(3):143–167, 2001. doi:10.1023/A:1014405811371.

[67] Supab Choopun, Niyom Hongsith, and Ekasiddh Wongrat. *Metal-Oxide Nanowires for Gas Sensors*, book section Chapter 1. 2012. doi:10.5772/54385.

[68] A. Katsuki and K. Fukui. H2 selective gas sensor based on SnO2. *Sensors and Actuators B: Chemical*, 52(1):30–37, 1998. doi:10.1016/S0925-4005(98)00252-4.

[69] Faramarz Hossein-Babaei, Mehrdad Keshmiri, Mohammad Kakavand, and Tom Troczynski. A resistive gas sensor based on undoped p-type anatase. *Sensors and Actuators B: Chemical*, 110(1):28–35, 2005. doi:10.1016/j.snb.2005.01.010.

[70] N. Barsan, D. Koziej, and U. Weimar. Metal oxide-based gas sensor research: How to? *Sensors and Actuators B: Chemical*, 121(1):18–35, 2007. doi:10.1016/j.snb.2006.09.047.

[71] S. J. Pearton, F. Ren, Yu-Lin Wang, B. H. Chu, K. H. Chen, C. Y. Chang, Wantae Lim, Jenshan Lin, and D. P. Norton. Recent advances in wide bandgap semiconductor biological and gas sensors. *Progress in Materials Science*, 55(1):1–59, 2010. doi:10.1016/j.pmatsci.2009.08.003.

[72] C. Wang, L. Yin, L. Zhang, D. Xiang, and R. Gao. Metal oxide gas sensors: sensitivity and influencing factors. *Sensors (Basel)*, 10(3):2088–106, 2010. doi:10.3390/s100302088.

[73] C Nylander, M Armgarth, and I Lundström. An ammonia detector based on a conducting polymer. In *Proceedings of the International Meeting on Chemical Sensors*, volume 17, pages 203–207, Fukuoka.

[74] Partha Pratim Sengupta, Satyananda Barik, and Basudam Adhikari. Polyaniline as a gas-sensor material. *Materials and Manufacturing Processes*, 21(3):263–270, 2006. doi:10.1080/10426910500464602.

[75] Chia-Yu Lin, Jian-Ging Chen, Chih-Wei Hu, James J. Tunney, and Kuo-Chuan Ho. Using a PEDOT:PSS modified electrode for detecting nitric oxide gas. *Sensors and Actuators B: Chemical*, 140(2):402–406, 2009. doi:10.1016/j.snb.2009.04.041.

[76] S. T. Navale, A. T. Mane, M. A. Chougule, R. D. Sakhare, S. R. Nalage, and V. B. Patil. Highly selective and sensitive room temperature no2 gas sensor based on polypyrrole thin films. *Synthetic Metals*, 189:94–99, 2014. doi:10.1016/j.synthmet.2014.01.002.

[77] Dan Xie and Yadong Jiang. The properties of praseodymium bis[octakis(octyloxy)phthalocyaninato] complex langmuir–blodgett films for NO2 sensor. *Sensors and Actuators B: Chemical*, 93(1):379–383, 2003. doi:10.1016/S0925-4005(03)00206-5.

[78] Yotsarayuth Seekaew, Shongpun Lokavee, Ditsayut Phokharatkul, Anurat Wisitsoraat, Teerakiat Kerdcharoen, and Chatchawal Wongchoosuk. Low-cost and flexible printed graphene–PEDOT:PSS gas sensor for ammonia detection. *Organic Electronics*, 15(11):2971–2981, 2014. doi:10.1016/j.orgel.2014.08.044.

[79] Tapan K. Das and Smita Prusty. Review on conducting polymers and their applications. *Polymer-Plastics Technology and Engineering*, 51(14):1487–1500, 2012. doi:10.1080/03602559.2012.710697.

[80] S. A. Krutovertsev, O. M. Ivanova, and S. I. Sorokin. Sensing properties of polyaniline films doped with dawson heteropoly compounds. *Journal of Analytical Chemistry*, 56(11):1057–1060, 2001. doi:10.1023/A:1012569127685.

[81] Alan Graham MacDiarmid, R. J. Mammone, R. B. Kaner, Lord Porter, R. Pethig, A. J. Heeger, D. R. Rosseinsky, Ronald James Gillespie, and Peter Day. The concept of conducting polymers the role of reduction potentials. *Philosophical Transactions of the Royal Society of London. Series A, Mathematical and Physical Sciences*, 314(1528):3–15, 1985. doi:10.1098/rsta.1985.0004.

[82] J. Kong, N. R. Franklin, C. Zhou, M. G. Chapline, S. Peng, K. Cho, and H. Dai. Nanotube molecular wires as chemical sensors. *Science*, 287(5453):622–5, 2000. doi:10.1126/science.287.5453.622.

[83] Mohd Nurazzi Norizan, Muhammad Harussani Moklis, Siti Zulaikha Ngah Demon, Norhana Abdul Halim, Alinda Samsuri, Imran Syakir Mohamad, Victor Feizal Knight, and Norli Abdullah. Carbon nanotubes: functionalisation and their application in chemical sensors. *RSC Advances*, 10(71):43704–43732, 2020. doi:10.1039/D0RA09438B.

[84] Jean-Joseph Adjizian, Radouane Leghrib, Antal A. Koos, Irene Suarez-Martinez, Alison Crossley, Philipp Wagner, Nicole Grobert, Eduard Llobet, and Christopher P. Ewels. Boron- and nitrogen-doped multi-wall carbon nanotubes for gas detection. *Carbon*, 66:662–673, 2014. doi:10.1016/j.carbon.2013.09.064.

[85] Li Niu, Yanling Luo, and Zhanqing Li. A highly selective chemical gas sensor based on functionalization of multi-walled carbon nanotubes with poly(ethylene glycol). *Sensors and Actuators B: Chemical*, 126(2):361–367, 2007. doi:10.1016/j.snb.2007.03.018.

[86] Paul C. P. Watts, Natacha Mureau, Zhenni Tang, Yoji Miyajima, J. David Carey, and S. Ravi P. Silva. The importance of oxygen-containing defects on carbon nanotubes for the detection of polar and non-polar vapours through hydrogen bond formation. *Nanotechnology*, 18(17):175701, 2007. doi:10.1088/0957-4484/18/17/175701.

[87] Michael F. L. De Volder, Sameh H. Tawfick, Ray H. Baughman, and A. John Hart. Carbon nanotubes: Present and future commercial applications. *Science*, 339 (6119):535–539, 2013. doi:10.1126/science.1222453.

[88] Tae H. Kim, Yeon H. Kim, Seo Y. Park, Soo Y. Kim, and Ho W. Jang. Two-Dimensional transition metal disulfides for chemoresistive gas sensing: Perspective and challenges. *Chemosensors*, 5(2), 2017. doi:10.3390/chemosensors5020015.

[89] Ananya Dey. Semiconductor metal oxide gas sensors: A review. *Materials Science and Engineering: B*, 229:206–217, 2018. doi:10.1016/j.mseb.2017.12.036.

[90] K. S. Novoselov, A. K. Geim, S. V. Morozov, D. Jiang, Y. Zhang, S. V. Dubonos, I. V. Grigorieva, and A. A. Firsov. Electric field effect in atomically thin carbon films. *Science*, 306(5696):666–9, 2004. doi:10.1126/science.1102896.

[91] K. S. Novoselov, V. I. Fal'ko, L. Colombo, P. R. Gellert, M. G. Schwab, and K. Kim. A roadmap for graphene. *Nature*, 490(7419):192–200, 2012. doi:10.1038/nature11458.

[92] Alexander S Mayorov, Roman V Gorbachev, Sergey V Morozov, Liam Britnell, Rashid Jalil, Leonid A Ponomarenko, Peter Blake, Kostya S Novoselov, Kenji Watanabe, and Takashi Taniguchi. Micrometer-scale ballistic transport in encapsulated graphene at room temperature. *Nano letters*, 11(6):2396–2399, 2011. doi:10.1021/nl200758b.

[93] Michael J. McAllister, Je-Luen Li, Douglas H. Adamson, Hannes C. Schniepp, Ahmed A. Abdala, Jun Liu, Margarita Herrera-Alonso, David L. Milius, Roberto Car, Robert K. Prud'homme, and Ilhan A. Aksay. Single sheet functionalized graphene by oxidation and thermal expansion of graphite. *Chemistry of Materials*, 19(18):4396–4404, 2007. doi:10.1021/cm0630800.

[94] Xiao-Ye Wang, Akimitsu Narita, and Klaus Müllen. Precision synthesis versus bulk-scale fabrication of graphenes. *Nature Reviews Chemistry*, 2(1), 2017. doi:10.1038/s41570-017-0100.

[95] Anisha N Patel, Manon Guille Collignon, Michael A O'Connell, Wendy OY Hung, Kim McKelvey, Julie V Macpherson, and Patrick R Unwin. A new view of electrochemistry at highly oriented pyrolytic graphite. *Journal of the American Chemical Society*, 134(49):20117–20130, 2012. doi:10.1021/ja308615h.

[96] Y. Hernandez, V. Nicolosi, M. Lotya, F. M. Blighe, Z. Sun, S. De, I. T. McGovern, B. Holland, M. Byrne, Y. K. Gun'Ko, J. J. Boland, P. Niraj, G. Duesberg, S. Krishnamurthy, R. Goodhue, J. Hutchison, V. Scardaci, A. C. Ferrari, and J. N. Coleman. High-yield production of graphene by liquid-phase exfoliation of graphite. *Nat Nanotechnol*, 3(9):563–8, 2008. doi:10.1038/nnano.2008.215.

[97] L. Dong, J. Yang, M. Chhowalla, and K. P. Loh. Synthesis and reduction of large sized graphene oxide sheets. *Chem Soc Rev*, 46(23):7306–7316, 2017. doi:10.1039/c7cs00485k.

[98] A. T. Murdock, A. Koos, T. B. Britton, L. Houben, T. Batten, T. Zhang, A. J. Wilkinson, R. E. Dunin-Borkowski, C. E. Lekka, and N. Grobert. Controlling the orientation, edge geometry, and thickness of chemical vapor deposition graphene. *ACS Nano*, 7(2):1351–9, 2013. doi:10.1021/nn3049297.

[99] H. Huang, W. Chen, S. Chen, and A. T. Wee. Bottom-up growth of epitaxial graphene on 6H-SiC(0001). *ACS Nano*, 2(12):2513–8, 2008. doi:10.1021/nn800711v.

[100] A. Narita, X. Feng, Y. Hernandez, S. A. Jensen, M. Bonn, H. Yang, I. A. Verzhbitskiy, C. Casiraghi, M. R. Hansen, A. H. Koch, G. Fytas, O. Ivasenko, B. Li, K. S. Mali, T. Balandina, S. Mahesh, S. De Feyter, and K. Mullen. Synthesis of structurally well-defined and liquid-phase-processable graphene nanoribbons. *Nat Chem*, 6(2):126–32, 2014. doi:10.1038/nchem.1819.

[101] F. Schedin, A. K. Geim, S. V. Morozov, E. W. Hill, P. Blake, M. I. Katsnelson, and K. S. Novoselov. Detection of individual gas molecules adsorbed on graphene. *Nature Materials*, 6(9):652–655, 2007. doi:10.1038/nmat1967.

[102] Yaping Dan, Ye Lu, Nicholas J. Kybert, Zhengtang Luo, and A. T. Charlie Johnson. Intrinsic response of graphene vapor sensors. *Nano Letters*, 9(4):1472–1475, 2009. doi:10.1021/nl8033637.

[103] O. Leenaerts, B. Partoens, and F. M. Peeters. Adsorption of H2O , NH3 , CO, NO2 , and NO on graphene: A first-principles study. *Physical Review B*, 77(12): 125416, 2008. doi:10.1103/PhysRevB.77.125416.

[104] Jesse D. Fowler, Matthew J. Allen, Vincent C. Tung, Yang Yang, Richard B. Kaner, and Bruce H. Weiller. Practical chemical sensors from chemically derived graphene. *ACS Nano*, 3(2):301–306, 2009. doi:10.1021/nn800593m.

[105] Zongbiao Ye, Huiling Tai, Rui Guo, Zhen Yuan, Chunhua Liu, Yuanjie Su, Zhi Chen, and Yadong Jiang. Excellent ammonia sensing performance of gas sensor based on graphene/titanium dioxide hybrid with improved morphology. *Applied Surface Science*, 419:84–90, 2017. doi:10.1016/j.apsusc.2017.03.251.

[106] Jianhua Sun, Xin Shu, Yanli Tian, Zhangfa Tong, Shouli Bai, Ruixian Luo, Dianqing Li, and Chung Chiun Liu. Facile preparation of polypyrrole-reduced graphene oxide hybrid for enhancing nh3 sensing at room temperature. *Sensors and Actuators B: Chemical*, 241:658–664, 2017. doi:10.1016/j.snb.2016.10.047.

[107] Zhuo Chen, Ahmad Umar, Shiwei Wang, Yao Wang, Tong Tian, Ying Shang, Yuzun Fan, Qi Qi, Dongmei Xu, and Lei Jiang. Supramolecular fabrication of multilevel graphene-based gas sensors with high NO2 sensibility. *Nanoscale*, 7(22):10259–10266, 2015. doi:10.1039/C5NR01770J.

[108] W. Yuan, A. Liu, L. Huang, C. Li, and G. Shi. High-performance NO2 sensors based on chemically modified graphene. *Adv Mater*, 25(5):766–71, 2013. doi:10.1002/adma.201203172.

[109] Kehan Yu, Pengxiang Wang, Ganhua Lu, Ke-Hung Chen, Zheng Bo, and Junhong Chen. Patterning vertically oriented graphene sheets for nanodevice applications. *The Journal of Physical Chemistry Letters*, 2(6):537–542, 2011. doi:10.1021/jz200087w.

[110] Gugang Chen, Tereza M. Paronyan, and Avetik R. Harutyunyan. Sub-ppt gas detection with pristine graphene. *Applied Physics Letters*, 101(5), 2012. doi:10.1063/1.4742327.

[111] Shirong Huang, Luis Antonio Panes-Ruiz, Alexander Croy, Markus Löffler, Vyacheslav Khavrus, Viktor Bezugly, and Gianaurelio Cuniberti. Highly sensitive room temperature ammonia gas sensor using pristine graphene: The role of biocompatible stabilizer. *Carbon*, 173:262–270, 2021. doi:10.1016/j.carbon.2020.11.001.

[112] L. A. Panes-Ruiz, M. Shaygan, Y. Fu, Y. Liu, V. Khavrus, S. Oswald, T. Gemming, L. Baraban, V. Bezugly, and G. Cuniberti. Toward highly sensitive and energy efficient ammonia gas detection with modified single-walled carbon nanotubes at room temperature. *ACS Sens*, 3(1):79–86, 2018. doi:10.1021/acssensors.7b00358.

[113] A. Vijayaraghavan, C. Sciascia, S. Dehm, A. Lombardo, A. Bonetti, A. C. Ferrari, and R. Krupke. Dielectrophoretic assembly of high-density arrays of individual graphene devices for rapid screening. *ACS Nano*, 3(7):1729–34, 2009. doi:10.1021/nn900288d.

[114] R. Ghosh, A. Midya, S. Santra, S. K. Ray, and P. K. Guha. Chemically reduced graphene oxide for ammonia detection at room temperature. *ACS Appl Mater Interfaces*, 5(15):7599–603, 2013. doi:10.1021/am4019109.

[115] Berk Hess, Carsten Kutzner, David van der Spoel, and Erik Lindahl. GROMACS 4 algorithms for highly efficient, load-balanced, and scalable molecular simulation. *Journal of Chemical Theory and Computation*, 4(3):435–447, 2008. doi:10.1021/ct700301q.

[116] Kurt Binder, Jürgen Horbach, Walter Kob, Wolfgang Paul, and Fathollah Varnik. Molecular dynamics simulations. *Journal of Physics: Condensed Matter*, 16(5): S429–S453, 2004. doi:10.1088/0953-8984/16/5/006.

[117] Carlo Trozzi and Giovanni Ciccotti. Stationary nonequilibrium states by molecular dynamics. ii. Newton's law. *Physical Review A*, 29(2):916–925, 1984. doi:10.1103/PhysRevA.29.916.

[118] William L. Jorgensen, David S. Maxwell, and Julian Tirado-Rives. Development and testing of the opls all-atom force field on conformational energetics and properties of organic liquids. *Journal of the American Chemical Society*, 118(45): 11225–11236, 1996. doi:10.1021/ja9621760.

[119] Nathan Schmid, Andreas P. Eichenberger, Alexandra Choutko, Sereina Riniker, Moritz Winger, Alan E. Mark, and Wilfred F. van Gunsteren. Definition and testing of the GROMOS force-field versions 54A7 and 54B7. *European Biophysics Journal*, 40(7):843, 2011. doi:10.1007/s00249-011-0700-9.

[120] H. J. C. Berendsen, J. P. M. Postma, W. F. van Gunsteren, A. DiNola, and J. R. Haak. Molecular dynamics with coupling to an external bath. *The Journal of Chemical Physics*, 81(8):3684–3690, 1984. doi:10.1063/1.448118.

[121] Giovanni Bussi, Davide Donadio, and Michele Parrinello. Canonical sampling through velocity rescaling. *The Journal of Chemical Physics*, 126(1):014101, 2007. doi:10.1063/1.2408420.

[122] D. C. Rapaport, Robin L. Blumberg, Susan R. McKay, and Wolfgang Christian. The art of molecular dynamics simulation. *Computers in Physics*, 10(5):456–456, 1996. doi:10.1063/1.4822471.

[123] Mohammad Hossin and M. N. Sulaiman. A review on evaluation metrics for data classification evaluations. *International Journal of Data Mining & Knowledge Management Process*, 5(2):11, 2015. doi:10.5121/ijdkp.2015.5201.

[124] Xiaohua Hu, Xiaodan Zhang, Caimei Lu, E. K. Park, and Xiaohua Zhou. Exploiting wikipedia as external knowledge for document clustering, 2009.

[125] Shirong Huang, Alexander Croy, Viktor Bezugly, and Gianaurelio Cuniberti. Stabilization of aqueous graphene dispersions utilizing a biocompatible dispersant: a molecular dynamics study. *Physical Chemistry Chemical Physics*, 21 (43):24007–24016, 2019. doi:10.1039/c9cp04742e.

[126] T. Kuila, S. Bose, P. Khanra, A. K. Mishra, N. H. Kim, and J. H. Lee. Recent advances in graphene-based biosensors. *Biosens Bioelectron*, 26(12):4637–48, 2011. doi:10.1016/j.bios.2011.05.039.

[127] Roberto Muñoz and Cristina Gómez-Aleixandre. Review of CVD synthesis of graphene. *Chemical Vapor Deposition*, 19(10-11-12):297–322, 2013. doi:10.1002/cvde.201300051.

[128] Neeraj Mishra, John Boeckl, Nunzio Motta, and Francesca Iacopi. Graphene growth on silicon carbide: A review. *physica status solidi (a)*, 213(9):2277–2289, 2016. doi:10.1002/pssa.201600091.

[129] S. Yang, M. R. Lohe, K. Mullen, and X. Feng. New-generation graphene from electrochemical approaches: Production and applications. *Adv Mater*, 28(29): 6213–21, 2016. doi:10.1002/adma.201505326.

[130] Wufeng Chen, Lifeng Yan, and P. R. Bangal. Chemical reduction of graphene oxide to graphene by sulfur-containing compounds. *The Journal of Physical Chemistry C*, 114(47):19885–19890, 2010. doi:10.1021/jp107131v.

[131] Rekha Narayan and Sang Ouk Kim. Surfactant mediated liquid phase exfoliation of graphene. *Nano Convergence*, 2(1):20, 2015. doi:10.1186/s40580-015-0050-x.

[132] Sumit Goenka, Vinayak Sant, and Shilpa Sant. Graphene-based nanomaterials for drug delivery and tissue engineering. *Journal of Controlled Release*, 173:75–88, 2014. doi:10.1016/j.jconrel.2013.10.017.

[133] Hong Zhao, Ruihua Ding, Xin Zhao, Yiwei Li, Liangliang Qu, Hao Pei, Lara Yildirimer, Zhengwei Wu, and Weixia Zhang. Graphene-based nanomaterials for drug and/or gene delivery, bioimaging, and tissue engineering. *Drug Discovery Today*, 22(9):1302–1317, 2017. doi:10.1016/j.drudis.2017.04.002.

[134] M. A. Lewis. Chronic toxicities of surfactants and detergent builders to algae: A review and risk assessment. *Ecotoxicology and Environmental Safety*, 20(2): 123–140, 1990. doi:10.1016/0147-6513(90)90052-7.

[135] Sharrel Rebello, Aju K. Asok, Sathish Mundayoor, and M. S. Jisha. Surfactants: toxicity, remediation and green surfactants. *Environmental Chemistry Letters*, 12(2):275–287, 2014. doi:10.1007/s10311-014-0466-2.

[136] M. Ayán-Varela, J. I. Paredes, L. Guardia, S. Villar-Rodil, J. M. Munuera, M. Díaz-González, C. Fernández-Sánchez, A. Martínez-Alonso, and J. M. D. Tascón. Achieving extremely concentrated aqueous dispersions of graphene flakes and catalytically efficient graphene-metal nanoparticle hybrids with flavin mononucleotide as a high-performance stabilizer. *ACS Applied Materials & Interfaces*, 7(19):10293–10307, 2015. doi:10.1021/acsami.5b00910.

[137] Sang-Yong Ju, Jonathan Doll, Ity Sharma, and Fotios Papadimitrakopoulos. Selection of carbon nanotubes with specific chiralities using helical assemblies of flavin mononucleotide. *Nature Nanotechnology*, 3(6):356–362, 2008. doi:10.1038/nnano.2008.148.

[138] Woojin Yoon, Yonggeun Lee, Hongje Jang, Myungsu Jang, Jin Sung Kim, Hee Sung Lee, Seongil Im, Doo Wan Boo, Jiwoong Park, and Sang-Yong Ju. Graphene nanoribbons formed by a sonochemical graphene unzipping using flavin mononucleotide as a template. *Carbon*, 81:629–638, 2015. doi:10.1016/j.carbon.2014.09.097.

[139] William L. Jorgensen and Julian Tirado-Rives. Potential energy functions for atomic-level simulations of water and organic and biomolecular systems. *Proceedings of the National Academy of Sciences of the United States of America*, 102 (19):6665, 2005. doi:10.1073/pnas.0408037102.

[140] Leela S. Dodda, Jonah Z. Vilseck, Julian Tirado-Rives, and William L. Jorgensen. 1.14*CM1A-LBCC: Localized bond-charge corrected cm1a charges for condensed-phase simulations. *The Journal of Physical Chemistry B*, 121(15): 3864–3870, 2017. doi:10.1021/acs.jpcb.7b00272.

[141] Shuichi Miyamoto and Peter A. Kollman. Settle: An analytical version of the SHAKE and RATTLE algorithm for rigid water models. *Journal of Computational Chemistry*, 13(8):952–962, 1992. doi:10.1002/jcc.540130805.

[142] Ailan Cheng and W. A. Steele. Computer simulation of ammonia on graphite. i. low temperature structure of monolayer and bilayer films. *The Journal of Chemical Physics*, 92(6):3858–3866, 1990. doi:10.1063/1.458562.

[143] N. R. Tummala and A. Striolo. Curvature effects on the adsorption of aqueous sodium-dodecyl-sulfate surfactants on carbonaceous substrates: structural features and counterion dynamics. *Phys Rev E Stat Nonlin Soft Matter Phys*, 80 (2 Pt 1):021408, 2009. doi:10.1103/PhysRevE.80.021408.

[144] Tom Darden, Darrin York, and Lee Pedersen. Particle mesh ewald an n log(n) method for ewald sums in large systems. *The Journal of Chemical Physics*, 98 (12):10089–10092, 1993. doi:10.1063/1.464397.

[145] Z. Xu, X. Yang, and Z. Yang. A molecular simulation probing of structure and interaction for supramolecular sodium dodecyl sulfate/single-wall carbon nanotube assemblies. *Nano Lett*, 10(3):985–91, 2010. doi:10.1021/nl9041005.

[146] Justin A. Lemkul and David R. Bevan. Assessing the stability of alzheimer's amyloid protofibrils using molecular dynamics. *The Journal of Physical Chemistry B*, 114(4):1652–1660, 2010. doi:10.1021/jp9110794.

[147] N. R. Tummala, B. H. Morrow, D. E. Resasco, and A. Striolo. Stabilization of aqueous carbon nanotube dispersions using surfactants: insights from molecular dynamics simulations. *ACS Nano*, 4(12):7193–204, 2010. doi:10.1021/nn101929f.

[148] A. Hardy, J. Dix, C. D. Williams, F. R. Siperstein, P. Carbone, and H. Bock. Design rules for graphene and carbon nanotube solvents and dispersants. *ACS Nano*, 12(2):1043–1049, 2018. doi:10.1021/acsnano.7b05159.

[149] Brian C. Stephenson, Arthur Goldsipe, Kenneth J. Beers, and Daniel Blankschtein. Quantifying the hydrophobic effect 1 a computer simulation molecular thermodynamic model for the self assembly of hydrophobic and amphiphilic solutes in aqueous solution. *The Journal of Physical Chemistry B*, 111(5):1025–1044, 2007. doi:10.1021/jp065696i.

[150] J. Łukasiewicz, H. Grajek, and D. Frąckowiak. The influence of flavo nucleotide (fmn) dimerization on the efficiency of the fmn triplet states generation. *Dyes and Pigments*, 73(3):377–382, 2007. doi:10.1016/j.dyepig.2006.01.004.

[151] Zoltán Király, Gerhard H. Findenegg, and Ágnes Mastalir. Chain-length anomaly in the two-dimensional ordering of the cationic surfactants CnTAB at the graphite/water interface, revealed by advanced calorimetric methods. *The Journal of Physical Chemistry B*, 107(45):12492–12496, 2003. doi:10.1021/jp035466t.

[152] Jae Hyun Park and N. R. Aluru. Self-assembly of graphenes. *Surface Science*, 605(17):1616–1620, 2011. doi:10.1016/j.susc.2011.02.011.

[153] S. Lin, C. J. Shih, M. S. Strano, and D. Blankschtein. Molecular insights into the surface morphology, layering structure, and aggregation kinetics of surfactant-stabilized graphene dispersions. *J Am Chem Soc*, 133(32):12810–23, 2011. doi:10.1021/ja2048013.

[154] Bin Wu and Xiaoning Yang. Molecular simulation of electrolyte-induced interfacial interaction between SDS/Graphene assemblies. *The Journal of Physical Chemistry C*, 117(44):23216–23223, 2013. doi:10.1021/jp4038842.

[155] Ronan J. Smith, Mustafa Lotya, and Jonathan N. Coleman. The importance of repulsive potential barriers for the dispersion of graphene using surfactants. *New Journal of Physics*, 12(12):125008, 2010. doi:10.1088/1367-2630/12/12/125008.

[156] Haoyue Sun and Xiaoning Yang. Molecular simulation of self-assembly structure and interfacial interaction for sdbs adsorption on graphene. *Colloids and Surfaces A: Physicochemical and Engineering Aspects*, 462:82–89, 2014. doi:10.1016/j.colsurfa.2014.08.013.

[157] T. Yang, H. Chen, Z. Qiu, R. Yu, S. Luo, W. Li, and K. Jiao. Direct electrochemical vibrio dna sensing adopting highly stable graphene-flavin mononucleotide aqueous dispersion modified interface. *ACS Appl Mater Interfaces*, 10(5):4540–4547, 2018. doi:10.1021/acsami.7b18212.

[158] C. F. Isley and M. P. Taylor. Air quality management in the pacific islands: A review of past performance and implications for future directions. *Environmental Science & Policy*, 84:8, 2018. doi:10.1016/j.envsci.2018.02.013.

[159] T. N. Ly and S. Park. Highly sensitive ammonia sensor for diagnostic purpose using reduced graphene oxide and conductive polymer. *Sci Rep*, 8(1):18030, 2018. doi:10.1038/s41598-018-36468-z.

[160] N. Joshi, T. Hayasaka, Y. Liu, H. Liu, Jr. Oliveira, O. N., and L. Lin. A review on chemiresistive room temperature gas sensors based on metal oxide nanostructures, graphene and 2D transition metal dichalcogenides. *Mikrochim Acta*, 185(4):213, 2018. doi:10.1007/s00604-018-2750-5.

[161] Shyamasree Gupta Chatterjee, Somenath Chatterjee, Ajoy K. Ray, and Amit K. Chakraborty. Graphene–metal oxide nanohybrids for toxic gas sensor: A review. *Sensors and Actuators B: Chemical*, 221:1170–1181, 2015. doi:10.1016/j.snb.2015.07.070.

[162] Alexander J. Samuels and J. David Carey. Engineering graphene conductivity for flexible and high-frequency applications. *ACS Applied Materials & Interfaces*, 7(40):22246–22255, 2015. doi:10.1021/acsami.5b05140.

[163] Wenjing Yuan and Gaoquan Shi. Graphene-based gas sensors. *Journal of Materials Chemistry A*, 1(35), 2013. doi:10.1039/c3ta11774j.

[164] Keith R. Paton, Eswaraiah Varrla, Claudia Backes, Ronan J. Smith, Umar Khan, Arlene O'Neill, Conor Boland, Mustafa Lotya, Oana M. Istrate, Paul King, Tom Higgins, Sebastian Barwich, Peter May, Pawel Puczkarski, Iftikhar Ahmed, Matthias Moebius, Henrik Pettersson, Edmund Long, João Coelho, Sean E. O'Brien, Eva K. McGuire, Beatriz Mendoza Sanchez, Georg S. Duesberg, Niall McEvoy, Timothy J. Pennycook, Clive Downing, Alison Crossley, Valeria Nicolosi, and Jonathan N. Coleman. Scalable production of large quantities of defect-free few-layer graphene by shear exfoliation in liquids. *Nature Materials*, 13(6):624–630, 2014. doi:10.1038/nmat3944.

[165] Alan P. Kauling, Andressa T. Seefeldt, Diego P. Pisoni, Roshini C. Pradeep, Ricardo Bentini, Ricardo V. B. Oliveira, Konstantin S. Novoselov, and Antonio H. Castro Neto. The worldwide graphene flake production. *Advanced Materials*, 30(44):1803784, 2018. doi:10.1002/adma.201803784.

[166] L. M. Malard, M. A. Pimenta, G. Dresselhaus, and M. S. Dresselhaus. Raman spectroscopy in graphene. *Physics Reports*, 473(5):51–87, 2009. doi:10.1016/j.physrep.2009.02.003.

[167] Sasha Stankovich, Dmitriy A. Dikin, Richard D. Piner, Kevin A. Kohlhaas, Alfred Kleinhammes, Yuanyuan Jia, Yue Wu, SonBinh T. Nguyen, and Rodney S. Ruoff. Synthesis of graphene-based nanosheets via chemical reduction of exfoliated graphite oxide. *Carbon*, 45(7):1558–1565, 2007. doi:10.1016/j.carbon.2007.02.034.

[168] Vincent C. Tung, Matthew J. Allen, Yang Yang, and Richard B. Kaner. High-throughput solution processing of large-scale graphene. *Nature Nanotechnology*, 4(1):25–29, 2009. doi:10.1038/nnano.2008.329.

[169] A. Eckmann, A. Felten, A. Mishchenko, L. Britnell, R. Krupke, K. S. Novoselov, and C. Casiraghi. Probing the nature of defects in graphene by Raman spectroscopy. *Nano Lett*, 12(8):3925–30, 2012. doi:10.1021/nl300901a.

[170] M. V. Bracamonte, G. I. Lacconi, S. E. Urreta, and L. E. F. Foa Torres. On the nature of defects in liquid-phase exfoliated graphene. *The Journal of Physical Chemistry C*, 118(28):15455–15459, 2014. doi:10.1021/jp501930a.

[171] Wei Zhao, Abhilash Sugunan, Zhi-Bin Zhang, and Anwar Ahniyaz. Graphene and flavin mononucleotide interaction in aqueous graphene dispersions. *The Journal of Physical Chemistry C*, 123(43):26282–26288, 2019. doi:10.1021/acs.jpcc.9b06442.

[172] Katsuhiko Ariga, Ayumi Kamino, Hiroshi Koyano, and Toyoki Kunitake. Recognition of aqueous flavin mononucleotide on the surface of binary monolayers of guanidinium and melamine amphiphiles. *Journal of Materials Chemistry*, 7 (7):1155–1161, 1997. doi:10.1039/A700081B.

[173] Igor Popov, Gotthard Seifert, and David Tománek. Designing electrical contacts to mos 2 monolayers: A computational study. *Physical Review Letters*, 108(15):156802, 2012. doi:10.1103/PhysRevLett.108.156802.

[174] Z. Chen, J. Wang, D. Pan, Y. Wang, R. Noetzel, H. Li, P. Xie, W. Pei, A. Umar, L. Jiang, N. Li, N. F. Rooij, and G. Zhou. Mimicking a dog's nose: Scrolling graphene nanosheets. *ACS Nano*, 12(3):2521–2530, 2018. doi:10.1021/acsnano.7b08294.

[175] Kewei Shu, Caiyun Wang, Sha Li, Chen Zhao, Yang Yang, Huakun Liu, and Gordon Wallace. Flexible free-standing graphene paper with interconnected porous structure for energy storage. *Journal of Materials Chemistry A*, 3(8): 4428–4434, 2015. doi:10.1039/C4TA04324C.

[176] Shumao Cui, Shun Mao, Zhenhai Wen, Jingbo Chang, Yang Zhang, and Junhong Chen. Controllable synthesis of silver nanoparticle-decorated reduced graphene oxide hybrids for ammonia detection. *Analyst*, 138(10):2877–2882, 2013. doi:10.1039/C3AN36922F.

[177] Fazel Yavari, Zongping Chen, Abhay V. Thomas, Wencai Ren, Hui-Ming Cheng, and Nikhil Koratkar. High sensitivity gas detection using a macroscopic three-Dimensional graphene foam network. *Scientific Reports*, 1(1):166, 2011. doi:10.1038/srep00166.

[178] Fazel Yavari, Eduardo Castillo, Hemtej Gullapalli, Pulickel M. Ajayan, and Nikhil Koratkar. High sensitivity detection of NO2 and NH3 in air using chemical vapor deposition grown graphene. *Applied Physics Letters*, 100(20), 2012. doi:10.1063/1.4720074.

[179] Madhav Gautam and Ahalapitiya H. Jayatissa. Ammonia gas sensing behavior of graphene surface decorated with gold nanoparticles. *Solid-State Electronics*, 78:159–165, 2012. doi:10.1016/j.sse.2012.05.059.

[180] R. K. Paul, S. Badhulika, N. M. Saucedo, and A. Mulchandani. Graphene nanomesh as highly sensitive chemiresistor gas sensor. *Anal Chem*, 84(19): 8171–8, 2012. doi:10.1021/ac3012895.

[181] Byungjin Cho, Jongwon Yoon, Myung Gwan Hahm, Dong-Ho Kim, Ah Ra Kim, Yung Ho Kahng, Sang-Won Park, Young-Joo Lee, Sung-Gyu Park, Jung-Dae Kwon, Chang Su Kim, Myungkwan Song, Yongsoo Jeong, Kee-Seok Nam, and Heung Cho Ko. Graphene-based gas sensor: metal decoration effect and application to a flexible device. *J. Mater. Chem. C*, 2(27):5280–5285, 2014. doi:10.1039/c4tc00510d.

[182] F. Ricciardella, B. Alfano, F. Loffredo, F. Villani, T. Polichetti, M. L. Miglietta, E. Massera, and G. Di Francia. Inkjet printed graphene-based chemi-resistors for gas detection in environmental conditions. In *2015 XVIII AISEM Annual Conference*, pages 1–4. doi:10.1109/AISEM.2015.7066858.

[183] Hui Zhang, Liwei Fan, Huilong Dong, Pingping Zhang, Kaiqi Nie, Jun Zhong, Youyong Li, Jinghua Guo, and Xuhui Sun. Spectroscopic investigation of plasma-fluorinated monolayer graphene and application for gas sensing. *ACS Applied Materials & Interfaces*, 8(13):8652–8661, 2016. doi:10.1021/acsami.5b11872.

[184] Cheol-Soo Yang, Ather Mahmood, Bongseock Kim, Kyusoon Shin, Do Hyun Jeon, Jin Kyu Han, Sang Don Bu, Serin Park, Won Jin Choi, Bernard Doudin, and Jeong-O. Lee. Enhancing gas sensing properties of graphene by using a nanoporous substrate. *2D Materials*, 3(1):011007, 2016. doi:10.1088/2053-1583/3/1/011007.

[185] Min Zhao, Lanqin Yan, Xianfeng Zhang, Lihua Xu, Zhiwei Song, Peipei Chen, Fengliang Dong, and Weiguo Chu. Room temperature NH3 detection of ti/-graphene devices promoted by visible light illumination. *Journal of Materials Chemistry C*, 5(5):1113–1120, 2017. doi:10.1039/C6TC04416F.

[186] Xiaohui Tang, Driss Lahem, Jean-Pierre Raskin, Pierre Gerard, Xin Geng, Nicolas Andre, and Marc Debliquy. A fast and room-temperature operation ammonia sensor based on compound of graphene with polypyrrole. *IEEE Sensors Journal*, 18(22):9088–9096, 2018. doi:10.1109/jsen.2018.2869203.

[187] M. Kodu, A. Berholts, T. Kahro, J. Eriksson, R. Yakimova, T. Avarmaa, I. Renge, H. Alles, and R. Jaaniso. Graphene-based ammonia sensors functionalised with sub-monolayer V2O5: A comparative study of chemical vapour deposited and epitaxial graphene dagger. *Sensors (Basel)*, 19(4), 2019. doi:10.3390/s19040951.

[188] Xiaoqing Zhou, Xiaolin Wang, Bin Wang, Zhimin Chen, Chunying He, and Yiqun Wu. Preparation, characterization and NH3-sensing properties of reduced

graphene oxide/copper phthalocyanine hybrid material. *Sensors and Actuators B: Chemical*, 193:340–348, 2014. doi:10.1016/j.snb.2013.11.090.

[189] Fang Niu, Li-Ming Tao, Yu-Chao Deng, Qi-Hua Wang, and Wei-Guo Song. Phosphorus doped graphene nanosheets for room temperature NH3 sensing. *New Journal of Chemistry*, 38(6), 2014. doi:10.1039/c4nj00162a.

[190] Jianwei Wang, Servin Rathi, Budhi Singh, Inyeal Lee, Sunglyul Maeng, Han-Ik Joh, and Gil-Ho Kim. Dielectrophoretic assembly of pt nanoparticle-reduced graphene oxide nanohybrid for highly-sensitive multiple gas sensor. *Sensors and Actuators B: Chemical*, 220:755–761, 2015. doi:10.1016/j.snb.2015.05.133.

[191] Le Thai Duy, Duck-Jin Kim, Tran Quang Trung, Vinh Quang Dang, Bo-Yeong Kim, Hock Key Moon, and Nae-Eung Lee. High performance three-dimensional chemical sensor platform using reduced graphene oxide formed on high aspect-ratio micro-pillars. *Advanced Functional Materials*, 25(6):883–890, 2015. doi:10.1002/adfm.201401992.

[192] J. Wu, K. Tao, Y. Guo, Z. Li, X. Wang, Z. Luo, S. Feng, C. Du, D. Chen, J. Miao, and L. K. Norford. A 3D chemically modified graphene hydrogel for fast, highly sensitive, and selective gas sensor. *Adv Sci (Weinh)*, 4(3):1600319, 2017. doi:10.1002/advs.201600319.

[193] William Humphrey, Andrew Dalke, and Klaus Schulten. VMD: Visual molecular dynamics. *Journal of Molecular Graphics*, 14(1):33–38, 1996. doi:10.1016/0263-7855(96)00018-5.

[194] Lu Zhang, Zijian Zhang, Chaozheng He, Liming Dai, Jun Liu, and Lixiang Wang. Rationally designed surfactants for few-layered graphene exfoliation: Ionic groups attached to electron-deficient pi -conjugated unit through alkyl spacers. *ACS Nano*, 8(7):6663–6670, 2014. doi:10.1021/nn502289w.

[195] A. K. Manna and S. K. Pati. Tuning the electronic structure of graphene by molecular charge transfer: a computational study. *Chem Asian J*, 4(6):855–60, 2009. doi:10.1002/asia.200800486.

[196] Zengxing Zhang, Helin Huang, Xiaomei Yang, and Ling Zang. Tailoring electronic properties of graphene by pi-pi stacking with aromatic molecules. *The Journal of Physical Chemistry Letters*, 2(22):2897–2905, 2011. doi:10.1021/jz201273r.

[197] L. Kong, A. Enders, T. S. Rahman, and P. A. Dowben. Molecular adsorption on graphene. *J Phys Condens Matter*, 26(44):443001, 2014. doi:10.1088/0953-8984/26/44/443001.

[198] Farheen Khurshid, M. Jeyavelan, Keisuke Takahashi, M. Sterlin Leo Hudson, and S. Nagarajan. Aryl fluoride functionalized graphene oxides for excellent room temperature ammonia sensitivity/selectivity. *RSC Advances*, 8(36): 20440–20449, 2018. doi:10.1039/c8ra01818a.

[199] R. M. Minyaev and G. V. Orlova. Covalent nature of the hydrogen bond. *Journal of Structural Chemistry*, 26(2):157–164, 1985. doi:10.1007/BF00754217.

[200] Jin Zhou, Hongzhen Lin, Xue-Feng Cheng, Jie Shu, Jing-Hui He, Hua Li, Qing-Feng Xu, Na-Jun Li, Dong-Yun Chen, and Jian-Mei Lu. Ultrasensitive and robust organic gas sensors through dual hydrogen bonding. *Materials Horizons*, 6(3): 554–562, 2019. doi:10.1039/c8mh01098f.

[201] Sanne Boesveldt and Valentina Parma. The importance of the olfactory system in human well-being, through nutrition and social behavior. *Cell and Tissue Research*, 383(1):559–567, 2021. doi:10.1007/s00441-020-03367-7.

[202] Michael T. Shipley, Matthew Ennis, and Adam C. Puche. *The Olfactory System*, pages 579–593. Humana Press, Totowa, NJ, 2003. doi:10.1007/978-1-59259-371-2_27.

[203] Manuel Zarzo. The sense of smell: molecular basis of odorant recognition. *Biological Reviews*, 82(3):455–479, 2007. doi:10.1111/j.1469-185X.2007.00019.x.

[204] K. C. Hoover. Smell with inspiration: the evolutionary significance of olfaction. *Am J Phys Anthropol*, 143 Suppl 51:63–74, 2010. doi:10.1002/ajpa.21441.

[205] Wenwen Hu, Liangtian Wan, Yingying Jian, Cong Ren, Ke Jin, Xinghua Su, Xiaoxia Bai, Hossam Haick, Mingshui Yao, and Weiwei Wu. Electronic noses: From advanced materials to sensors aided with data processing. *Advanced Materials Technologies*, 2018. doi:10.1002/admt.201800488.

[206] T. Wasilewski, J. Gebicki, and W. Kamysz. Bioelectronic nose: Current status and perspectives. *Biosens Bioelectron*, 87:480–494, 2017. doi:10.1016/j.bios.2016.08.080.

[207] Julian W. Gardner and Philip N. Bartlett. A brief history of electronic noses. *Sensors and Actuators B: Chemical*, 18(1-3):210–211, 1994. doi:10.1016/0925-4005(94)87085-3.

[208] F. S. Fedorov, A. Yaqin, D. V. Krasnikov, V. A. Kondrashov, G. Ovchinnikov, Y. Kostyukevich, S. Osipenko, and A. G. Nasibulin. Detecting cooking state of grilled chicken by electronic nose and computer vision techniques. *Food Chem*, 345:128747, 2021. doi:10.1016/j.foodchem.2020.128747.

[209] A. Lichtenstein, E. Havivi, R. Shacham, E. Hahamy, R. Leibovich, A. Pevzner, V. Krivitsky, G. Davivi, I. Presman, R. Elnathan, Y. Engel, E. Flaxer, and F. Patolsky. Supersensitive fingerprinting of explosives by chemically modified nanosensors arrays. *Nat Commun*, 5:4195, 2014. doi:10.1038/ncomms5195.

[210] Hayley Rottiers, Daylan Amelia Tzompa Sosa, Liesbet Van de Vyver, Michael Hinneh, Helena Everaert, Jocelyn De Wever, Kathy Messens, and Koen Dewettinck. Discrimination of cocoa liquors based on their odor fingerprint: a fast GC electronic nose suitability study. *Food Analytical Methods*, 12(2):475–488, 2018. doi:10.1007/s12161-018-1379-7.

[211] Junyu Zhang, Yingying Xue, Tao Zhang, Yuantao Chen, Xinwei Wei, Hao Wan, and Ping Wang. Detection of hazardous gas mixtures in the smart kitchen using an electronic nose with support vector machine. *Journal of The Electrochemical Society*, 167(14), 2020. doi:10.1149/1945-7111/abc83c.

[212] A. De Vincentis, G. Pennazza, M. Santonico, U. Vespasiani-Gentilucci, G. Galati, P. Gallo, C. Vernile, C. Pedone, R. Antonelli Incalzi, and A. Picardi. Breath-print analysis by e-nose for classifying and monitoring chronic liver disease: a proof-of-concept study. *Sci Rep*, 6:25337, 2016. doi:10.1038/srep25337.

[213] A. M. Graboski, C. A. Zakrzevski, F. M. Shimizu, R. T. Paschoalin, A. C. Soares, J. Steffens, N. Paroul, and C. Steffens. Electronic nose based on carbon nanocomposite sensors for clove essential oil detection. *ACS Sens*, 5(6):1814–1821, 2020. doi:10.1021/acssensors.0c00636.

[214] Tarik Saidi, Mohammed Moufid, Kelvin de Jesus Beleño-Saenz, Tesfalem Geremariam Welearegay, Nezha El Bari, Aylen Lisset Jaimes-Mogollon, Radu Ionescu, Jamal Eddine Bourkadi, Jouda Benamor, Mustapha El Ftouh, and Benachir Bouchikhi. Non-invasive prediction of lung cancer histological types through exhaled breath analysis by UV-irradiated electronic nose and GC/QTOF/MS. *Sensors and Actuators B: Chemical*, 311, 2020. doi:10.1016/j.snb.2020.127932.

[215] H. Y. Yang, Y. C. Wang, H. Y. Peng, and C. H. Huang. Breath biopsy of breast cancer using sensor array signals and machine learning analysis. *Sci Rep*, 11(1):103, 2021. doi:10.1038/s41598-020-80570-0.

[216] Ernest Bonah, Xingyi Huang, Ren Yi, Joshua H. Aheto, Richard Osae, and Moses Golly. Electronic nose classification and differentiation of bacterial foodborne pathogens based on support vector machine optimized with particle swarm optimization algorithm. *Journal of Food Process Engineering*, 42(6), 2019. doi:10.1111/jfpe.13236.

[217] M. M. Macias, A. G. Manso, C. J. Orellana, H. M. Velasco, R. G. Caballero, and J. C. Chamizo. Acetic acid detection threshold in synthetic wine samples of a portable electronic nose. *Sensors (Basel)*, 13(1):208–20, 2012. doi:10.3390/s130100208.

[218] Rahul Kumar, Xianghong Liu, Jun Zhang, and Mahesh Kumar. Room-temperature gas sensors under photoactivation: From metal oxides to 2D materials. *Nano-Micro Letters*, 12(1), 2020. doi:10.1007/s40820-020-00503-4.

[219] R. Gutierrez-Osuna. *Signal conditioning and pre-processing*. Wiley-VCH, Weinheim, 2002. doi:10.1002/3527601597.ch5.

[220] E. C. Nallon, V. P. Schnee, C. J. Bright, M. P. Polcha, and Q. Li. Discrimination enhancement with transient feature analysis of a graphene chemical sensor. *Anal Chem*, 88(2):1401–6, 2016. doi:10.1021/acs.analchem.5b04050.

[221] T. Hummel, K. Rissom, J. Reden, A. Hahner, M. Weidenbecher, and K. B. Huttenbrink. Effects of olfactory training in patients with olfactory loss. *Laryngoscope*, 119(3):496–9, 2009. doi:10.1002/lary.20101.

[222] Haisong Qi, Jianwen Liu, Jürgen Pionteck, Petra Pötschke, and Edith Mäder. Carbon nanotube–cellulose composite aerogels for vapour sensing. *Sensors and Actuators B: Chemical*, 213:20–26, 2015. doi:10.1016/j.snb.2015.02.067.

[223] J. Lotsch, D. Kringel, and T. Hummel. Machine learning in human olfactory research. *Chem Senses*, 44(1):11–22, 2019. doi:10.1093/chemse/bjy067.

[224] David Van Der Spoel, Erik Lindahl, Berk Hess, Gerrit Groenhof, Alan E. Mark, and Herman J. C. Berendsen. GROMACS fast, flexible, and free. *Journal of Computational Chemistry*, 26(16):1701–1718, 2005. doi:10.1002/jcc.20291.

[225] Alpeshkumar K. Malde, Le Zuo, Matthew Breeze, Martin Stroet, David Poger, Pramod C. Nair, Chris Oostenbrink, and Alan E. Mark. An automated force field topology builder (ATB) and repository: Version 1.0. *Journal of Chemical Theory and Computation*, 7(12):4026–4037, 2011. doi:10.1021/ct200196m.

[226] M. Elstner. SCC-DFTB: What is the proper degree of self-consistency? *The Journal of Physical Chemistry A*, 111(26):5614–5621, 2007. doi:10.1021/jp071338j.

[227] Michael Gaus, Qiang Cui, and Marcus Elstner. DFTB3: Extension of the self-consistent-charge density-functional tight-binding method (scc-dftb). *Journal of Chemical Theory and Computation*, 7(4):931–948, 2011. doi:10.1021/ct100684s.

[228] R. S. Mulliken. Electronic population analysis on LCAO–MO molecular wave functions. i. *The Journal of Chemical Physics*, 23(10):1833–1840, 1955. doi:10.1063/1.1740588.

[229] Lihua Li, Xiaoli Zheng, Jianjun Wang, Qiang Sun, and Qun Xu. Solvent-exfoliated and functionalized graphene with assistance of supercritical carbon dioxide. *ACS Sustainable Chemistry & Engineering*, 1(1):144–151, 2012. doi:10.1021/sc3000724.

[230] D. Parviz, S. Das, H. S. Ahmed, F. Irin, S. Bhattacharia, and M. J. Green. Dispersions of non-covalently functionalized graphene with minimal stabilizer. *ACS Nano*, 6(10):8857–67, 2012. doi:10.1021/nn302784m.

[231] J. Krenkova, M. Liskova, R. Cmelik, G. Vigh, and F. Foret. Multi-cationic aminopyrene-based labeling tags for oligosaccharide analysis by capillary electrophoresis-mass spectrometry. *Anal Chim Acta*, 1095:226–232, 2020. doi:10.1016/j.aca.2019.10.032.

[232] Qiang Yang, Xuejun Pan, Fang Huang, and Kecheng Li. Fabrication of high-concentration and stable aqueous suspensions of graphene nanosheets by noncovalent functionalization with lignin and cellulose derivatives. *The Journal of Physical Chemistry C*, 114(9):3811–3816, 2010. doi:10.1021/jp910232x.

[233] D. Zaharie-Butucel, M. Potara, A. M. Craciun, R. Boukherroub, S. Szunerits, and S. Astilean. Revealing the structure and functionality of graphene oxide and reduced graphene oxide/pyrene carboxylic acid interfaces by correlative spectral and imaging analysis. *Physical Chemistry Chemical Physics*, 19(24):16038–16046, 2017. doi:10.1039/C7CP02443F.

[234] Deana Kwong Hong Tsang, Tyler J. Lieberthal, Clare Watts, Iain E. Dunlop, Sami Ramadan, Armando E. del Rio Hernandez, and Norbert Klein. Chemically functionalised graphene FET biosensor for the label-free sensing of exosomes. *Scientific Reports*, 9(1), 2019. doi:10.1038/s41598-019-50412-9.

[235] Ellie Yi Lih Teo, Gomaa A. M. Ali, H. Algarni, Wilairat Cheewasedtham, Thitima Rujiralai, and Kwok Feng Chong. One-step production of pyrene-1-boronic acid functionalized graphene for dopamine detection. *Materials Chemistry and Physics*, 231:286–291, 2019. doi:10.1016/j.matchemphys.2019.04.029.

[236] J. Irani, N. Pise, and M. Phatak. Clustering techniques and the similarity measures used in clustering: A survey. *International Journal of Computer Applications*, 134:9–14, 2016. doi:10.5120/ijca2016907841.

[237] M. E. Frank, D. B. Fletcher, and T. P. Hettinger. Recognition of the component odors in mixtures. *Chem Senses*, 42(7):537–546, 2017. doi:10.1093/chemse/bjx031.

[238] Charlotte Sinding, Gérard Coureaud, Claire Chabanet, Adeline Chambault, Noelle Béno, Thibaut Dosne, Benoist Schaal, and Thierry Thomas-Danguin. *Perceptual Interactions in Complex Odor Mixtures*, pages 27–31. 2014. doi:10.1016/b978-0-12-398549-1.00005-2.

[239] T. Thomas-Danguin, C. Sinding, S. Romagny, F. El Mountassir, B. Atanasova, E. Le Berre, A. M. Le Bon, and G. Coureaud. The perception of odor objects in everyday life: a review on the processing of odor mixtures. *Front Psychol*, 5: 504, 2014. doi:10.3389/fpsyg.2014.00504.

[240] Leslie M. Kay, Tanja Crk, and Jennifer Thorngate. A redefinition of odor mixture quality. *Behavioral Neuroscience*, 119(3):726–733, 2005. doi:10.1037/0735-7044.119.3.726.

[241] A. L. Bierling, I. Croy, T. Hummel, G. Cuniberti, and A. Croy. Olfactory perception in relation to the physicochemical odor space. *Brain Sci*, 11(5), 2021. doi:10.3390/brainsci11050563.

[242] A. Keller, R. C. Gerkin, Y. Guan, A. Dhurandhar, G. Turu, B. Szalai, J. D. Mainland, Y. Ihara, C. W. Yu, R. Wolfinger, C. Vens, L. Schietgat, K. De Grave, R. Norel, Dream Olfaction Prediction Consortium, G. Stolovitzky, G. A. Cecchi, L. B. Vosshall, and P. Meyer. Predicting human olfactory perception from chemical features of odor molecules. *Science*, 355(6327):820–826, 2017. doi:10.1126/science.aal2014.

[243] Andrew Dravnieks, Thomas Masurat, and Richard A. Lamm. Hedonics of odors and odor descriptors. *Journal of the Air Pollution Control Association*, 34 (7):752–755, 1984. doi:10.1080/00022470.1984.10465810.

[244] R. Haddad, A. Medhanie, Y. Roth, D. Harel, and N. Sobel. Predicting odor pleasantness with an electronic nose. *PLoS Comput Biol*, 6(4):e1000740, 2010. doi:10.1371/journal.pcbi.1000740.

[245] R. M. Khan, C. H. Luk, A. Flinker, A. Aggarwal, H. Lapid, R. Haddad, and N. Sobel. Predicting odor pleasantness from odorant structure: pleasantness as a reflection of the physical world. *J Neurosci*, 27(37):10015–23, 2007. doi:10.1523/JNEUROSCI.1158-07.2007.

[246] Yehya El-Sayed and Teresa J. Bandosz. Role of surface oxygen groups in incorporation of nitrogen to activated carbons via ethylmethylamine adsorption. *Langmuir*, 21(4):1282–1289, 2005. doi:10.1021/la0483966.

[247] Marcus Franz, Hassan A. Arafat, and Neville G. Pinto. Effect of chemical surface heterogeneity on the adsorption mechanism of dissolved aromatics on activated carbon. *Carbon*, 38(13):1807–1819, 2000. doi:10.1016/S0008-6223(00)00012-9.

[248] Quanzi Yuan, Ya-Pu Zhao, Limiao Li, and Taihong Wang. Ab initio study of ZnO-based gas-sensing mechanisms: Surface reconstruction and charge transfer. *The Journal of Physical Chemistry C*, 113(15):6107–6113, 2009. doi:10.1021/jp810161j.

[249] Serdar Ozdemir and James L. Gole. A phosphine detection matrix using nanostructure modified porous silicon gas sensors. *Sensors and Actuators B: Chemical*, 151(1):274–280, 2010. doi:10.1016/j.snb.2010.08.016.

[250] H. Wu, Z. Ma, Z. Lin, H. Song, S. Yan, and Y. Shi. High-sensitive ammonia sensors based on tin monoxide nanoshells. *Nanomaterials (Basel)*, 9(3), 2019. doi:10.3390/nano9030388.

[251] K. Wilma, T. Unger, S. Tuncel Kostakoglu, M. Hollfelder, C. Hunger, A. Lang, A. G. Gurek, M. Thelakkat, J. Kohler, A. Kohler, S. Gekle, and R. Hildner. Excited state dynamics and conformations of a Cu(ii)-phthalocyanine-perylenebisimide dyad. *Phys Chem Chem Phys*, 19(33):22169–22176, 2017. doi:10.1039/c7cp04026a.

[252] Barun Das, Rakesh Voggu, Chandra Sekhar Rout, and C. N. R. Rao. Changes in the electronic structure and properties of graphene induced by molecular charge-transfer. *Chemical Communications*, (41):5155–5157, 2008. doi:10.1039/B808955H.

[253] Xiaochen Dong, Dongliang Fu, Wenjing Fang, Yumeng Shi, Peng Chen, and Lain-Jong Li. Doping single-layer graphene with aromatic molecules. *Small*, 5 (12):1422–1426, 2009. doi:10.1002/smll.200801711.

[254] R. Prabakaran, R. Kesavamoorthy, G.L.N. Reddy, and F.P. Xavier. Structural investigation of copper phthalocyanine thin films using X-ray Diffraction, Raman Scattering and Optical Absorption Measurements. *physica status solidi (b)*, 229(3):1175–1186, 2002. doi:10.1002/1521-3951(200202)229:3<1175::AID-PSSB1175>3.0.CO;2-K.

[255] Anindarupa Chunder, Tanusri Pal, Saiful I. Khondaker, and Lei Zhai. Reduced graphene oxide/copper phthalocyanine composite and its optoelectrical properties. *The Journal of Physical Chemistry C*, 114(35):15129–15135, 2010. doi:10.1021/jp104587n.

[256] Ross A. Hatton, Nicholas P. Blanchard, Vlad Stolojan, Anthony J. Miller, and S. Ravi P. Silva. Nanostructured copper phthalocyanine-sensitized multiwall carbon nanotube films. *Langmuir*, 23(11):6424–6430, 2007. doi:10.1021/la070156d.

[257] L. Guardia, M. J. Fernández-Merino, J. I. Paredes, P. Solís-Fernández, S. Villar-Rodil, A. Martínez-Alonso, and J. M. D. Tascón. High-throughput production of pristine graphene in an aqueous dispersion assisted by non-ionic surfactants. *Carbon*, 49(5):1653–1662, 2011. doi:10.1016/j.carbon.2010.12.049.

[258] Jianwei Wang, Servin Rathi, Budhi Singh, Inyeal Lee, Han-Ik Joh, and Gil-Ho Kim. Alternating current dielectrophoresis optimization of pt-decorated graphene oxide nanostructures for proficient hydrogen gas sensor. *ACS Applied Materials & Interfaces*, 7(25):13768–13775, 2015. doi:10.1021/acsami.5b01329.

[259] Hervé Abdi and Lynne J. Williams. Principal component analysis. *WIREs Computational Statistics*, 2(4):433–459.

[260] Alok Sharma and Kuldip K. Paliwal. Linear discriminant analysis for the small sample size problem: an overview. *International Journal of Machine Learning and Cybernetics*, 6(3):443–454, 2015. doi:10.1007/s13042-013-0226-9.

[261] A. Ravia, K. Snitz, D. Honigstein, M. Finkel, R. Zirler, O. Perl, L. Secundo, C. Laudamiel, D. Harel, and N. Sobel. A measure of smell enables the creation of olfactory metamers. *Nature*, 588(7836):118–123, 2020. doi:10.1038/s41586-020-2891-7.

[262] Haihan Chen, Mychel E. Varner, R. Benny Gerber, and Barbara J. Finlayson-Pitts. Reactions of methanesulfonic acid with amines and ammonia as a source of new particles in air. *The Journal of Physical Chemistry B*, 120(8):1526–1536, 2016. doi:10.1021/acs.jpcb.5b07433.

[263] Congfei Yao, Yucui Hou, Shuhang Ren, Weize Wu, Youan Ji, and Hui Liu. Sulfonate based zwitterions: A new class of extractants for separating phenols from oils with high efficiency via forming deep eutectic solvents. *Fuel Processing Technology*, 178:206–212, 2018. doi:10.1016/j.fuproc.2018.05.031.

[264] P. G. Sennikov. Weak hydrogen-bonding by second-row (PH3, H2S) and third-row (AsH3, H2Se) hydrides. *The Journal of Physical Chemistry*, 98(19):4973–4981, 1994. doi:10.1021/j100070a006.

[265] Hoa Nguyen and Sherif A. El-Safty. Meso- and macroporous Co3O4 nanorods for effective VOC gas sensors. *The Journal of Physical Chemistry C*, 115(17):8466–8474, 2011. doi:10.1021/jp1116189.

[266] Yuanyuan Yu, Enxiu Wu, Yan Chen, Zhihong Feng, Shijun Zheng, Hao Zhang, Wei Pang, Jing Liu, and Daihua Zhang. Volatile organic compounds discrimination based on dual mode detection. *Nanotechnology*, 29(24):245502, 2018. doi:10.1088/1361-6528/aab29b.

[267] S. Kim, J. Chen, T. Cheng, A. Gindulyte, J. He, S. He, Q. Li, B. A. Shoemaker, P. A. Thiessen, B. Yu, L. Zaslavsky, J. Zhang, and E. E. Bolton. PubChem in 2021: new data content and improved web interfaces. *Nucleic Acids Res*, 49(D1):D1388–d1395, 2021. doi:10.1093/nar/gkaa971.

List of publications

Publications in peer-reviewed journals

1. **Shirong Huang**, Luis Antonio Panes-Ruiz, Alexander Croy, Markus Löffler, Vyacheslav Khavrus, Viktor Bezugly, and Gianaurelio Cuniberti. "Highly sensitive room temperature ammonia gas sensor using pristine graphene: The role of biocompatible stabilizer." *Carbon* 173 (2021): 262-270.

2. **Shirong Huang**, Alexander Croy, Viktor Bezugly, and Gianaurelio Cuniberti. "Stabilization of aqueous graphene dispersions utilizing a biocompatible dispersant: a molecular dynamics study." *Physical Chemistry Chemical Physics* 21, no. 43 (2019): 24007-24016.

3. **Shirong Huang**, Alexander Croy, Luis Antonio Panes-Ruiz, Vyacheslav Khavrus, Viktor Bezugly, Bergoi Ibarlucea, Gianaurelio Cuniberti. Identification of Ammonia and Phosphine Gas Using Graphene Nanosensor with Machine Learning Techniques. *Advanced Intelligent Systems* (DOI:10.1002/aisy.202200016)

4. **Shirong Huang**, Alexander Croy, Antonie Louise Bierling, Vyacheslav Khavrus, Luis Antonio Panes-Ruiz, Arezoo Dianat, Bergoi Ibarlucea, Gianaurelio Cuniberti. Machine learning-enabled biomimetic electronic olfaction using graphene single-channel sensors. (In preparation)

5. Jinbo Pang, **Shirong Huang**, Bergoi Ibarlucea, Gianaurelio Cuniberti, et.al. Applications of MXene for information device applications. (In preparation)

Conference contributions/proceedings

1. **Shirong Huang**, Alexander Croy, Bergoi Ibarlucea, Gianaurelio Cuniberti. NH_3 and PH_3 Identification Using Graphene based Gas Sensor. 2021 Trends in Nan-

otechnology International Conference (TNT2021), Oct. 04-08, 2021, Tirana, Albania.

2. **Shirong Huang**. Short Course Summer 2021 of International Society for Olfaction and Chemical Sensing (ISOCS). In search for COVID19: Olfaction, Biomarkers and a Pandemic agent. 26-28 May 2021. Online.

3. **Shirong Huang**, Luis Antonio Panes-Ruiz, Alexander Croy, Leif Riemenschneider, Vyacheslav Khavrus, Viktor Bezugly, and Gianaurelio Cuniberti. "Supramolecular Functionalized Pristine Graphene Utilizing a Bio-Compatible Stabilizer towards Ultra-Sensitive Ammonia Detection." Engineering Proceedings 6, no. 1 (2021): 14.

4. **Shirong Huang**, Luis Antonio Panes-Ruiz, Alexander Croy, Leif Riemenschneider, Vyacheslav Khavrus, Viktor Bezugly, and Gianaurelio Cuniberti. Supramolecular Functionalized Pristine Graphene Utilizing a Bio-Compatible Stabilizer towards Ultra-Sensitive Ammonia Detection. 8th International Symposium on Sensor Science (2021 I3S). 17–28 May 2021. Online.

5. **Shirong Huang**, Alexander Croy, Viktor Bezugly, Gianaurelio Cuniberti. Biocompatible graphene exfoliation assisted by flavin mononucleotide sodium: a molecular dynamics study. 2019 Chem2dmat conference, 3rd, Sep.- 6th, Sep, Dresden, Germany

6. **Shirong Huang**, Alexander Croy, Viktor Bezugly, Gianaurelio Cuniberti. Biocompatible graphene exfoliation assisted by flavin mononucleotide sodium: a molecular dynamics study. 2019 DPG Spring conference, 31th, March - 4th, April, Regensburg, Germany.

7. **Shirong Huang**, Alexander Croy, Viktor Bezugly, Gianaurelio Cuniberti. Aggregation of Flavin Mononucleotide Surfactants on Graphene: A Molecular Dynamics Study. Graphene 2018, June (26-29) Dresden, Germany.

Acknowledgements

First, I would like to thank my supervisor Prof. Dr. Gianaurelio Cuniberti for giving me the opportunity to conduct my PhD thesis at his chair. He provided me with invaluable trust and discussions during the course of my PhD and offered a highly energetic environment. This work would never be completed without his kind, warm and ongoing support and supervision!

I thank Dr. Viktor Bezugly for his kind support as a scientific supervisor at the beginning of my PhD period. I would like to thank Dr. Alexander Croy for his great effort as a co-scientific supervisor throughout my whole PhD. I highly appreciate that he supervised me during the last 4 years and help me grow personally with my tasks and challenges! I appreciate Dr. Bergoi Ibarlucea for his great work as a scientific supervisor in the last two years of my PhD. He always had an open ear for me when I was encountering with any problems and helped me to find solutions!

I would like thank my colleague Antonie Louise Bierling for her great support on the Olfactorial Perceptronic project cooperation. As well, I want to express my great thank to my colleagues Antonio Panes for various support and Dr. Vyacheslav Khavrus for his characterization assistance and Leif for his assistance on my project work. A special thanks to Dr. Markus Löffler for his kind assistance in SEM guidance, as well as Dr. Arezoo Dianat for her DFT contribution on the Olfactorial Perceptronic project. Without the nice working atmosphere in the chair, I would have never been able to finish my PhD. Many thanks to Bob, Jiao Wang, Xu Wang, Xinne Zhao, Tao Huang, Leif and all the other chair members in MBZ and HAL. For assistance with various organizational issues, great specials thanks are given to Sylvi and Grit. A special thank to SmartNanotubes team for technical assistance.

Finally, I would like to thank my parents and sister, in particular my wife and son, for their never-ending support and encouragement! Thanks!!